ABSTRACT

Title of Thesis: IMAGING PYROMETRY OF WOOD EMBERS UNDER SIMULATED MOVEMENT

James Baldwin
Master of Science, 2022

Thesis Directed by: Dr. Peter Sunderland
Department of Fire Protection Engineering

A major mechanism for wildland fire spread are spot fires, where small combusted organic particulate (firebrands) are lofted and transported to a remote location where they can then ignite new fires. The modeling of these spot fire ignitions is limited by the unknown surface temperature and emissivity of firebrands, which is challenging to measure due to the small size of firebrands (precluding the use of intrusive temperature methods such as thermocouples) as well as the dependency of conventional non-intrusive temperature measurements (e.g. Infrared Imagers) on emissivity. A solution to this is presented in Color Pyrometry, which uses color pixel intensities to determine an object's temperature based on a calibration against an object of known temperature/emissivity. The presented method is a Ratio Pyrometry approach between green and red pixel intensities normalized to camera settings, which demonstrates the benefit of being independent of object emissivity as validated by Planck's Law, and is based on a Blackbody Furnace calibration. To determine the method's applicability to realistic firebrand imaging conditions, which would provide the

most comprehensive understanding of firebrand ignition, the individual impact of firebrand movement speed on the pyrometry's surface temperature predictions is considered. An apparatus is developed that decouples firebrand movement speed from the surface wind speed (which is known to impact firebrand surface temperature) as well as allows for modulation of the firebrand's simulated movement speed, and involves rotating the imaging device about a fixed axis relative to a stationary firebrand. Five trials at a set orientation were conducted to verify the apparatus' repeatability, and subsequent trials of varying rotation speed, distance, applied wind speed, and mounting orientation were conducted. Both qualitatively and through a statistical analysis consisting of ANOVA and non-parametric distribution testing, firebrand movement speed and orientation are shown to have no individual impact on surface temperature. Average ember surface temperatures were found to be 922.1 ± 20.4 °C with a 1 m/s applied wind speed and 955.0 ± 20.2 °C with a 2 m/s applied wind speed, which is in agreement with previous studies. It is proven that the presented Pyrometry method's results are independent of a major complicating factor associated with realistic firebrands, which thereby further supports future efforts into wildland fire spread modeling.

IMAGING PYROMETRY OF WOOD EMBERS UNDER SIMULATED MOVEMENT

by

James Baldwin

Thesis submitted to the Faculty of the Graduate School of the
University of Maryland, College Park in partial fulfillment
of the requirements for the degree of
Master of Science
2022

Advisory Committee:
Professor Peter Sunderland, Chair/Advisor
Dr. Fernando Raffan-Montoya
Professor Stanislav Stoliarov

Acknowledgements

I owe many people thanks for their role in the completion of this thesis project. To my advisor Dr. Sunderland, thank you for providing guidance on my work and constantly offering kind words of encouragement. To the other graduate student on my project Mahdi Tlemsani, thank you for always letting me bounce ideas off of you (and for telling me when those ideas are awful). To my advisory committee, Dr. Stoliarov and Dr. Raffan-Montoya, thank you for taking the time to provide feedback and help guide me in this endeavor. To all of my friends and family, thank you for the support (and understanding of my schedule) over the last year. To all of the professors, staff, and students in the FPE department, and particularly the other graduate students in my cohort, thank you for all of the support, lessons, and memories - you've all made my last 5 years at UMD truly invaluable.

Table of Contents

List of Figures

List of Tables

List of Abbreviations

AHD	Adaptive Homogeneity-Directed
ANOVA	Analysis of Variance
CMOS	Complementary Metal Oxide Semiconductor
DC	Direct Current
DSLR	Digital Single-Lens Reflex
IR	Infrared
ISO	International Organization for Standardization
KS	Kolmogorov-Smirnov
LCD	Liquid Crystal Display
LED	Light Emitting Diode
MWU	Mann-Whitney U-Test
PDF	Probability Density Function
PPG	Patterned Pixel Grouping
PWM	Pulse-Width Modulation
RGB	Red-Green-Blue
RMSE	Root Mean Square Error
RPM	Rotations per Minute
SiC	Silicon Carbide
SNR	Signal-to-Noise Ratio
VNG	Variable Number of Gradients
WUI	Wildland-Urban Interface

1 Introduction

1.1 Motivation

Wildland fires are a global issue with an ever-growing impact to both natural and built environments. One of the predominant areas affected by these wildland fire events is California, where 4.2 million acres of wildland environment was burnt, 31 lives were lost, and approximately 112 million metric tons of Carbon Dioxide was release into the atmosphere in 2020 alone [19]. These figures individuallu lend credence to the devastation associated with these events, let alone the risk they pose to the US as a whole [6]. Reference [1], the U.S. Fire Administration, summarizes this risk to the United States: 46 million residences in more than 70,000 communities are threatened by wildland fires, between 2002 and 2016 an average exceeding 3000 homes a year were lost to fires in the Wildland-Urban Interface (WUI), and the WUI area that could potentially be exposed to wildland fire events continues to trend upward at a rate of 2 million acres per year. Taking these national figures with similar trends seen globally, the problem of wildland fires, and particularly those in the WUI, are evident. Further exacerbating this risk is the growing impact of climate change, which has been predicted to contribute to an increased occurrence and severity of these WUI fires [23, 5].

A major mechanism through which these wildland fire events propagate is through spot fires - where smoldering particulate released from the primary fire front, commonly referred to as firebrands, are lofted airborne by wind or buoyant flows and distributed up to several miles away from the initial flame front, where they have a tendency to collected in piles [6, 34, 36]. The occurrence of these spot fires poses a clear risk, not only in terms of directly spreading the fire and rendering a higher degree of damage but also in terms of taxing emergency response resources. Therefore, as society continues to combat wildland fire events, a comprehensive understanding of these spot fires is vital to minimize the direct and indirect costs of WUI fires to the environment, property, human lives, and public resources.

1.2 Literature Review

Research into wildland fire phenomena primarily focus on the WUI area, where human structures and wildland fire can readily meet, as opposed to alternative regions such as urban conflagrations or purely natural areas. The reason for this focus is twofold - the behavior of wildland fires in this WUI region are readily observable due to the existing infrastructure, thereby providing increased insight to the general mechanisms of wildland fire dynamics and propagation, and that they pose the most significant risk to human lives and property. As previously mentioned, firebrands are an area of key interest in this consideration of WUI fires due to their propensity to significantly contribute to the propagation, and therefore risk, of these events.

The study of firebrands includes three major disciplines in the context of fire research: Generation, Transport, and Ignition. Generation relates to the creation and release of firebrands from materials involved in a wildland fire, Transport relates to the lofting and movement behaviors of the firebrands through external forces such as buoyant flows and wind, and Ignition relates to the firebrand's deposition on fuel sources and the subsequent "Spot Fire" ignition occurring thereafter which serves as a major mechanism in wildland fire spread [6]. Previous literature reviews have detailed the mechanism behind these processes [34, 6]. A mechanism called the "Dragon" has been developed by NIST as an attempt to fully quantify the interaction between firebrands and the environment - at a basic level, this devices generates realistic representative firebrands and releases them in a shower such as could be seen in a wildland fire event, which allows for a consideration of the transport dynamics of these showers as well as the impact of a firebrand shower attack on various full-scale assemblies [31, 29, 30, 43, 42, 32, 41]. Summarily, these works have primarily focused on considering the comprehensive effect of firebrand attack on the ignition of full-scale man-made assemblies such as decks and roofs, as well as considered the impact of more individual factors on this ignition such as firebrand accumulation and the consequences of radiative heat transfer occurring in conjunction with the shower. Beyond this, in terms of general works, intrinsic

key features of firebrands such as smoldering time and various thermal parameters have been explored under laboratory conditions [11].

While firebrand generation and transport has been thoroughly quantified [44, 53, 2] even beyond the aforementioned comprehensive studies, firebrand ignition has received comparatively little individual consideration beyond direct observation of ignition behavior. The mechanism of spot fire ignition, and specifically the heat flux released by the ember pile under varying environmental conditions and pile sizes, has been investigated under laboratory conditions [16]. A previous study with a similar goal focused on the contribution and behavior of the fuel bed in this ignition process [33]. As previously discussed, and along a similar vein, there has also been investigation into the ignition capability of firebrands on plywood and orientation strand board (OSB) crevices as a function of their quantity and the fuel bed angle, which incorporated temperature analysis with an infrared camera [28]. The heat transfer relevant to spot fire ignitions has also been considered in simplified models, which serve as precursors to the application of the work presented in this report [50].

A major hurdle in modeling the ignition mechanism of firebrands lies in their small size - to develop a comprehensive heat transfer model the surface temperature of the firebrand needs to be quantified, and conventional intrusive temperature measurements such as thermocouples have a tendency to either quench the embers due to their small size, if the thermocouple is sufficiently large, or face issues in the ash generated by the smoldering ember, if the thermocouple is small [22]. Accordingly, a non-intrusive method is the most accurate, and simplest, means to estimate a firebrand's surface temperature. One of the most common non-intrusive temperature measurement tools, an infrared camera, has been used in previous studies with a high degree of success but faces several major drawbacks - infrared cameras are expensive (approximately $100,000 for the commonly used FLIR Model A8300sc), have a low resolution (approximately 0.92 megapixels for the same FLIR Model A8300sc), and have a dependence on the emissivity of the considered object which is poorly quantified for smoldering organics such as firebrands due to both the wide variations seen in

their fuel compositions as well as the temporal variation in this factor due to the complex environment typically surrounding firebrands [16, 49, 28]. Summarily, while an established non-intrusive temperature measurement approach, infrared imagers present challenges in developing an understanding of firebrand characteristics due to their high cost as well as their potential inaccuracies.

An answer to the problem of non-intrusive temperature measurements lies in the use of a standard DSLR camera for a process known as color pyrometry - where pixel intensity values produced by an image can be referenced to a calibration conducted on an object of known temperature and emissivity such as a blackbody furnace [25], or other similarly luminous objects with known emissivity such as a thermally-excited thermocouple [26] or tungsten lamp [47], to determine the imaged object's temperature. In this manner, accuracy is maintained in comparison to intrusive measurements and the drawbacks associated with Infrared camera readings are minimized. DSLR cameras cost a fraction of Infrared imagers which renders them more accessible, have a much higher resolution on average and therefore allow for a higher degree of measurement accuracy, and their results can be manipulated to remove the dependence on object surface emissivity by virtue of recording several different "channels" of light wavelengths [40]. Through this virtue, by taking the quotient of two of the light channels the emissivity dependence can be removed entirely from the pyrometry temperature calculation. The basis driving this analysis is Planck's Law, which can be used to relate the visual emittance from a gray body to its temperature [4]. This method has been validated within both theoretical and idealized frameworks [27], a reference which also considered the application of pyrometry to wood particles - although not in an ember/firebrand orientation, and more so as a representative charring material within an idealized furnace environment. Beyond this idealized consideration, pyrometry has also been validated in a multitude of realistic applications.

The literature shows a great degree of success in color pyrometry with DSLR cameras. The method has been used to characterize physical object's temperatures, such as burning

coal particles [47, 46] and glowing metal spark sprays (such as would be expected from the operation of an angle grinder applied to steel) [26], in addition to ember and firebrand temperatures such as is considered in this report. It has also been used to quantify fire-specific phenomena, such as upward flame spread and the associated driving radiative heat flux [3] and parameters of interest for char/soot production such as temperature and volume fraction in flames [15, 51, 38]. Additionally, the method has seen use in the general combustion field in applications such as engine design [21] and tube furnace operation validation [9]. There have also been studies quantifying the effect of complicating factors associated with combustion on pyrometry methods, such as in considering the radiation from combustion products [17]. Studies outside of the fire science field with temperature as a parameter of interest, such as with impact shock and hypersonic physics, have also seen success with pyrometry [37, 52].

Pyrometry studies on embers and firebrands have predominantly focused on establishing the general pyrometry analysis process for an object with spatial and temporal variations in surface temperature, as well as testing individual factors that could be relevant to field measurements of firebrands such as distance away from the target and ambient illuminance [8]. While previous studies have also considered the general impact of distance on pyrometry for idealized materials [9], additional consideration was desired in reference [8] to validate this for objects without spatially-resolved surface temperatures such as firebrands. Additionally, some preliminary analysis on how firebrand movement impacts pyrometry has been conducted - although the results were relatively inconclusive due to intricacies in the testing apparatus [22]. Therefore, being that firebrands are defined as moving objects, a more rigorous description of the impact of their movement on the pyrometry model is warranted in order to better quantify its applicability to realistic events and therefore support more accurate firebrand ignition models.

1.3 Gaps in Literature

Despite the effect of movement on color pyrometry being considered in a multitude of studies [26, 47, 22], several uncertainties and difficulties have still been noted in regard to its application to firebrands. In a color pyrometry study considering the temperatures of flying metal sparks [26], the practice of imaging moving objects for the purpose of pyrometry was considered but several key differences between spark and embers arise - namely, the sparks are assumed isothermal and with a constant emissivity which is not the case with embers [22, 8], and they note that the rotation of a lofted particle presents a source of uncertainty in the measurement. Additionally, in their discussion of the temperature progression of a single spark, they note that the particle velocity is unable to be determined from a single streak across an entire image. Despite this, the referenced study validated the application of pyrometry to moving objects by imaging a reproducibly heated metal ball with controlled movement, which lends credence to the practice. In a study considering the color pyrometry of moving coal particles [47], particles inside of a flame were considered which therefore demonstrated fundamentally different combustion characteristics to smoldering firebrands even beyond the differences in fuel source. Again, despite this key difference, this study provides a validation of applying pyrometry to moving objects. A study considering the movement of firebrands [22] in color pyrometry also presents several logistical shortcomings - specifically, a pendulum-esque apparatus was used which could only simulate a single velocity progression, the ember was secured with tweezers which presented the opportunity for quenching as noted previously in the same study for the application of thermocouples to embers, and the practice of physically moving the ember during imaging complicates the process of decoupling the effects of wind speed and velocity on the pyrometry process - the former of which has been found to positively correlate with the surface temperature of smoldering firebrands [48].

Beyond these gaps in literature for general pyrometry methods, there are also several firebrand-specific areas of continued interest. Beyond the aforementioned works on the same

project preceding this body of analysis [22, 8], an additional study has also focused specifically on the application of DSLR camera color pyrometry to firebrands [48]. While this study accurately quantified the impact of wind speed on firebrand surface temperature within a reasonable wind speed range, as well as further validated the use of a ratio pyrometry method through imaging the ember both with a DSLR color camera and an infrared camera, it also utilized idealized conditions - namely, the study was conducted in a darkened laboratory with a prescribed cohesive wind speed and a stationary ember. Because firebrands evidently exist outside of such controlled conditions, and the primary application of these works is modeling realistic wildland fire propagation, it is desirable to quantify the impact of complicating factors associated with WUI fires on the presented pyrometry methods.

1.4 Objectives

Following from these shortcomings in the literature, and the importance of understanding the spot fire ignition mechanism in combating the impact of wildland fire events through modeling, the primary objectives of this thesis are twofold - firstly, to create an apparatus that decouples object movement and accompanying factors such as relative wind speed to better analyze the individual contribution of particle velocity to pyrometry, and secondly, to analyze the surface temperature results from the consideration of firebrands with this apparatus. In this, the color pyrometry model established in previous studies under the same project [22, 8] is used. Firebrand movement is simulated by rotating a DSLR camera at varying speeds, distances, and orientations relative to a stationary ember in order to mimic the same exposure effect on the camera's CMOS light-sensing chip as conventional movement while simultaneously maintaining a strong degree of ember replicability. In this manner, the surface temperature of firebrands can be better quantified for use in endeavors such as wildland fire computer simulations and firebrand ignition heat transfer models, and the DSLR-based color pyrometry approach is further verified for use as a field diagnostic in objectives such as identifying spot fires and better observing wildland fire spread mechanisms.

2 Pyrometry Analysis Methodology

Images are recorded with a Sony DSC-RX10 III model Digital Single Lens Reflex (DSLR) camera, which produces a 14-bit .ARW raw file format. A representative image of this camera model is shown in Figure 2.1.

Figure 2.1: Sony DSC-RX10 III DSLR Camera

Camera settings were adjusted to maintain a strong degree of contrast between the ambient environment and ember while minimizing the number of saturated pixels on the ember's surface. Despite this design decision, the propagation of saturated pixel temperature uncertainties to average surface temperature results in this context is not significant for relatively few saturated pixels, as shown in the simple propagation considerations of I. The camera shutter speed was adjusted so as to capture the entire sweep of the ember as the camera rotated past it to capture a "worst-case" scenario of the impact of ember movement on

an image - the two other major camera settings considered, ISO and f-number, were adjusted accordingly to fit this goal. As approximate definitions for these factors, the shutter speed corresponds to exposure time, the ISO is a method of electrical brightening (increasing image gain), and the f-number correlates to the "zoom" or magnification of the image.

After recording, images were converted from the 14-bit .ARW raw format to a 16-bit .TIFF file for viewing and analysis with the open-source software dcraw, written by Dave Coffin [7]. This conversion process is necessary to make the image compatible with the pyrometry analysis procedures presented, as the raw format files do not present Red, Green, and Blue intensities at each pixel. The .ARW file contains information based on a Bayer Filter, shown below in Figure 2.2, which is tailored to approximate human vision. Its orientation results in each cell on the camera's Complementary Metal Oxide Semiconductor (CMOS) photovoltaic chip recording only a single wavelength of light intensity (Red, Green, or Blue), which results in the need for a method of interpolation in converting from the .ARW to .TIFF file such that each pixel will have its own Red, Green, and Blue value. This interpolation from a Bayer Filter's output intensities to a viewable RGB photograph is referred to as demosaicing. The image conversion software dcraw allows for the selection of interpolation method in this demosaicing process [7]. The different options show little impact on the pyrometry process, as is proven in Table 2.1 detailing the resulting average surface temperatures of a stationary ember demosaiced with different methods, so a simple bilinear interpolation method was used for its computational efficiency relative to the other options. This selection is in accordance with the process used in references [22, 8]. The camera's White Balance was taken as the default setting in dcraw [7], which is based on a color chart illuminated with a standard D65 lamp and is again consistent with references [22, 8]. The specific code used to process the photographs with dcraw was created in MATLAB, and is shown in Appendix B.

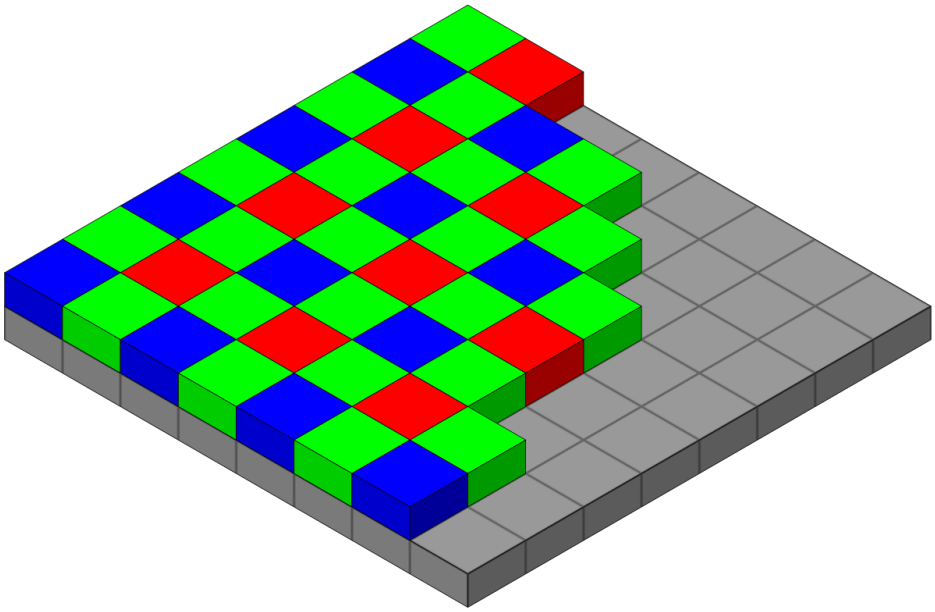

Figure 2.2: Bayer Filter

Table 2.1: Average Surface Temperature Results of a Stationary Ember Image produced by Differing Demosaicing Interpolation Methods

	Ratio Temperature [°C]	**Grayscale Temperature [°C]**
Bilinear	956.44	919.12
Variable Number of Gradients (VNG)	955.15	918.46
Patterned Pixel Grouping (PPG)	956.06	918.60
Adaptive Homogeneity-Directed (AHD)	955.62	918.62

The pyrometry methods considered in this body of work are based on a calibration against a blackbody furnace, conducted by references [22, 8] with the specific imaging devices used in this analysis. The specific blackbody furnace, an Oriel Blackbody Furnace Model 67032, has an operating temperature range of 50 to 1200 $^{\circ}C$ and a cavity emissivity of 0.99 ± 0.01 [25]. Images are captured of this blackbody furnace's aperture at differing

temperatures and camera settings, which are used to first develop a normalization process to ensure that pyrometry results are independent of camera settings and then develop an empirical relationship between these normalized pixel intensities and temperature. A representative image of this blackbody furnace is shown in Figure 2.3.

Figure 2.3: Oriel Model 67032 Blackbody Furnace

The driving principle behind color pyrometry is Planck's Law, which generally relates spectral emissivity to the temperature of a black body object. It can be integrated across a range of wavelengths to express general emissive power, such as is done in conventional heat transfer radiation calculations, or expressed in terms of a single wavelength. The sole-wavelength expression of Planck's Law takes the simplified form

$$E_\lambda = \frac{C_1}{\lambda^5[exp(\frac{C_2}{\lambda T}) - 1]}, \tag{2.1}$$

where T refers to the temperature of the object, λ refers to the wavelength of visible light produced by the object, C_1 refers to the First Radiation Constant with a constant value of $3.742 * 10^{-16}\ W - m^2$, and C_2 refers to the Second Radiation Constant with a constant value

of 0.01439 $m - K$. The spectral response range of the Sony DSC-RX10 III camera used for this analysis is 430nm to 680nm, with 430nm corresponding to visible blue light and 680nm corresponding to visible red light [40]. Because the visible light produced by the embers considered is primarily red, when evaluating this expression within the context of ember pyrometry an approximated wavelength value of 680nm can be inputted to the expression while maintaining a high degree of accuracy [22]. To apply Planck's Law, which in the shown form is relevant to a blackbody object with a surface emissivity of $\varepsilon = 1$, to a realistic gray body with $\varepsilon < 1$, the spectral emissivity can simply be multiplied by the emissivity of the object and the medium transmissivity between the gray body and imaging sensor [22]. Following from this, it is evident that when the quotient is taken between two spectral emissivity wavelengths, such as is done in the Ratio Pyrometry approach presented here, the object emissivity/medium transmissivity will cancel and any operation stemming from the resulting quotient will therefore not be dependent on these two parameters. The key assumption in this derivation is that the exponential term in the denominator of the Planck's Law expression is significantly larger than 1, which is the case for an inputted wavelength of 680nm and the considered temperature range of 600-1200 degrees $°C$. For example, with a worst-case temperature of 1200 $°C$ in this regard, a dimensionless exponential term of magnitude 4.56e7 is produced. The benefit of this simple derivation is that it verifies that the temperature of an object with an unknown emissivity and transmissivity (such as would be expected in an unknown ambient environment or with a charring and ash-generating material) can be determined directly with Ratio Pyrometry. While the pixel intensity recorded at the CMOS camera chip and the spectral emissivity do not hold the same magnitude, being that the CMOS photovoltaic chip outputs voltages corresponding to differing light intensities, they fundamentally represent the same concept of spectral emissivity and therefore can be related through Planck's Law [22, 8].

The ratio of Green-to-Red pixels is considered for ratio pyrometry here, in accordance with the findings of references [22, 8] - summarily, a value without a dependence on blue

light is desirable for firebrand pyrometry due to the low level of blue light found to be produced by smoldering embers, and moreover the Green/Red curve is found to produce a noticeable logarithmic trend against temperature from the blackbody furnace calibration which is desirable to produce a clear correlation. These ratio curves are shown in Figure 2.4, taken from reference [8]. Of note is that this graphic demonstrate good agreement in calibration for two distinct cameras, and thus validates this method across a range of imaging devices.

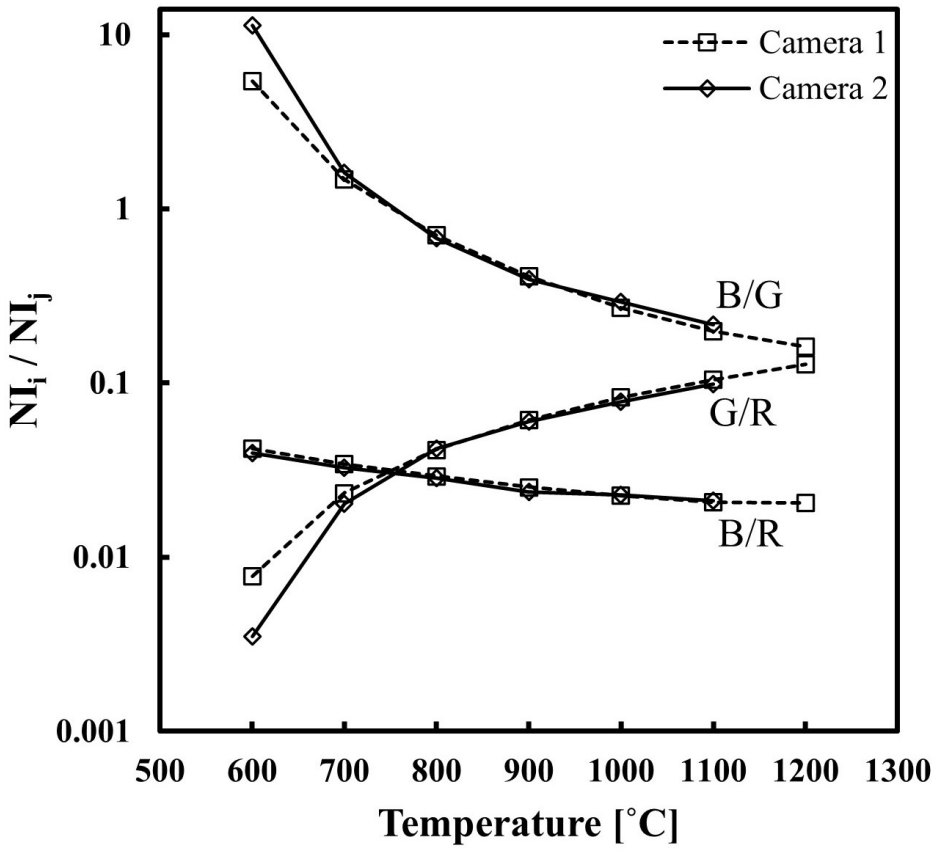

Figure 2.4: Normalized Pixel Intensity Ratio Curves as a function of Blackbody Temperature, from Reference [8]

While pyrometry methods other than Green/Red ratio are of interest, including grayscale and hybrid approaches such as are discussed in references [22, 8], primarily ratio pyrometry is considered in this analysis due to the nature of the images captured. Images of moving embers are considered here - which, in accordance with previous pyrometry investigations with moving objects [26], are primarily limited to providing average temperatures. While

ratio pyrometry has been shown to have a significantly lower Signal-To-Noise ratio than Grayscale pyrometry, which is a pyrometry analysis based on an average of the red, green, and blue pixels and thereby has more consistent results than the ratio of any two channels, it is also shown to have higher accuracy due to its independence on the object's radiative properties as previously described. In addition, because the movement explored in this body of work theoretically serves to physically "smooth" the imaged embers, their surface emissivity will not only be unknown but also difficult to accurately evaluate. From the conjunction of these two factors, the sole use of ratio pyrometry in this consideration of ember movement is justified.

Although not explicitly used in this body of work, of further note is that reference [22] developed a hybrid pyrometry method of the above-described grayscale and ratio pyrometry methods, which takes advantage of simple curve fitting techniques to map the precise, but inaccurate, grayscale pyrometry temperatures to the accurate, but imprecise, ratio pyrometry temperatures and thereby captures the advantages of both methods. Due to ratio pyrometry being the sole method used in this paper, for the above reasons as well as for issues in the grayscale method stemming from uneven pixel exposure on the camera's CMOS chip as considered in Chapter 4, grayscale pyrometry does not hold significance for this work and thus the use of hybrid pyrometry is also prevented.

Pyrometry analysis was conducted in MATLAB, with the same basic methodology documented in references [22, 8]. After being converted to a .TIFF format, the images were loaded into MATLAB, cropped to a manually inputted range, normalized to the camera settings with the equation

$$I_{norm} = \frac{(I - I_{DarkCurrent})(f)^2}{(ISO)(t)}, \tag{2.2}$$

and converted to temperatures using a blackbody furnace calibration equation for Ratio

Pyrometry,

$$T_{Ratio} = 362.73log_{10}(\frac{I_{NG}}{I_{NR}})^3 + 2186.7log_{10}(\frac{I_{NG}}{I_{NR}})^2 + 4466.5log_{10}(\frac{I_{NG}}{I_{NR}}) + 3753.5. \quad (2.3)$$

As previously discussed, the use of Ratio Pyrometry, which is based on the input of the base-10-log of the ratio between normalized green and normalized red pixel intensities, removes the pyrometry analysis' dependence on object emissivity and medium transmissivity and thus ensures the temperature results are accurate despite the uncertainty in ash distribution across the ember when taken in a long-exposure format such as this. Effectively, it produces an average temperature for the ember given that the relatively long exposure time "averages" the pixel intensities received by the CMOS sensor as it captures different regions of the ember surface.

Noise reduction strategies are utilized in the MATLAB pyrometry analysis to improve the quality of the numerical and graphical outputs. One such of these strategies involves considering the 7 pixel by 7 pixel area surrounding each individual pixel, and setting that pixel intensity as null if the majority of the 7-by-7 region is also null. In this manner, noise outside of the ember itself, caused by the ambient environment, is removed and a rudimentary form of ember edge detection is applied. Along a similar vein, threshold values are applied to the raw pixel intensities before calculations are conducted in order to minimize the possibility of ambient pixel intensities in excess of the camera dark current values impacting temperature operations - namely, beyond removing saturated pixels with an intensity magnitude over 65,534, pixels with a green pixel intensity of under 100 are neglected.

Smoothing functionality was provided for the ratio pyrometry method in order to visually reduce the noise caused by the method's low Signal-to-Noise ratio, which allows for the better presentation of results. This methodology is purely visual, and all reported average temperatures are from the unsmoothed ratio pyrometry results. The smoothing was accomplished with a similar mean-based method to the noise reduction previously described

- specifically, by taking the average of all non-zero entries in a 7-by-7 pixel area surrounding each pixel and assigning that pixel's temperature to the averaged value. This is consistent with a similar smoothing method considered in references [22, 8].

3 Apparatus Development & Experimental Methods

3.1 Overview

Firebrand movement is simulated by moving the camera itself while keeping the ember stationary, with the hypothesis that translation of any sort will have the same effect on the CMOS sensor's capabilities. Additionally, keeping the ember stationary allows for a high degree of replicability between trials as well as a comparison to previously documented firebrand surface temperatures [22, 8]. To accomplish this, the camera was rotated about a fixed axis. It was determined that this was the most effective method to accomplish replicable motion due to the intrinsically small footprint of the resulting apparatus as well as the simple modularity associated with pure rotation about an axis. Namely, with this method the simulated speed of the ember can be altered by adjusting the camera's rotation speed and the distance between the ember and the camera focus. The rotating apparatus consisted of a simple "powertrain" composed of a DC motor and a power supply, an Arduino circuit to monitor the apparatus' movement speed and trigger the camera's shutter line, and an applied wind speed to promote cohesive smoldering. The specific mounting methods are shown in Figures 3.1 and 3.2 for horizontal and vertical rotation (specifically without the camera attached for visibility purposes), respectively.

Figure 3.1: Horizontal Rotation Mounting Detail

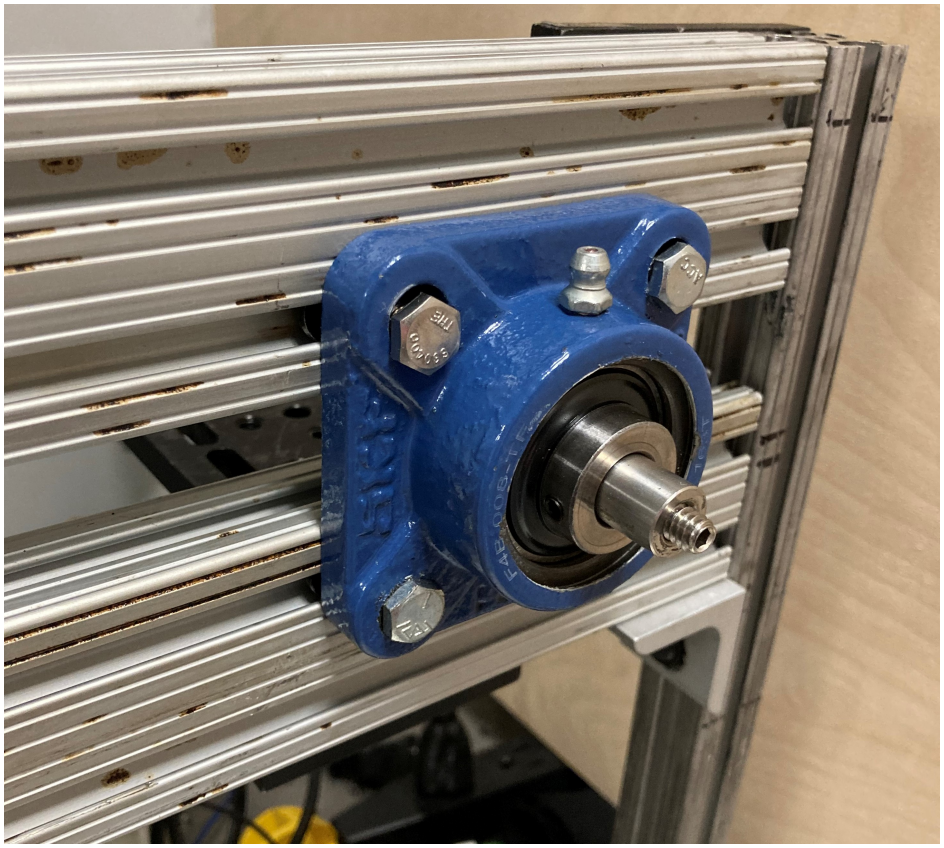

Figure 3.2: Vertical Rotation Mounting Detail

Of particular note for the overall apparatus is the 80-20 brand T-Slot aluminum framing structure, which allows for significant modularity in the camera's mounting position and

orientation. By using this T-slot framing in conjunction with shaft mounts sourced from McMaster-Carr [35], a modular system capable of testing the goals detailed in 4 is developed. The full horizontal mounting orientation is shown in Figure 3.3, the vertical mounting orientation in Figure 3.4, and the overall apparatus is shown in Figure 3.5.

Figure 3.3: Horizontal Rotation Apparatus Orientation

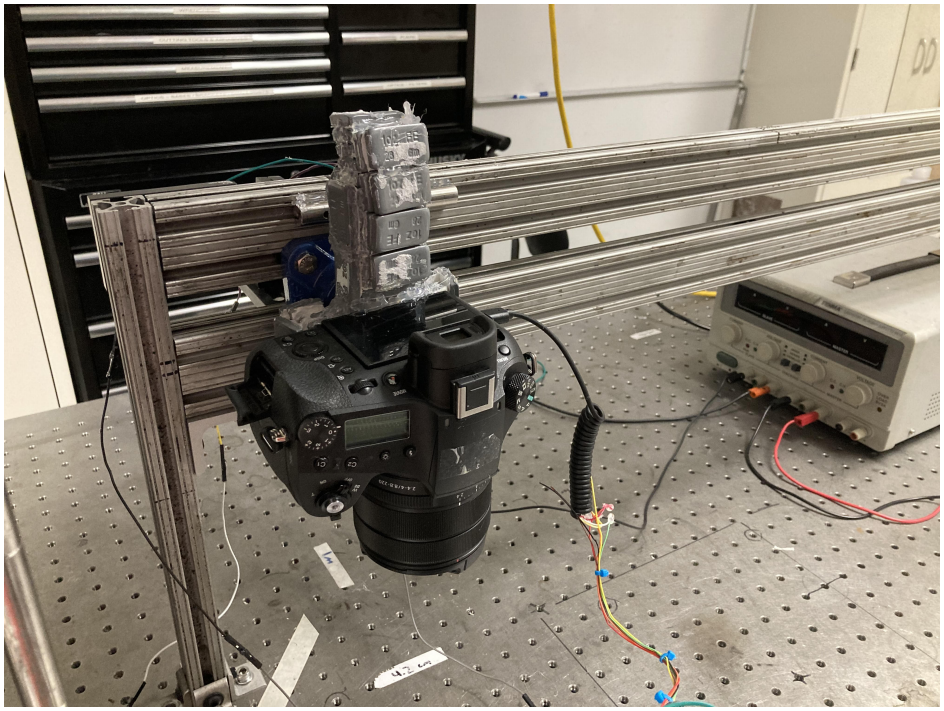

Figure 3.4: Vertical Rotation Apparatus Orientation

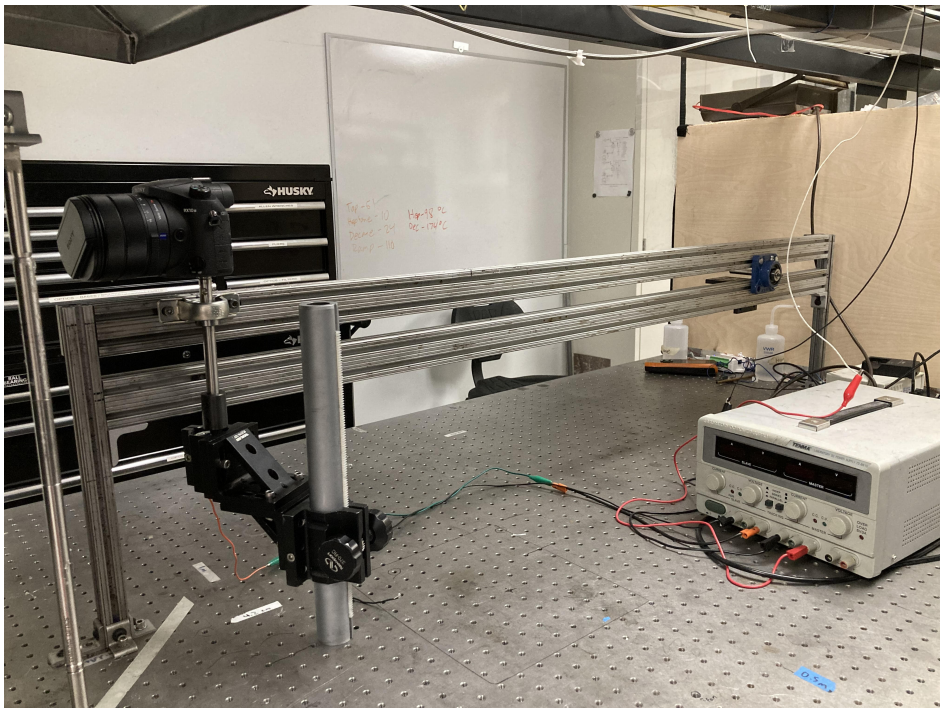

Figure 3.5: Camera Mounting Apparatus

3.2 Power Supply & Motor

Rotation was accomplished through the use of a Direct Current (DC) motor attached directly to a DC power supply, which allowed for rotation speed modulation by simply adjusting the voltage from the power supply. The motor used was a PLUMIA 24V 100RPM 37mm DC Gearmotor, while the DC power supply was a Tenma Laboratory DC Power Supply72-6615 with an output voltage range from 0V to 32V. The control panel of the power supply can be seen in Figure 3.6. The motor was attached to a shaft through the use of a shaft coupling, which in turn was attached to the camera via threaded mounting holes on the bottom of the camera and terminal end of the shaft respectively. The camera was mounted in both horizontal and vertical orientations in this manner, to allow for comparison between the resulting translational behaviors. The DC motor/camera assembly was then attached to the "rail" system made of T-slot aluminum framing, which allowed for the simple movement of the apparatus to varying distances between the ember surface and camera focus. Through this, the results of a previous study [8] investigating the interplay of pyrometry and distance are verified and further developed. The apparatus is capable of creating rotation speeds of 2.5-11 radians per second in the horizontal mounting rotation and 5-8 radians per second in the vertical mounting orientation. The smaller range of speeds in the vertical orientation is due to the counterweights evident in Figure 3.4, which were necessary in order to create a constant rotation speed in this orientation. An in-depth analysis of the effects of these counterweights, for improved aesthetics and simplicity in future uses of this work, can be seen in Appendix J. A multiple-exposure image demonstrating the motion of the camera in its horizontal orientation is shown in Figure 3.7

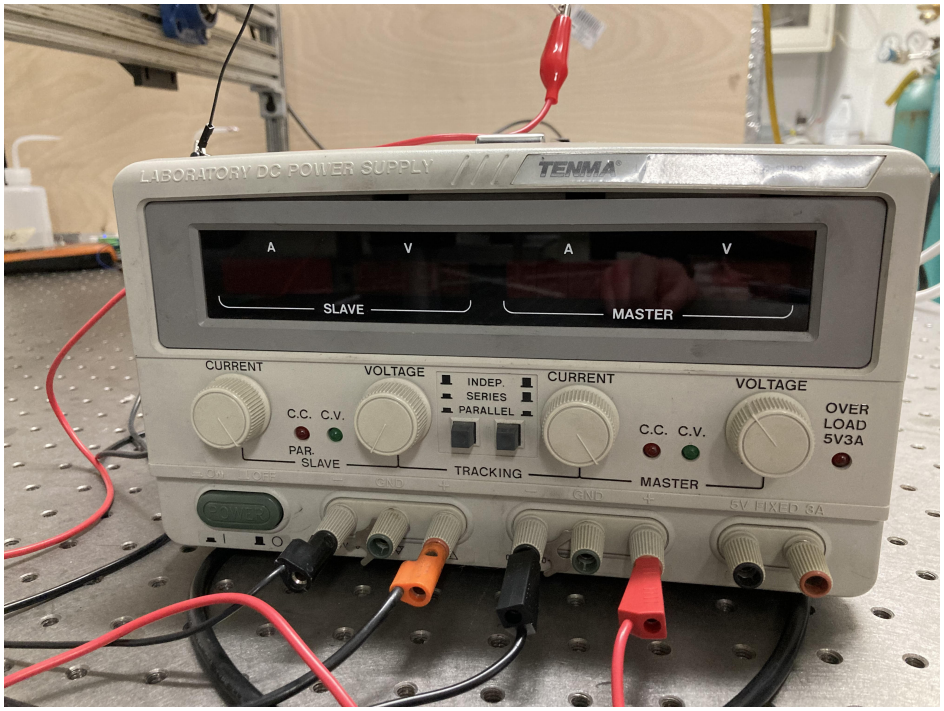

Figure 3.6: Control Interface of the DC Power Supply

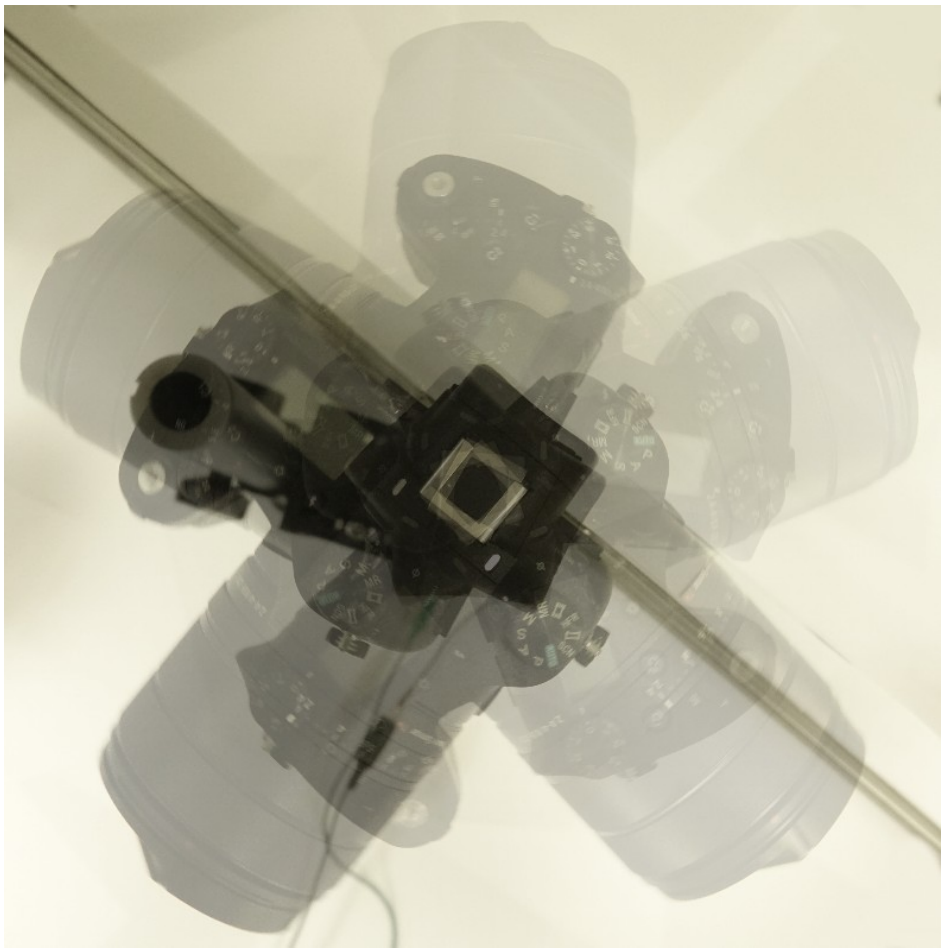

Figure 3.7: Multiple Exposure Representation of Camera Rotation

3.3 Camera Shutter Trigger

The camera's shutter operation was triggered automatically through the use of an Arduino module. The camera's rotation involved the activation of a magnetic Hall Sensor at a single point, triggered by a magnet attached to the camera's mounting shaft, whose signal then activated a shutter trigger cable spliced into the Arduino module. The Hall Sensor installation is shown in Figure 3.8. The Arduino and camera were connected with a slip ring connector, to allow for the camera's movement while keeping the Arduino module stationary and thereby preserving its wiring integrity. In this way, a repeatable manner of triggering the camera shutter at a precise time was created. The timing, both in terms of the camera's shutter speed as well as the Arduino delay between sensor activation and shutter trigger, were designed such to capture the entire sweep of the ember as the camera rotated past in order to minimize the effect of unbalanced light intensities on the CMOS sensor. The goal of this was to potentially allow for grayscale and hybrid pyrometry methods, which have a dependence on pixel intensities, whereas ratio pyrometry results will have no dependence on this potentially unbalanced light intensity due to its basis on a Planck's Law quotient. While capturing these images as streaks may not accurately reflect field conditions, where the camera shutter speed would likely be significantly shorter than those considered here, it was determine to appropriately model a "worst-case" scenario in this context as firebrand speed and the camera shutter speed would be difficult to exactly match in the field and thus exposure streaks will still be created to some degree. Beyond this desire for a conservative model for the targeted behavior, it also provides for a uniform visual basis with which to display results. An estimation for the camera's shutter speed, as well as a presentation of its angular velocity, were calculated based on the Hall sensor operation and outputted to an Arduino Liquid Crystal Display (LCD) module for simplicity. An image of this LCD read-out can be seen in Figure 3.9. A wiring diagram of the LCD Arduino setup can be seen in Figure 3.10, from reference [39]. The trigger mechanism was found to have a response time of approximately 50 ms. Beyond the wiring shown here, which comprises the most complex part

of the system, wiring components include theaforementioned Hall Sensor and the Shutter Trigger Cable (including a relay module). Both of these components are connected to a 5V line and a ground line, with the Hall Sensor connected to an analog pin input and the Shutter Trigger Cable's relay module connected to a digital pin output which serves to connect all 3 of the Shutter Trigger Cable's lines and thereby trigger an image capture if the Hall Sensor's reading exceeds a certain threshold value. The Arduino code used in these experiments can be seen in Appendix G.

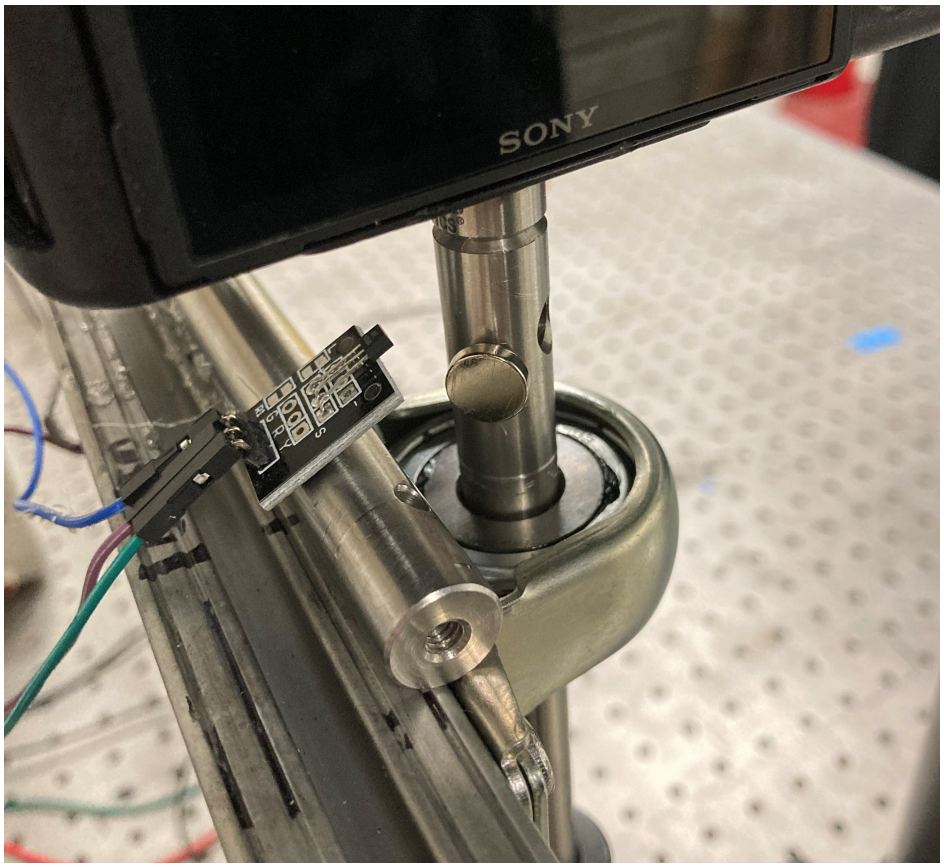

Figure 3.8: Magnetic Hall Sensor Installation

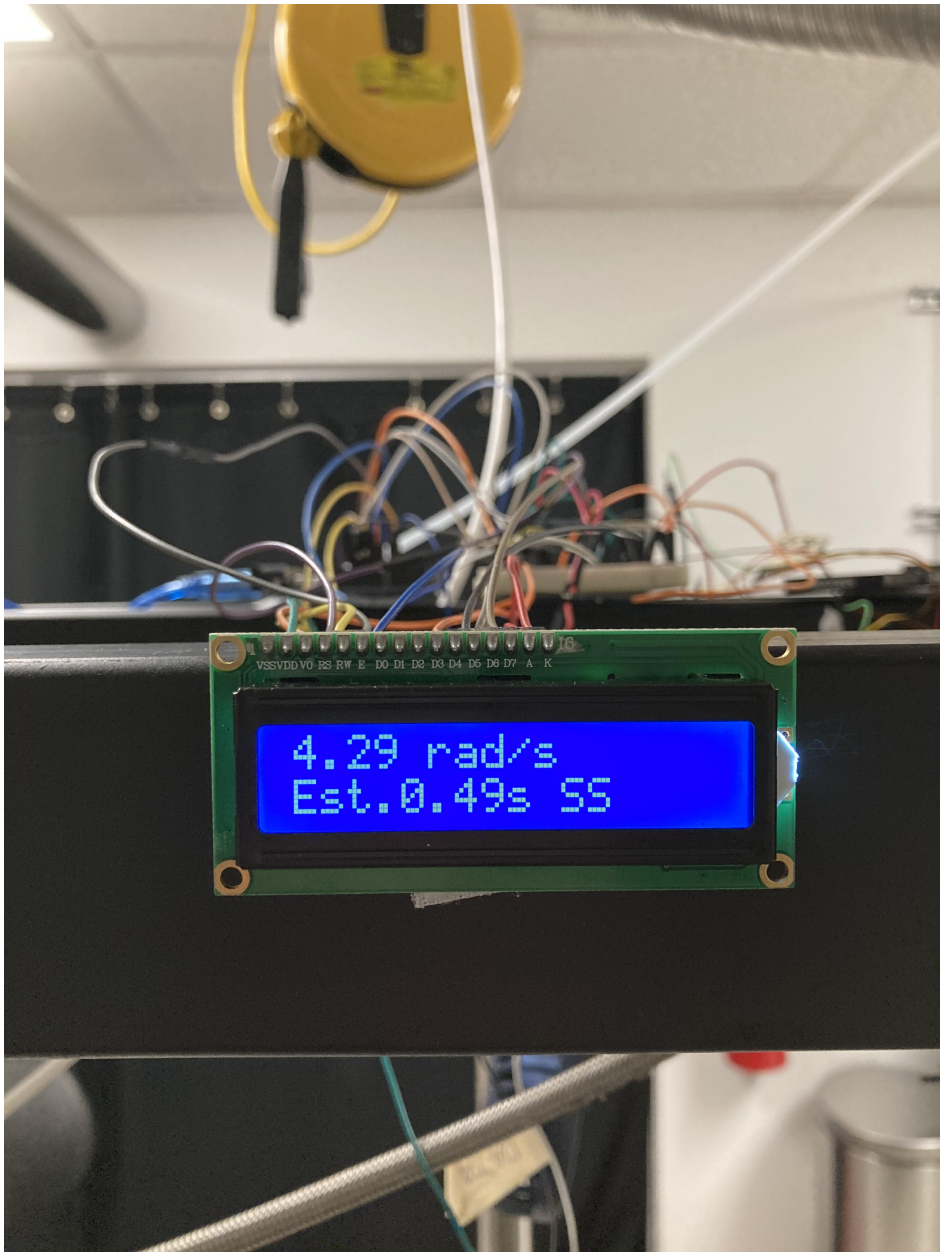

Figure 3.9: Arduino LCD Read-Out

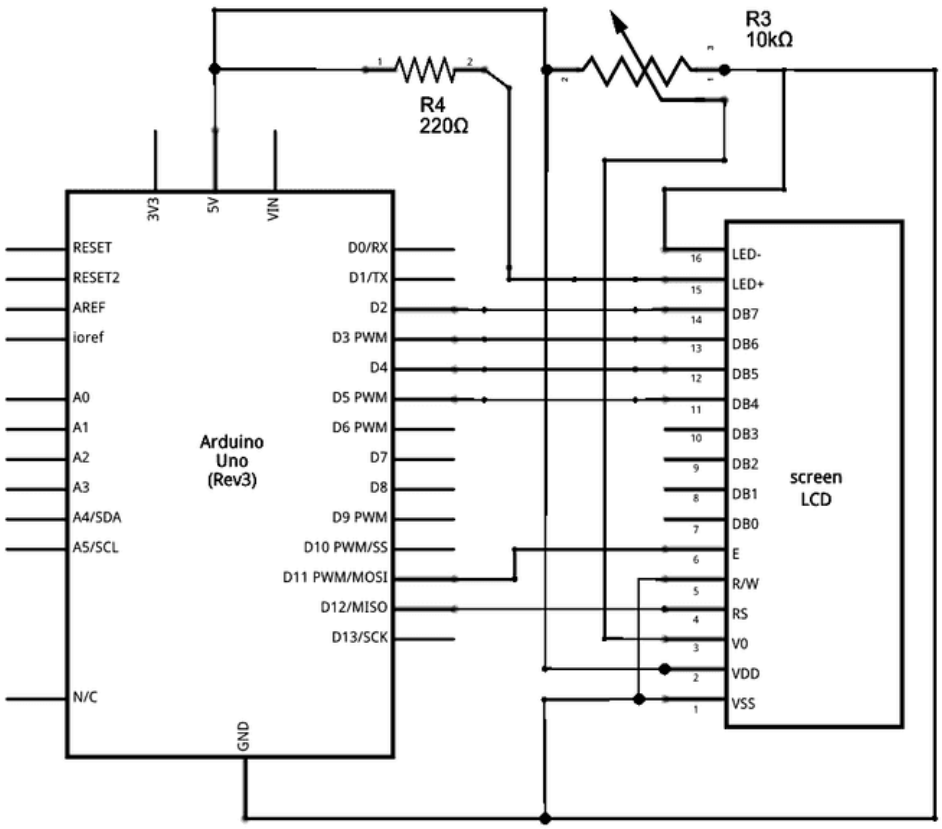

Figure 3.10: Arduino LCD Read-Out Wiring Diagram, from Reference [39]

3.4 Wind Speed Methodology

A fan was directed onto the face of the ember while images were recorded. The fan, a 12mm Noctua NF-F12 iPPC 3000 PWM 4-pin 3000 RPM model computer case fan, was mounted so as to hit the ember at a 30-degree below horizontal orientation and is capable of producing wind speeds of approximately 1 meter per second to 4 meters per second at the ember face. This mounting orientation is in accordance with References [22, 8]. The fan served to promoted smoldering as well as ensured that the results from this series of test could be compared to the previous reference's findings, as wind speed has been show to have a notable positive correlation with ember surface temperature [22, 48]. The wind speed was modulated by directly varying the fan's input voltage with a DC power supply, and wind speed at the ember surface was confirmed with both a HoldPeak HP-866B Rotating Vane Anemometer and an Omega HHF-SD1 Hotwire Anemometer. The specific wind speed

apparatus differs from the aforementioned previous studies [22, 8], where a simple handheld fan was used. This method was found to produce inconsistent wind speeds as the fan's battery depleted, and did not offer significant control over wind speeds - for these reasons, the apparatus was overhauled in order to allow for higher degrees of wind speed accuracy and modularity. Additionally, the new computer case fan apparatus was buffered with wire mesh in order to ensure cohesive flow across the exposed ember face whereas the previous system was noted to create hot and cool demarcations across the ember face due to uneven wind flow distributions. An image of the wind speed apparatus is shown in Figure 3.11.

Figure 3.11: Wind Speed Apparatus Orientation

3.5 Sample Preparation & Mounting

The embers are 6mm diameter Maple wood dowel rods, cut down to approximately 20 centimeter length portions. These criteria were established by Reference [22], and are maintained here for the purpose of consistency with those findings. A single ember is used for each test. The embers were cut to length with a bandsaw, and a 1/8 inch (3.175mm) hole was drilled through their center using a drill press and a simple wooden jig to facilitate mounting. The

exact embers used were found to have a mass of 360.0 ± 30.1 milligrams. A histogram of the ember masses taken from 31 such samples can be seen in Figure 3.12. These samples were conditioned in an oven set to 100 degrees Celsius for 24 hours prior to testing, and stored in a simple desiccation chamber for up to 3 weeks until use. The desiccation was achieved by adding Drierite to the chamber.

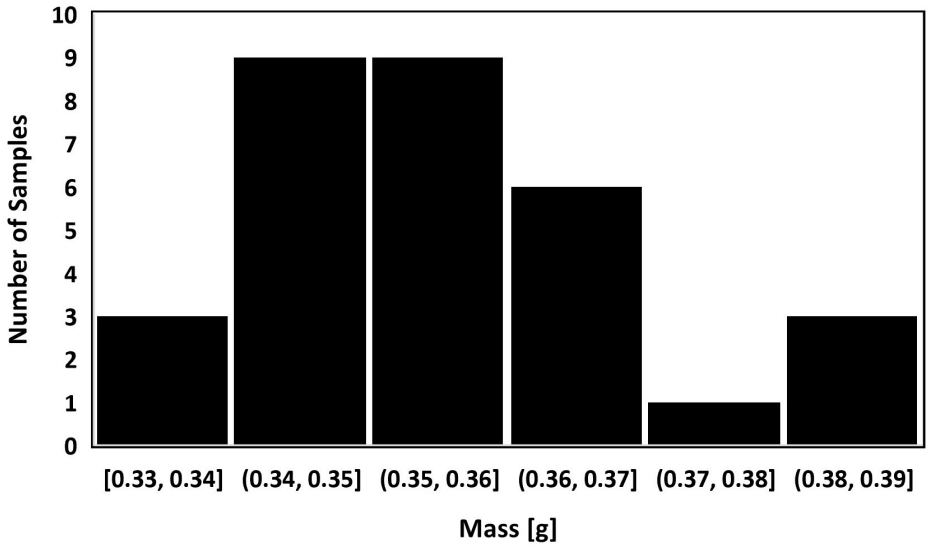

Figure 3.12: Histogram of Ember Masses from 31 Typical Samples

The mounting orientation of the embers involved suspending them between two optical rods, as shown in Figure 3.13. The purpose this was to simulate a realistic firebrand suspended in an air column as closely as possible, as well as to ensure that any quenching effects from contact surfaces are minimized. The ember is supported by two wires in a "X" pattern to minimize the effect of any turbulence from the applied wind speed on its physical constitution throughout the testing process. A deviation from the procedures of references [22, 8] lies in the specific mounting method - while those studies use individual 14 micron Nicalon ™Silicon Carbide (SiC) fibers to suspend the ember, this testing campaign utilized 225 micron Nichrome 80 (80% Nickel, 20% Chromium) wires. While this method evidently produces a more significant potential for ember quenching, through imaging it was found that this change does not appreciably impact the ember surface temperature - in part due to the fact that the wire is only in contact with the center bore of the ember, meaning that

its impact on the outer surface of the ember being measured with pyrometry is negligible compared to the convective and surface radiation effects present on that surface. The reason for this change is that it both simplifies the mounting procedures and makes it more reliable, as the SiC fibers were found to fail regularly during testing and sample preparation. A range of Nichrome wire sizes, ranging from 22 to 36 AWG (644 micron to 127 micron), were evaluated to determine the smallest wire diameter that could reliably support the ember once heated. The Nichrome material was selected due to both its ductility, which simplified mounting operations compared to a stiffer wire material such a steel, and relatively high strength under high temperature conditions. A further idealized consideration of the heat transfer repercussions of this wire mounting deviation can be seen in H, which further validates the experimental finding of equivalent surface temperature results between the mounting methods.

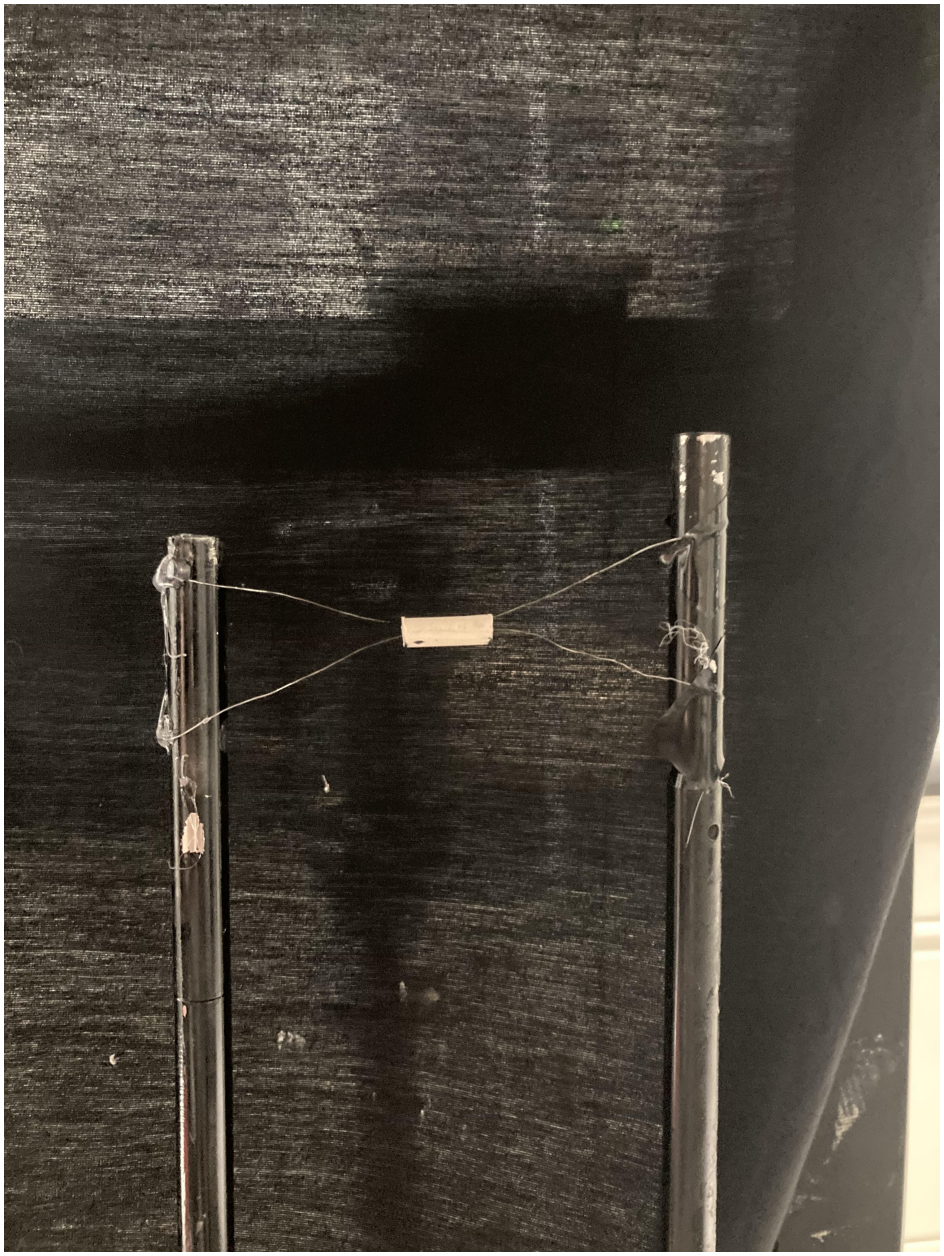

Figure 3.13: Ember Mounting Orientation

3.6 Apparatus Operation Validation

Following construction, the apparatus was validated through imaging a Light Emitting Diode (LED) device connected to DC power. In this manner, a stationary object with a theoretically consistent illuminance is captured, which allows for a consideration of the apparatus' ability to faithfully capture embers (i.e. that apparatus itself does not contribute the any "vibrations" or inconsistencies in the images) as well as of the camera capture timing through

a consideration of the LED's pixel intensities along the streak. A representative streak photo from this analysis can be seen in Figure 3.14, with an accompanying stationary LED photo shown in Figure 3.15 for comparison.

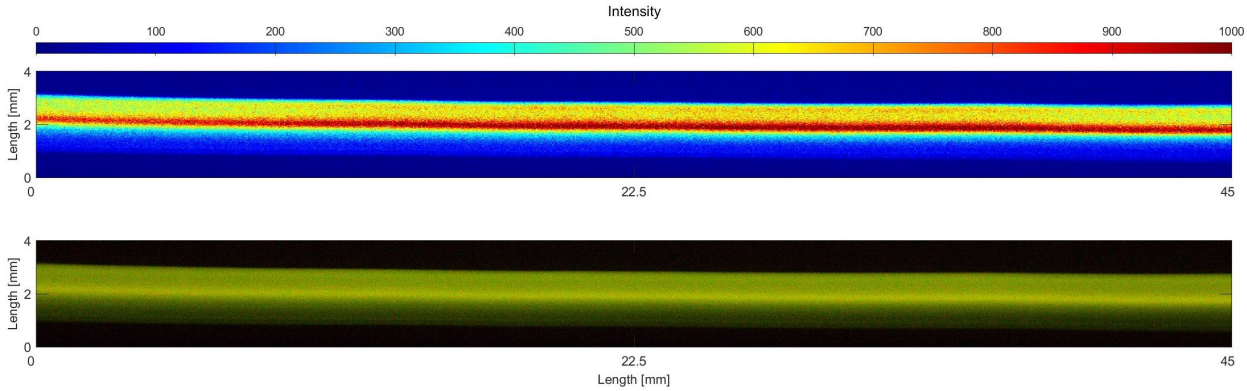

Figure 3.14: Apparatus Validation LED Streak

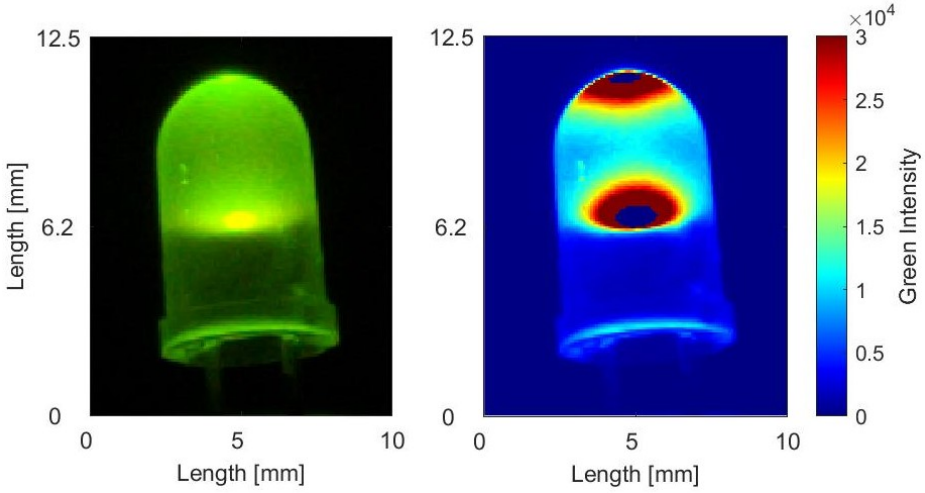

Figure 3.15: Apparatus Validation Stationary LED

Evident in these figures is that, while some key differences between the moving and stationary images are present, a good agreement between the vertical-direction intensities and the LED's true intensity distribution is clear. One major discrepancy between these scenarios is that the top of the stationary LED has an almost complementary brightness to the filament region at the bottom of the LED, whereas the LED streak appears to predominantly capture the bright region of the LED's filament at the base of the bulb and conveys the rest of the bulb as illuminated from that source. The brightness at the top of the image is expected due to the reflection of light occurring at this coalescing point of the bulb. The difference

seen here is attributed to the physical smoothing created by this streak methodology, which better demonstrates the diffusive nature of light in the bulb from the filament. These findings serve to validate that the constructed apparatus can effectively image stationary objects with reasonable fidelity, and that it is capable of capturing the approximate surface distribution behaviors of those objects.

Of note is that, because only the ratio pyrometry method is used in this analysis, the cohesive pixel exposure times targeted in this validation are not strictly necessary for accurate temperature analysis. The reason for this is that, as long as the dark ambient lab conditions have negligible pixel intensities as expected, uneven exposure times will only serve to lower the recorded RGB pixel intensities without actually altering their values. Because of this, ratio pyrometry will still operate as intended. In contrast, grayscale and therefore hybrid pyrometry approaches fail when subjected to these uneven exposure times due to their dependence on general pixel intensity. Although these methods are not considered extensively in this analysis the exposure time validation presented here is still conducted in order to provide a cursory overview of grayscale pyrometry results for this orientation, as well as the pave the way for potential future studies.

3.7 Experimental Methodology

After mounting the conditioned ember, the camera's motion was set at the intended level for the trial. Uniform ignition of the ember was then achieved by passing a butane blow torch over the ember surface for approximately 4 seconds, with a timer beginning at the first moment of torch application. The ember then underwent a period of flaming combustion, which ended approximately 40 seconds after ignition. Immediately after this flaming concluded, the fan was activated to promote cohesive smoldering across the ember face by increasing the rate of the smoldering oxidation reaction through improving oxidizer diffusion into the ember [18]. Once even smoldering was achieved, approximately 45 seconds after ignition, the camera's shutter mechanism was activated by supplying power to the Arduino trigger

mechanism which allowed the magnetic Hall sensor to begin triggering the shutter cyclically as intended. Images were then captured until the ember lost structural integrity and fell off of the mounting wires, a time which appeared to be a unique wind-speed-dependent quantity but generally fell within the range of 60-75 seconds after ignition, or burned to completion. Embers that burned to completion were noted to extinguish approximately 115 seconds after ignition. Higher wind speed generally demonstrated shorter ember lifespans. Images were then transported from the camera's memory card to a storage folder, which was labeled and organized such as to prevent any overlap in trials or uncertainty with camera properties and trial factors. The time between ignition and when imaging began was referred to as "Ignition Offset" and was recorded for use in the time-temperature plots described in Chapter 4.

4 Simulated Movement Results

4.1 Test Campaign Methodology

Tests were conducted in an incremental fashion as shown in Tables 4.1 and 4.2, which are organizational test matrices for the Horizontal and Vertical Rotation trials respectively. In this context, “Horizontal” and ”Vertical” are defined as the plane perpendicular to the camera’s axis of rotation. Each motion orientation was conducted at two wind speeds, 1 meter per second and 2 meters per second, to ensure that comparisons could be drawn to references [22, 8] given the previously discussed uncertainty in their wind speed. The primary goal of this configuration was to rigorously test the relationship between ember movement and distance between the ember and camera focus, in order to verify the findings of reference [8], as well as further develop an understanding of the pyrometry model’s limitations. Test distances were selected to consider the intermediate behavior of those explored in the aforementioned reference, which considered 1 meter, 2 meter, and 4 meter distances [8]. Simulated rotation speeds, calculated by taking the product of the angular velocity and distance from the ember through the traditional rotational mechanics relationship, were selected based on the approximate terminal velocity for embers of this size, noted to be 7-8 meters per second, and subsequently reduced by factors of two. The approach used here was designed to facilitate the observation of a evident empirical relationship between speed and ember temperature, should one exist, as well as capture the behavior of embers moving at speeds slower than their terminal velocity. The terminal velocity was selected as the maximum speed, as opposed to a maximum wildland fire flow velocity for example, as firebrands have been noted to travel at their terminal velocities [45, 22]. Both horizontal and vertical rotation were tested for each distance and speed orientation, within the apparatus’ capabilities. Additionally, a simulated speed of 12 meters per second was tested at the furthest 1.5 meter mounting distance to verify behavior at a theoretical maximum terminal velocity for embers of this size [12]. These firebrand speeds are corroborated by similar firebrand studies utilizing a firebrand

Table 4.1: Test Matrix for the Horizontal Rotation Simulated Movement Speed Trials.

	0.375m	**0.75m**	**1.5m**
2 m/s	5.33 rad/s	2.67 rad/s	1.33 rad/s [1]
4 m/s	10.67 rad/s	5.33 rad/s	2.67 rad/s
8 m/s	21.33 rad/s	10.67 rad/s	5.33 rad/s
12 m/s	32 rad/s	16 rad/s	8 rad/s

Table 4.2: Test Matrix for the Vertical Rotation Simulated Movement Speed Trials.

	0.375m	**0.75m**	**1.5m**
2 m/s	5.33 rad/s	2.67 rad/s [2]	1.33 rad/s
4 m/s	10.67 rad/s	5.33 rad/s	2.67 rad/s
8 m/s	21.33 rad/s	10.67 rad/s	5.33 rad/s
12 m/s	32 rad/s	16 rad/s	8 rad/s

generator, referred to as the Dragon [32]. In the context of this series of experiments, the distance is defined between the ember's surface and the camera focus which removes the lens length as a relevant factor and thereby better allows for future works with different camera orientations. Of note is that this definition of distance differs from the previous works in references [22, 8], which define it between the ember and camera lens face.

4.2 Grayscale Pyrometry Considerations

Representative Grayscale Pyrometry results of an ember streak image are shown below in figure 4.1, with a stationary ember considered with the same pyrometry methodology in figure 4.2 for reference.

[1] Red cells correspond to rotational speeds outside of the apparatus capabilities.

[2] Red cells correspond to rotational speeds outside of the apparatus capabilities.

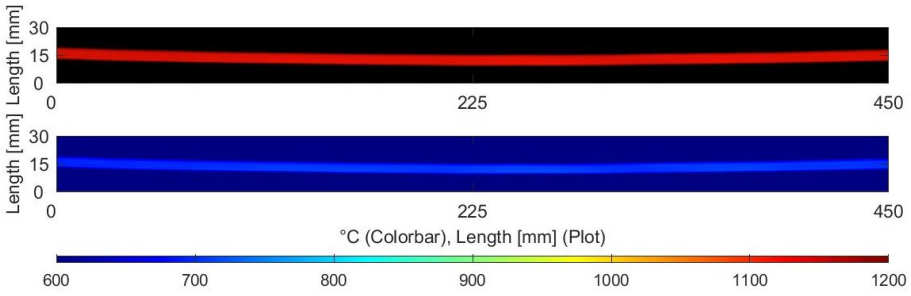

Figure 4.1: Representative Image and Grayscale Pyrometry Temperature Contour of a Full Streak

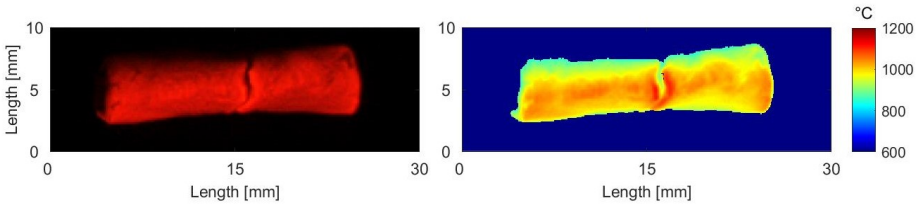

Figure 4.2: Representative Image and Grayscale Pyrometry Temperature Contours of a Stationary Ember

Evidently, the streak image conveys fundamentally different results than the stationary image despite the visual clarity of the streak photo - indicating that the major discrepancy seen here is from the pyrometry analysis method utilized. Further proving this argument are figures 4.8 and 4.11 from later in this discussion of results, which convey these same representative images but analyzed with ratio pyrometry and demonstrating qualitatively good agreement.

It is hypothesized that each pixel in the images effectively receives less exposure time to the ember due to the camera motion, which creates the issue noted above - each part of the image is only exposed to the ember for a portion of the shutter speed, so while the exposure is sufficient to clearly show the ember itself the general intensities are consistently lower in the streaks than in a stationary ember. The pixel intensities are lower in these streak images because each pixel reports voltages corresponding to partial ember exposure and partial null space readings, which is a neccesary drawback with the high shutter speeds neccesary to capture a full ember streak (0.25s - 0.62s). This is also why the streak images are not extremely saturated despite the significantly higher exposure time and ISO settings necessary to capture these images as compared to stationary photographs. Because of this lower

pixel intensity the grayscale temperatures are lower than expected and thus not particularly useful for this application, even beyond the streak image characteristic of primarily reporting average surface temperature information as discussed by [26]. The lower intensities seen here also preclude the use of Hybrid Pyrometry, which relies on the precise grayscale temperature results. Ratio pyrometry temperatures still yield useful and accurate results because it is based on the ratio between intensities, and thus a uniform decrease in intensity yields the same ratio of factors.

4.3 Repeatability Trials

After developing the apparatus and verifying its proper usage with a stationary DC-voltage LED, its repeatability capabilities were assessed by conducting five distinct trials at the same distance, rotation speed, wind speed, and camera setting factors. Specifically, trials were conducted at the 0.375m mounting distance, with a rotational speed of 5.33 radians per second (simulating a 2 meter per second ember speed), a wind speed of 1 meter per second, and camera settings of ISO64, f-2.4, and a 0.5 second shutter speed. The repeatability of the apparatus is assessed by comparing the ratio pyrometry temperature results of the five trials, which are hypothesized to be statistically the same given that all controlled factors did not vary between the experiments. As is discussed further in Chapter 5 of this report, these five trials showed practically identical average surface temperatures and passed statistical tests validating that the distributions are functionally the same. The details of this methodology are presented in that chapter. In this manner, the repeatability of this apparatus' results is validated between trials with constant factors, which allows for other distance, rotation speed, and wind speed orientations to be considered in a single representative trial with reasonable confidence that the individual trial will demonstrate representative results. While this is a first-order approximation, being that a multitude of trials for each orientation would be required to ascertain specific and significant relationships between the factors with true confidence, it allows for brevity in creating an overview of the interplay between the factors.

4.4 Time-Temperature Relationships

The time between ember ignition and the start of image capture was recorded for each trial, which, when coupled with the recorded rotation speed, allows for an approximate Time-Temperature Relationship to be developed for each trial. For this consideration, trials with 1 meter per second wind speed are considered to give an overview of the temporal trends of an ember's average surface temperature. It was decided to consider the 1 meter per second trials over the 2 meter per seconds trials, or both series, because the 2 meter per second trials demonstrate a higher degree of noise when evaluating the behavior of a series of images while demonstrating similar trends to the 1 meter per second trials. The reason for this is that smoldering is more intense in this wind flow regime, which can create larger temporal variations in the ember's average surface temperature with the applied wind speed's turbulent flow. Likewise, only temperature data from the horizontal rotation trials are show for the purpose of brevity in this general consideration of temporal behavior. Plots of the average ember surface temperature for an image against their capture time after ember ignition are show in Figures 4.3, 4.4, 4.5, 4.6, and 4.7 for simulated ember movement speeds of 0 meters per second, 2 meters per second, 4 meters per second, 8 meters per second, and 12 meters per second respectively.

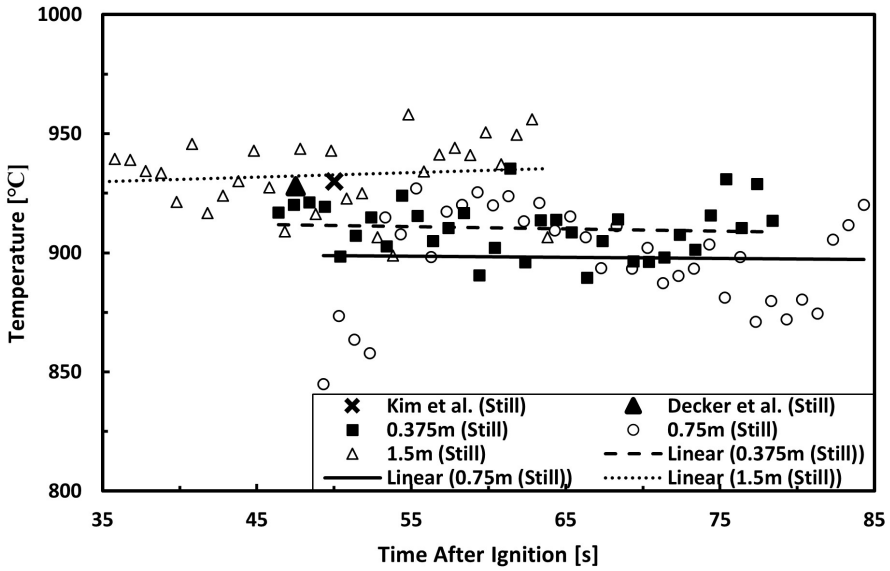

Figure 4.3: Time-Temperature Relationship for Stationary Images under 1 m/s Wind

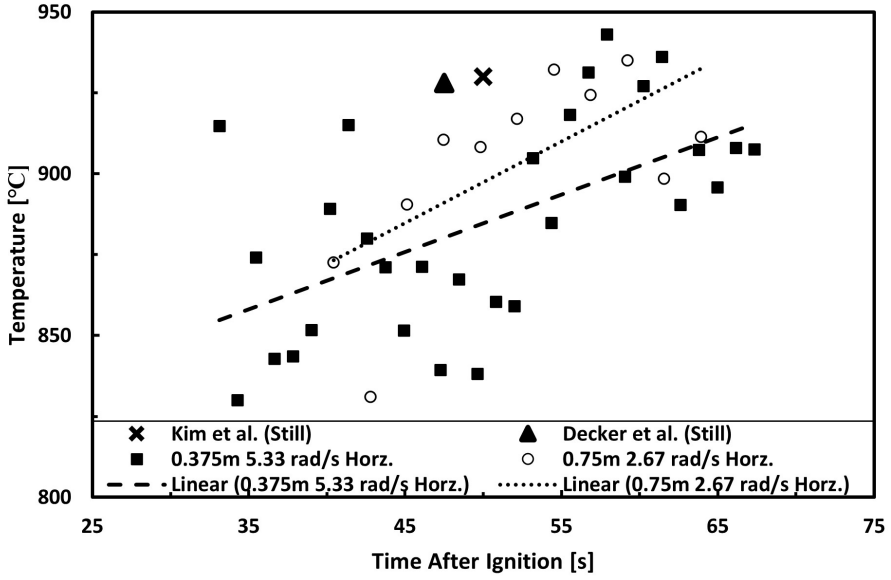

Figure 4.4: Time-Temperature Relationship for 2 m/s Horizontal Rotation Simulated Speed under 1 m/s Wind

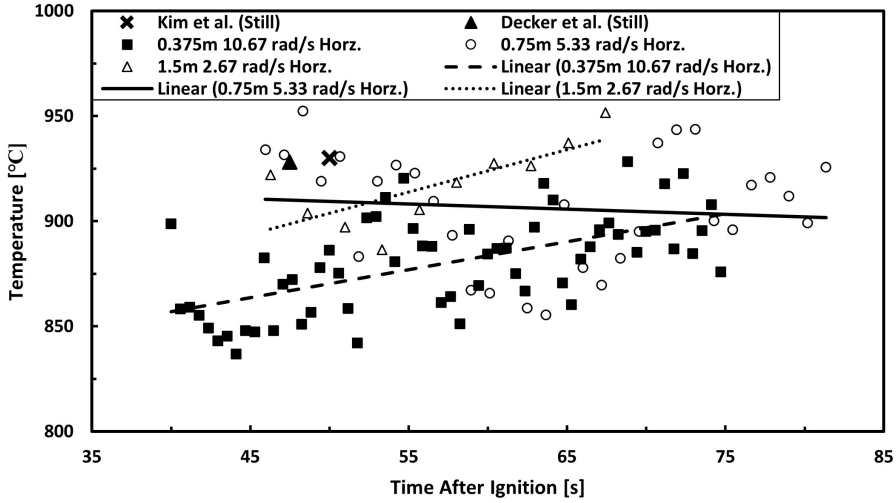

Figure 4.5: Time-Temperature Relationship for 4 m/s Horizontal Rotation Simulated Speed under 1 m/s Wind

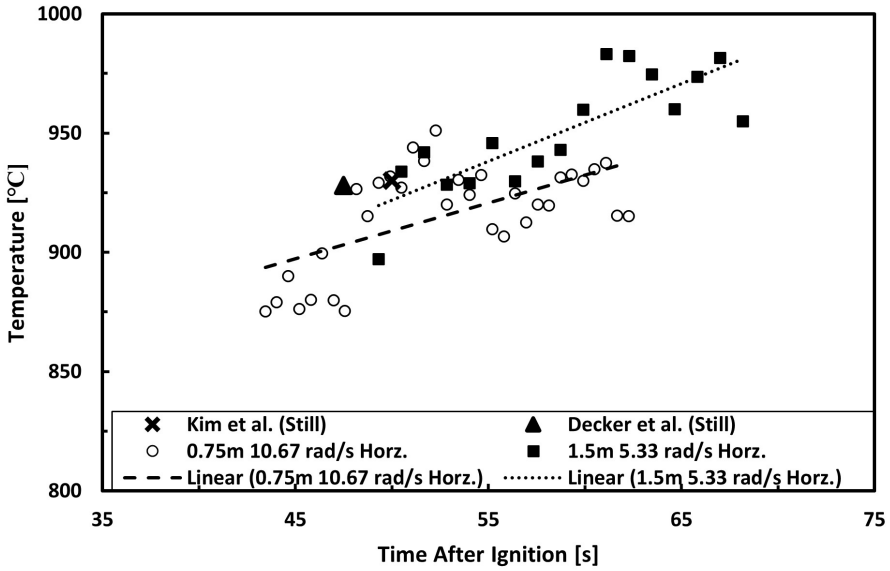

Figure 4.6: Time-Temperature Relationship for 8 m/s Horizontal Rotation Simulated Speed under 1 m/s Wind

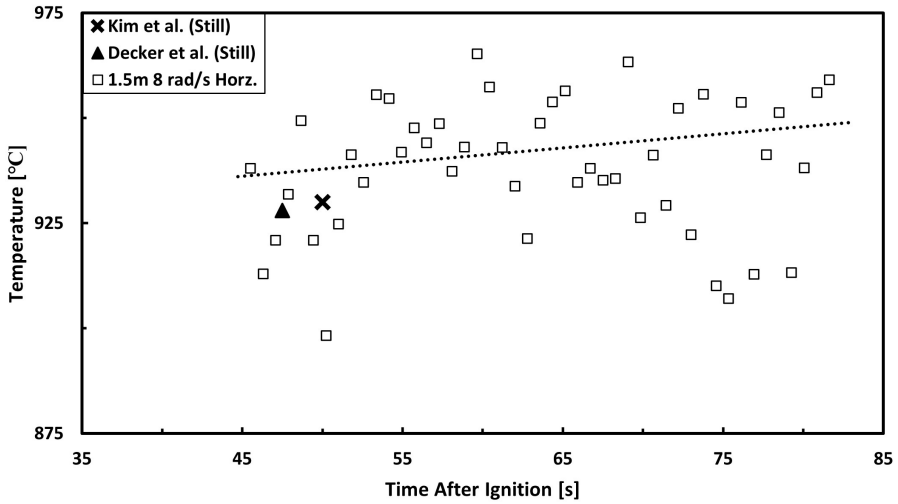

Figure 4.7: Time-Temperature Relationship for 12 m/s Horizontal Rotation Simulated Speed under 1 m/s Wind

The trendlines included with each data set indicate that the average surface temperature of the embers changes with time. These fluctuations do not appear to follow any particular trend, as demonstrated above. It is hypothesized that these fluctuations are primarily due to turbulence in the applied wind speed as well as the accumulation and loss of ash as the embers smolder, as well as potentially due to bulk fluctuations in the laboratory testing environment such as drafts and ventilation. The complexity, and almost random occurrence,

of these phenomena lend credence to the lack of significant pattern in the time-temperature relationships. This relationship was considered for vertical rotation and 2 meter per second wind speed with similar results, lending credence to the decision to display only the horizontal 1 meter per second wind speed results for the sake of brevity - more specifically, they illustrate the quasi-random nature of the ember's surface temperatures adequately and provide context for the further findings of this body of work. Overall trends, in terms of average surface temperatures seen over the course of the trials, can be seen in the subsequent section of this report.

Also of note is that, due to this quasi-random time-temperature relationship that is unique to each ember, calculating conventional error metrics between images captured of the same ember holds little value because they do not display Gaussian distribution behavior as is often assumed in such calculations. Likewise, error metrics within each image are not of significant meaning due to the large number of data points in each image (on the order of several million, dependent on the image mounting orientation and distance) which serves to drive down the standard error/confidence interval parameters used to conventionally convey measurement uncertainty. The standard deviation displayed in these plots is approximately in accordance with the ratio pyrometry Signal to Noise ratio discussed in references [22, 8], and is discussed in further detail in Chapter 5 of this report which considers the Histograms produced by the ember temperatures in single images.

Of additional note in these trials is that, despite their clear temporal fluctuations, and general agreement is shown with the summarized results of previous studies in all simulated movement cases [22, 8]. Not only does this indicate that the surface temperature estimated with pyrometry is independent of movement speed, such as is considered in more depth in the following subsection as well as statistically in the next chapter of this work, it supports a specific definition of "Average Surface Temperature" in the consideration of the interplay between the factors considered in this testing campaign - by averaging the ember surface temperatures spatially, such as is considered in these time-temperature plots, as well as

temporally across the entire ember observation period, a metric is developed that captures the heat transfer potential of an ember throughout its "lifespan" and thus serves as a more realistic value for use in modeling.

4.5 Distance and Rotation Speed Relationship Results

The goal of this section is to both quantify and qualitatively evaluate the surface temperature characteristics of the captured streak images, both across an individual ember surface captured at a single point in time as well as comprehensively across its lifespan, and thereby provide an understanding of the general dependence and behaviors of this surface temperature. The analysis presented here serves as a qualitative overview of these results, whose dependencies are then quantitatively considered with statistics in Chapter 5.

A representative image of an entire streak is shown in Figure 4.8, while cropped representative streaks for horizontal and vertical rotation trials at differing distances are shown in Figures 4.9 and 4.10 respectively. Corresponding Ratio Pyrometry temperature contours are shown adjacent to the captured images. The scaling of these photos was done by imaging a conventional ruler at the respective distances, and thereby ascertaining a pixel-to-millimeter conversion factor for each case. For visual comparison, a similar array of images for a stationary ember captured at a focal distance of 0.375m is shown in 4.11.

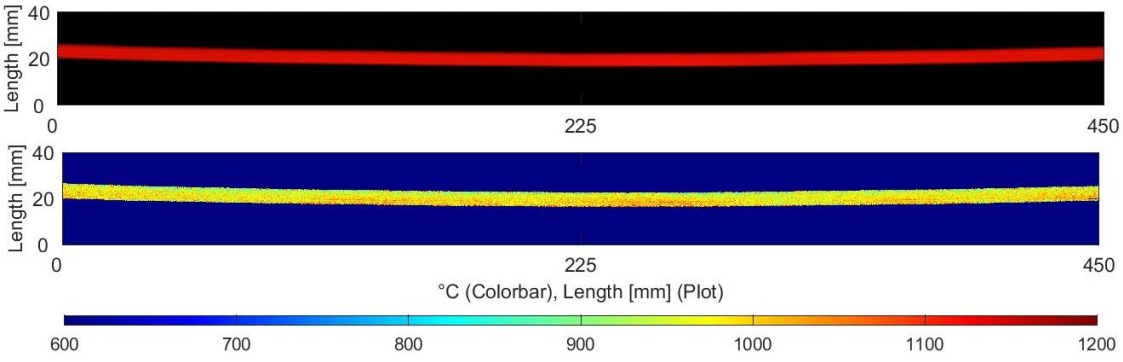

Figure 4.8: Representative Image and Ratio Pyrometry Temperature Contour of a Full Streak

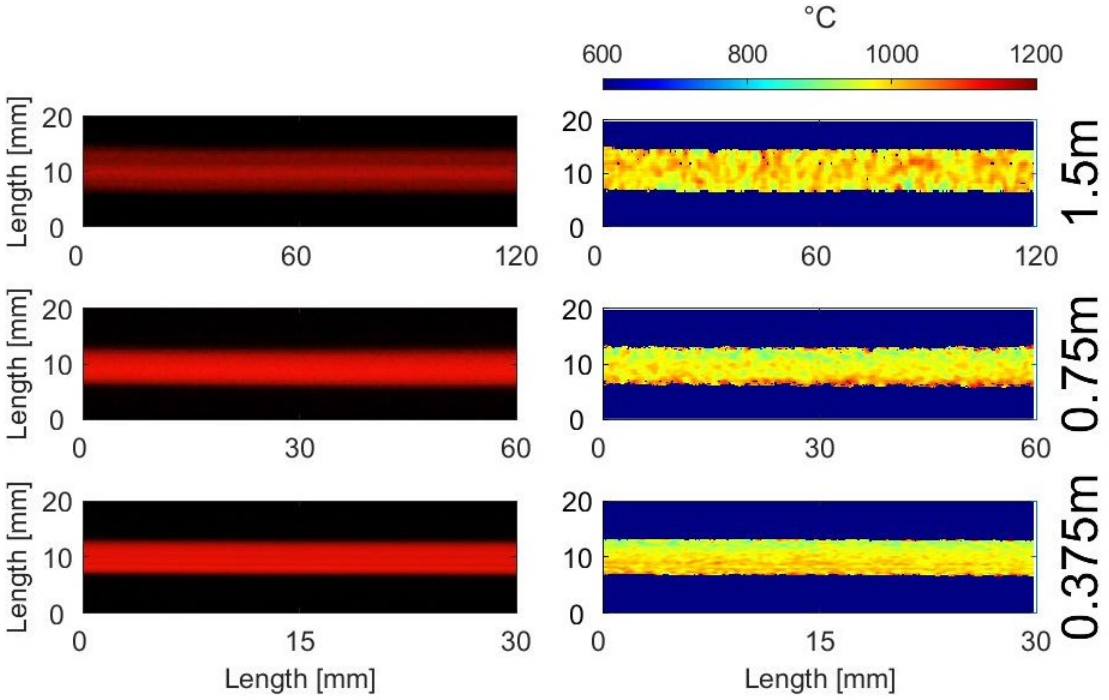

Figure 4.9: Representative Images and Ratio Pyrometry Temperature Contours of Cropped Vertical Streaks at Varying Distances

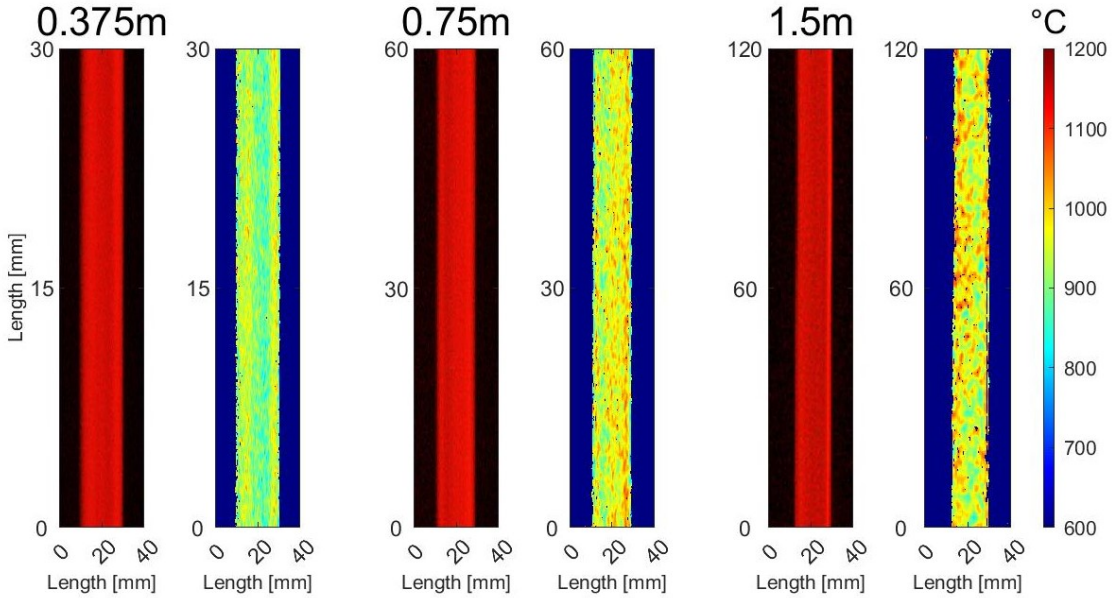

Figure 4.10: Representative Images and Ratio Pyrometry Temperature Contours of Cropped Vertical Streaks at Varying Distances

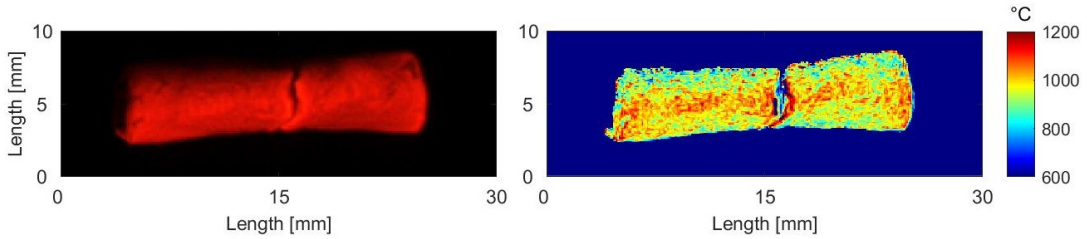

Figure 4.11: Representative Image and Unsmoothed Ratio Pyrometry Temperature Contours of a Stationary Ember

Evident in these streaks are relatively cohesive temperature distributions, as indicated by the previously considered LED validation imaging. While there is some discrepancy in the bulk temperature of the streak from top to bottom, particularly evident in 4.8 due to an uneven application of wind speed from turbulence, the streaks primarily provide average surface temperatures due to the physical smoothing caused by the high shutter speeds (0.25s - 0.62s) necessary to capture the full streaks. These findings are consistent with the movement images considered in [26]. Also of note is the increase degree of noise present in the further distance images, which is consistent with the findings of reference [8]. This occurrence is attributed to the increase relative presence of ambient pixels at the further distances, which thus makes it so ambient noise has a greater impact on the results as well as that each portion of the ember's surface is captured with less resolution and therefore fidelity.

Beyond these spatially resolved image analysis, the average temperatures of each trial as a function of simulated movement speed were considered. Here the average temperature is defined as the average both spatially and temporally over the course of each ember's lifespan, as defined in the previous section of this analysis. In this manner, a qualitative overview of the relationship between temperature, distance, and rotation speed can be ascertained, because the latter two factors are the constituent parts of simulated movement speed. The results of this analysis can be seen in Figures 4.12 and 4.13, for a 1 meter per second wind speed and a 2 meter per second wind speed respectively. Also shown on these plots are the average of all trial's mean temperatures, as well as the Root Mean Square Error (RMSE) and Signal-to-Noise ratio (SNR) amongst the trial averages.

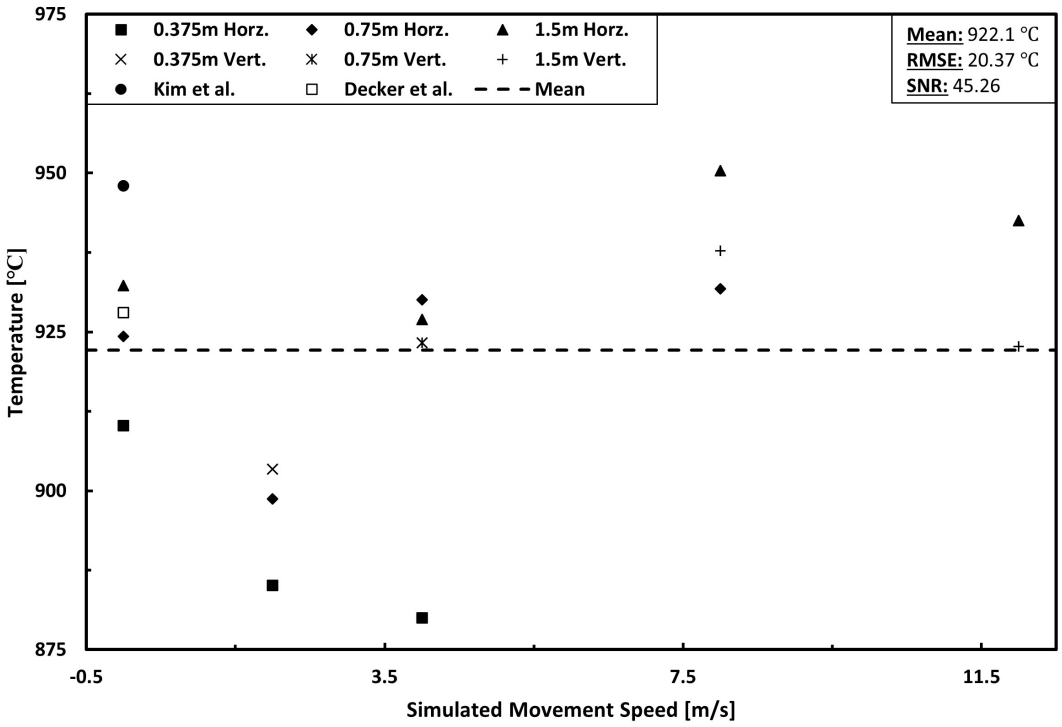

Figure 4.12: Average Surface Temperature as a function of Simulated Movement Speed under 1 m/s Wind

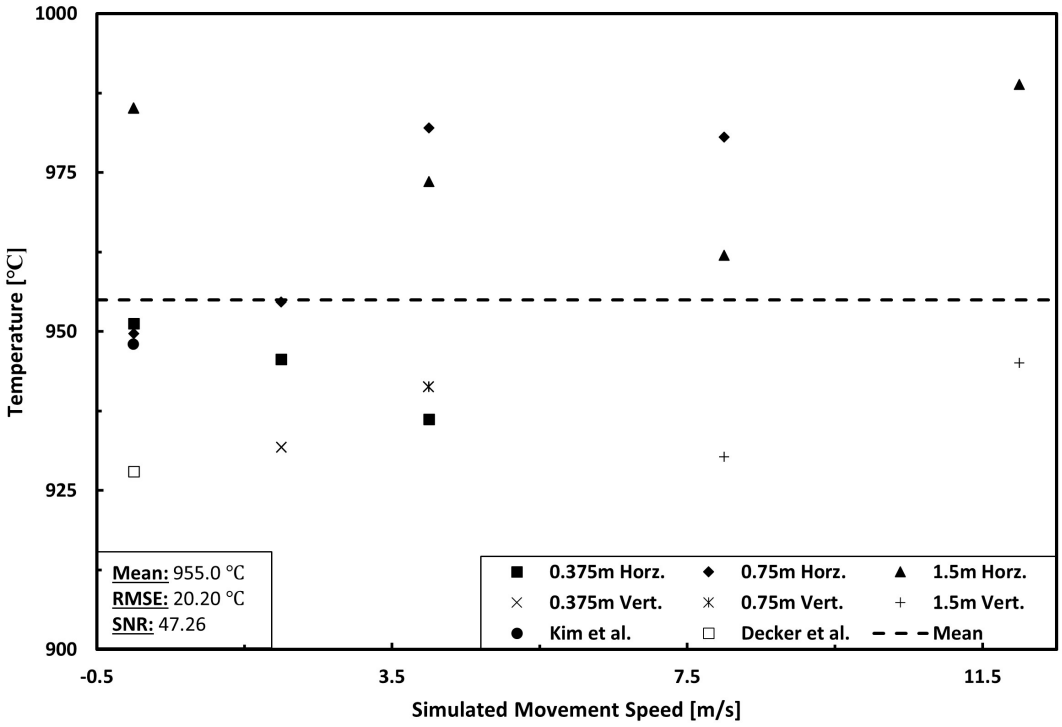

Figure 4.13: Average Surface Temperature as a function of Simulated Movement Speed under 2 m/s Wind

As is qualitatively evident in these plots, the average surface temperature results across the ember's lifespan show little dependence on the simulated speed. While a significant degree of variability is clear, due to the individual time-temperature dependencies for each ember which could alter the mean average surface temperatures, these difference appear to be consistent across the simulated speeds considered. These results lend a cursory credence to the assertation that simulated speed has a negligible individual impact on the presented pyrometry analysis method.

In terms of methodology, all pyrometry analysis was performed with the MATLAB code shown in Appendix A and all contour plots were generated with the MATLAB code shown in Appendix F.

5 Simulated Movement Statistical Analysis

5.1 Methodology

Following the collection and qualitative analysis of data, the overall goal of considering the individual contribution of ember movement to the considered pyrometry model is evaluated through a statistical analysis of the results. Specifically, the average surface temperatures of the embers from trials of differing experimental factors were considered to further ascertain if these factors have any appreciable impact on the pyrometry results. Probability histograms were also fitted to each image's pixel temperature readings, which were then used to evaluate the statistical similarities between images. Probability Density Function (PDF) fits of these histograms were also considered to characterize the general form of ember surface temperature distributions, and to provide for approximated distribution similarity testing. To this end, two statistical methods were considered - mean testing, primarily through Analysis of Variance (ANOVA) tests [13], and non-parametric distribution testing, via the Kolmogorov-Smirnov (KS) Test [20] and the Mann-Whitney U-Test (MWU) (also known as the Wilcoxon Rank Sum Test) [24].

The ANOVA test considers multiple data sets, here the average temperatures resulting from the factorial trials considering mounting orientation, wind speed, simulated speed, and distance, and assesses how likely it is that their means are from the same distribution. Because this test focuses on mean values of the distributions, it is used to compare the average temperatures from a range of streak photos from varying orientations to a stationary image. The reason for this is that, while the mean temperature values at a specific wind speed would statistically come from the same distribution if these factors truly have no impact on the pyrometry model, the streak photos "smooth" the embers and therefore their PDF values are expected to be fundamentally different from those of a stationary ember without this effective smoothing. For this ANOVA, the null hypothesis is that the PDFs have mean values from the same distribution. The ANOVA analyses detailed in appendices C and D were conducted

by directly inputting the average temperatures results and potential dependency factors into MATLAB - while this is certainly not elegant, it is necessary due to the memory limitations of creating these data points within a single body of code.

In contrast to this ANOVA test of means, the two-sided MWU Test and two-sided KS Test comprehensively evaluates if two entire distributions are the same. These tests are non-parametric, which means that they do not assume a specific statistical distribution (e.g. Gaussian, Weibull, etc.). Two types of test with similar outputs were selected here due to the intrinsically different structures of the methods, which thereby serve to highlight different aspects of the ember's surface temperature probabilities. The MWU Test ranks all values within the data sets sequentially and compares the mean ranks of the data sets, whereas the KS Test focuses on the largest discrepancy between the distributions. Because of these facets, the MWU Test is primarily sensitive to changes in the data median whereas the KS Test is sensitive to almost all factors in a distribution such as curvature and variance as well as the median. Due to these differing sensitivies and the computational ease of implementing the methods, both were considered for the purpose of conducting a comprehensive analysis. The distribution tests are conducted between streak photos of varying distance and rotation speed orientations to evaluate if these factors create differing probabilistic distributions even if their mean values are proven to be consistent with ANOVA. The null hypothesis in both of these tests are that the input distributions are the same. All tests were conducted using MATLAB's in-built statistical analysis tools. The MATLAB code used for the distribution analysis can be seen in Appendix E.

In general it was found that both the simulated streak images and stationary ember images produced approximately Gaussian distributions, as evaluated qualitatively, with occasionaly shifted geometries more reminiscent of Weibull distributions. This finding supports the use of traditional confidence interval analysis on the ember surface temperatures of a single image, and provides for a smaller degree of uncertainty in the consideration of environmental factors in this project because fewer data points will be required to obtain

a reasonably accurate population distribution as is proven by the Central Limit Theorem principle [10].

5.2 Repeatability Trials Analysis

As previously discussed in Chapter 4, five trials were conducted at a set combination of factors to verify the operation of the developed simulated movement apparatus. Specifically, these repeatability trials were conducted at the 0.375m mounting distance with a rotational speed of 5.33 radians per second (simulating a 2 meter per second ember speed), a wind speed of 1 meter per second, and camera settings of ISO64, f-2.4, and a 0.5 second shutter speed. The purpose of this was to verify that the apparatus is repeatable at any one orientation, which then allows for the reasonable extrapolation to other combinations of factors and thereby allow for an overview of the interplay between factors with minimal trials. To verify the repeatability of these trials, ANOVA and both relevant distribution tests were performed.

A one-way ANOVA was conducted with the average temperatures of each trial, where here the average temperature of each image is individually considered. This practice differs from the previous definition of average surface temperature as well as the definition used for ANOVA in the next section, which both take the mean of all image average surface temperatures and thereby create a measure of the ember's temperature characteristics throughout its lifespan. While this spatial and temporal averaging method is more representative of the purpose of pyrometry, here the temperature of each image is used to more directly compare the temporal resolution of these embers while also assessing their average surface temperature characteristics. These values were simply compared to the trial number associated with each measurement, with the physical meaning of the output assessing whether the average temperatures with respect to time could potentially come from the same distribution. Of particular note is that each trial ran for differing lengths of time (dependent on the physical constitution of the ember) and thus, without the time-temperature dependence explicitly accounted for, a strong average surface temperature consistency could be demonstrated if

ANOVA results support the repeatibility of these trials. The result of this ANOVA is that average surface temperature results are independent of specific trial, and thus the repeatibility of the apparatus is validated. Inputs to this ANOVA are not shown for brevity, but are conveyed in Appendix D.

Subsequently, to assess the exact repeatability of the photographs, distribution testing is performed. As previously noted, the temperature of the embers changes with time along with the applied wind's flow and ember ash accumulation, so the same stage of the ember's lifecycle was selected for this comparison. Specifically, tests were conducted on the first and last photographs of each trial, corresponding to the first point of cohesive smoldering and the last point before breakage respectively. The MATLAB code used for this analysis can be seen in Appendix D. The results of both the two-sided KS Tests and the MWU Test can be seen in Tables 5.1 and 5.2, respectively, for the first images captured in each trial. Tables 5.3 and 5.4 show the equivalent results for the last photograph in each trial for the KS Test and MWU Test, respectively. The MATLAB function for the KS Test, kstest2, produces a Boolean output - 1 corresponds to a rejection of the null hypothesis with 95% confidence (which would mean that the histograms are not from the same overall distribution), and 0 corresponds to the null hypothesis. The MWU Test function produces confidence levels, meaning that the null hypothesis is rejected (and the PDF's are not from the same overall distribution) if the produced level is under 0.05 with the same 95% confidence assumption used in the KS test. The blank cells indicate extraneous entries (e.g. the comparison of Trial 2 to Trial 4 is the same as vice-versa, and a Trial 1 to Trial 1 comparison is meaningless). Histogram distributions can be seen in Figures 5.1 and 5.3, with corresponding normal curve fits in Figures 5.2 and 5.4, for the first and last photos of each trial respectively. While the actual data closely corresponds to a normal curve fit, as is displayed, the histograms of the real data are of primary interest due to their direction reflection of reality. Accordingly, only the histograms of the data are presented for consideration of the real trial results - the PDF fits are included here to provide qualitative proof of the approximate distribution of

the data, as well as for the purpose of creating a cohesive and approximated basis across tests for distribution testing as previously described.

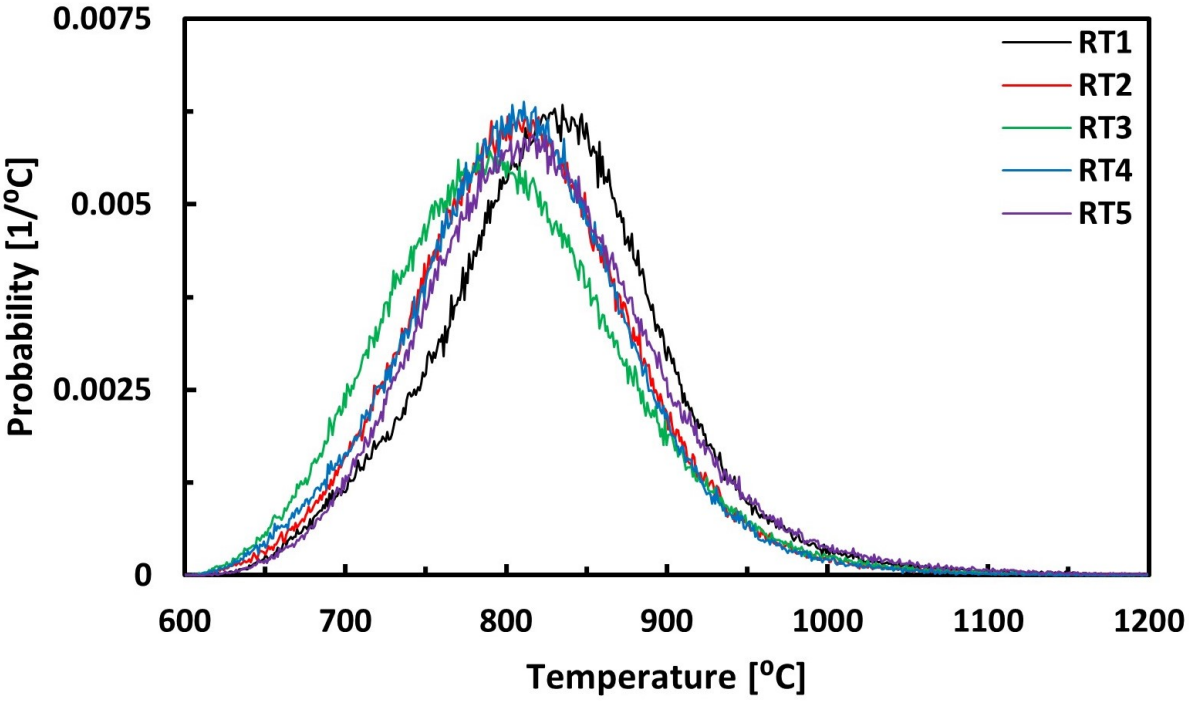

Figure 5.1: Repeatability Trials First Image Histograms

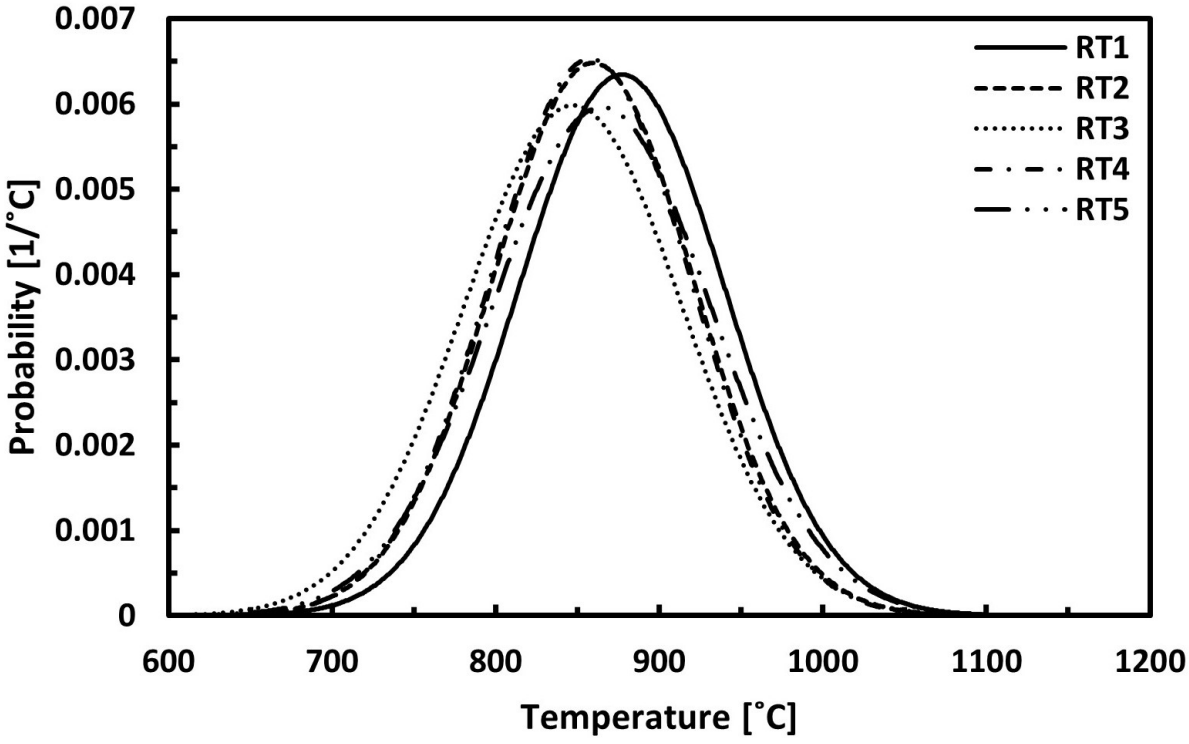

Figure 5.2: Repeatability Trials First Image Probability Density Functions

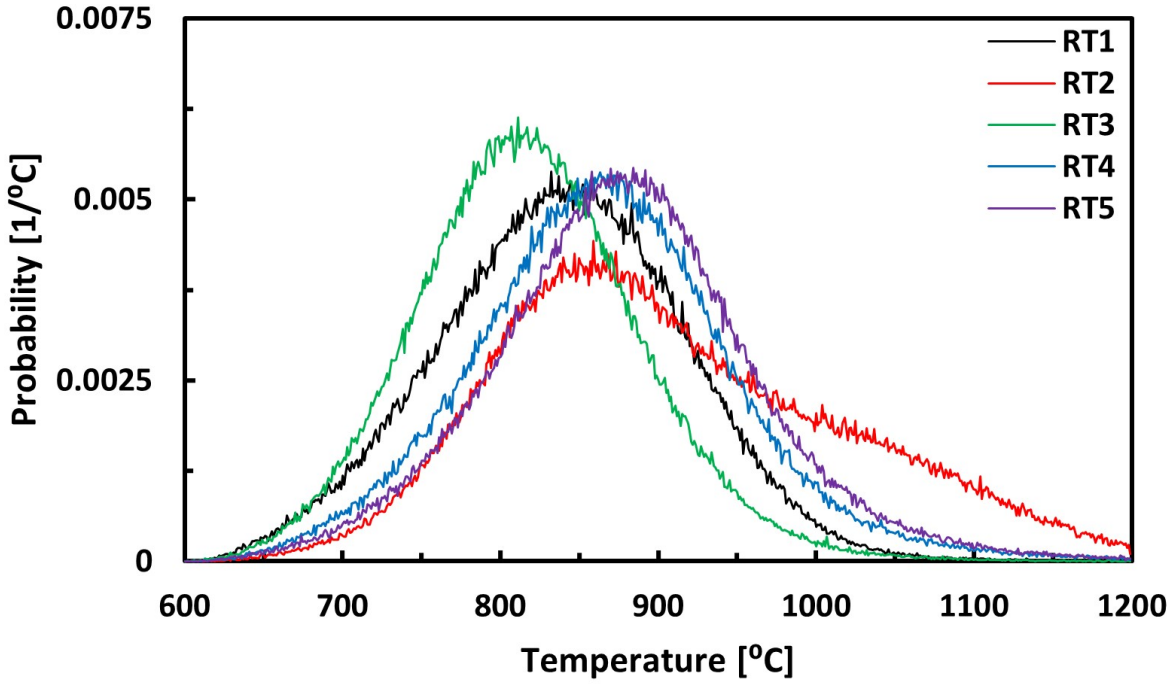

Figure 5.3: Repeatability Trials Last Image Histograms

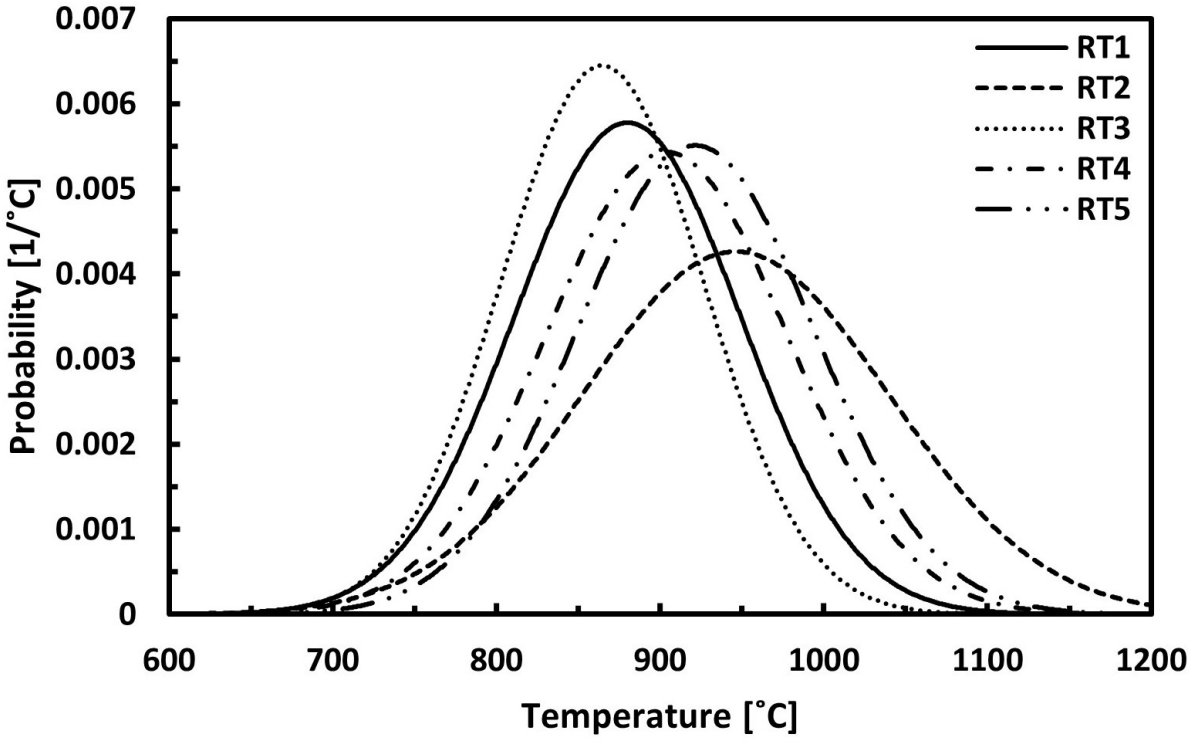

Figure 5.4: Repeatability Trials Last Image Probability Density Functions

Considering the tests conducted on the first images, of note in these results is that both

the KS and MWU tests demonstrate a strong degree of agreement between trials. This agreement is corroborated by the qualitatively similar data histograms. Although Trials 3 and 5 fail both tests within a reasonable degree of confidence compared to the other trials, they still demonstrate agreement with each other which lends credence to a degree of repeatability despite apparent variations between trials. Considering the tests conducted on the last images, a clearer degree of variation between the trials is seen in both the histogram plot and the distribution test results. These variations lend further credence to the variable time-temperature relationship between trials previously discussed, and supports the practice of averaging the ember surface temperatures both spatial and temporally to obtain accurate measurements - because any single point estimate can misrepresent the actual distribution's characteristics. Although Trials 4 and 5 still show a strong degree of similarity in these last image tests, this is dismissed as a coincidental result due to the other statistical disagreements and the approximately similar relationship between all of the recorded ember histograms.

Table 5.1: Repeatability Trials Two-Way Kolmogorov-Smirnov Test Results (First Images)

	Trial 1	**Trial 2**	**Trial 3**	**Trial 4**	**Trial 5**
Trial 1	-	0	1	0	1
Trial 2	-	- 0	1	0	1
Trial 3	-	-	-	1	0
Trial 4	-	- 0	-	-	1
Trial 5	-	-	-	-	-

Table 5.2: Repeatability Trials Mann-Whitney U-Test Results (First Images)

	Trial 1	**Trial 2**	**Trial 3**	**Trial 4**	**Trial 5**
Trial 1	-	0.473	0.471	0.356	0.198
Trial 2	-	-	0.131	0.855	0.043
Trial 3	-	-	-	0.085	0.674
Trial 4	-	-	-	-	0.026
Trial 5	-	-	-	-	-

Table 5.3: Repeatability Trials Two-Way Kolmogorov-Smirnov Test Results (Last Images)

	Trial 1	**Trial 2**	**Trial 3**	**Trial 4**	**Trial 5**
Trial 1	-	1	1	1	1
Trial 2	-	-	1	1	1
Trial 3	-	-	-	1	1
Trial 4	-	-	-	-	0
Trial 5	-	-	-	-	-

Table 5.4: Repeatability Trials Mann-Whitney U-Test Results (Last Images)

	Trial 1	**Trial 2**	**Trial 3**	**Trial 4**	**Trial 5**
Trial 1	-	0	0.005	0.143	0.317
Trial 2	-	-	0	0	0
Trial 3	-	-	-	0	0
Trial 4	-	-	-	-	0.718
Trial 5	-	-	-	-	-

Summarily, in considering these five repeatability trials, it is proven that the designed apparatus can produce repeatable average surface temperature results and probability distributions although these distributions change with time due to unique temporal effects on individual embers such as ash accumulation and wind gusting. Consequently, the apparatus' operation and the practice of recording data at varying orientations with minimal trials, as well as averaging the ember surface temperatures both spatially and temporally, is validated.

5.3 Trial Data ANOVA Analysis

Tables 5.5 and 5.6 reiterate the mean average surface temperature trial results and testing orientations for both wind speeds tested respectively, which were inputted to MATLAB for this n-way ANOVA analysis. The specific MATLAB code used for this analysis can be seen in Appendix C.

Table 5.5: Trial Orientations & Results for ANOVA Input (1 m/s Wind Speed)

Orientation	**Simulated Speed [m/s]**	**Distance [m]**	**Avg. Surface Temperature [°C]**
Horz	0	1.5	932.4
		0.75	910.2
		0.375	924.3
		1	948
		0.01	928
	2	0.375	885.1
		0.75	898.7
	4	0.375	880.0
		0.75	930.1
		1.5	927.0
	8	0.75	931.8
		1.5	950.4
	12	1.5	942.5
Vert	2	0.375	903.4
	4	0.75	923.3
	8	1.5	937.8
	12	1.5	922.7

Table 5.6: Trial Orientations & Results for ANOVA Input (2 m/s Wind Speed)

Orientation	**Simulated Speed [m/s]**	**Distance [m]**	**Avg. Surface Temperature [°C]**
Horz	0	1.5	985.1
		0.75	949.7
		0.375	951.3
		1	948
		0.01	928
	2	0.375	945.6
		0.75	954.7
	4	0.375	936.2
		0.75	982.0
		1.5	973.6
	8	0.75	980.6
		1.5	962.0
	12	1.5	988.8
Vert	2	0.375	931.8
	4	0.75	941.2
	8	1.5	930.3
	12	1.5	945.1

The results of this ANOVA are as hypothesized - wind speed has a significant bearing on the average surface temperature of the firebrands, while the other factors considered have no meaningful impact. Distribution testing is performed between the simulated movement and stationary images in the next section of this analysis as a form of contextualization for those results - despite this consideration, the streak and stationary images are not hypothesized to have distribution agreements because they are expected to demonstrate fundamentally different temperature distributions, despite their agreement in mean results, due to the factor of uncertain exposure time in the simulated movement images.

While the above 3-way ANOVA analysis proves that the only factor significant impacting the mean average surface temperature is the applied wind speed, common practice indicates that a follow-up analysis considering the dependence of the mean average surface temperature on each individual factor is warranted to minimize the chance for false dependency

results. To accomplish this, the Bonferroni-Holm Correction for multiple comparison cases is considered [14]. This correction method compares the significance levels produced by the original ANOVA analysis to better consider the impact of the individual factors, and the variations within those factors, on the final surface temperature results. In this manner, it was further verified that Wind Speed is the only factor with a significant bearing on the mean average surface temperature results. 1-way ANOVA analyses between the average temperatures and the individual apparatus factors, which is effectively a series of Student T-Tests [10], also validate this finding.

5.4 Trial Data Distribution Considerations

Following the ANOVA analysis considering the dependence of the mean average surface temperature on the independent variable factors, non-parametric distribution testing is conducted on the streak PDFs in order to determine their relation to stationary embers and, more specifically, considered if the varied factors show any bearing on the variance of the measurements. It is hypothesized that the further distances and higher speeds will demonstrate a distribution with a higher variance, in accordance with the qualitative findings of Chapter 4 of this body of work. For this analysis, as a cursory overview of this relationship, case with the same simulated speed and wind speed at different distances are considered against a stationary ember captured by reference [22]. Specifically, horizontal streak images with a 1 meter per second applied wind speed and a 4 meter per second simulated speed are considered. Subsequently, to consider the effect of simulated speed, PDFs of embers at the same distance but with different simulated speeds are considered with the same stationary ember. Here, embers captured in the horizontal orientation at the 1.5 meter mounting distance and a 1 meter per second applied wind speed are considered. Accordingly with the time-temperature fluctuations previously noted, all streak images are pulled from approximately the same point in the ember "lifespan", at the first point of cohesive smoldering, to maintain the best possible basis for comparison.

Figures 5.5 and 5.6 show histograms of the above-described orientations, with the reference [22] stationary ember plotted against trials of the same simulated speed but differing distances in 5.5 and trials of the same distance but differing simulated speeds in 5.6. Both histograms feature data from the 1 meter per second applied wind speed data set, again to minimize the potential for visual noise caused by the more intense smoldering at the higher wind speed. Of particular note is that these histograms convey information from a single ember image, as opposed to the temperatures considered in the ANOVA analysis of these trials shown in 5.5 and 5.6 which were averaged both spatially across the ember surface as well as temporally across all images in a single test, as previously discussed in the consideration of the repeatability trial distributions. While the latter orientation is more representative of realistic ember surface temperatures and provides for a better basis for comparison between trials as previously discussed, histograms were unable to be created for this combined information due to computational limitations associated with the significant number of temperature data points that would be associated with such an undertaking. Because of this, the conveyed histograms are expected to show more variation than indicated in the results used in the ANOVA analysis because of the time-temperature dependence of ember's surface temperatures - although, as proven in the consideration of the repeatability trials, by selecting images from the same point in the ember's lifespan a good degree of agreement can still be cultivated barring any outlier effects such as wind gusting.

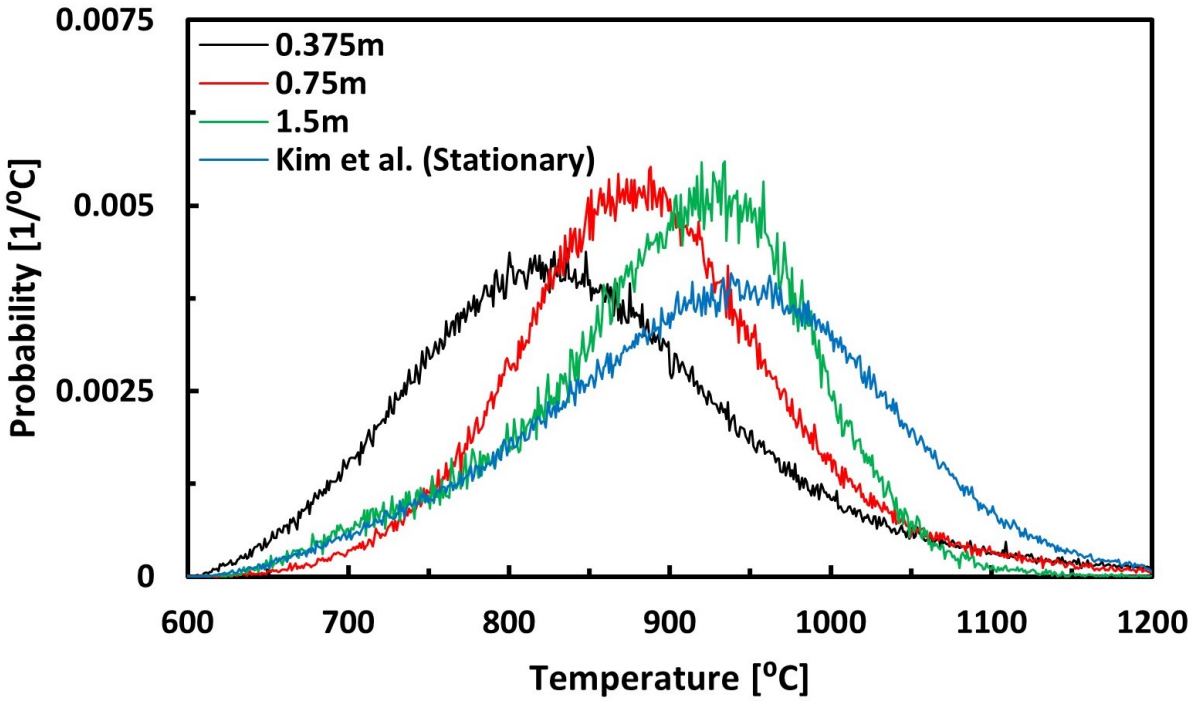

Figure 5.5: Single Image Histograms of a Stationary Ember compared to Streak Images at Varying Distances

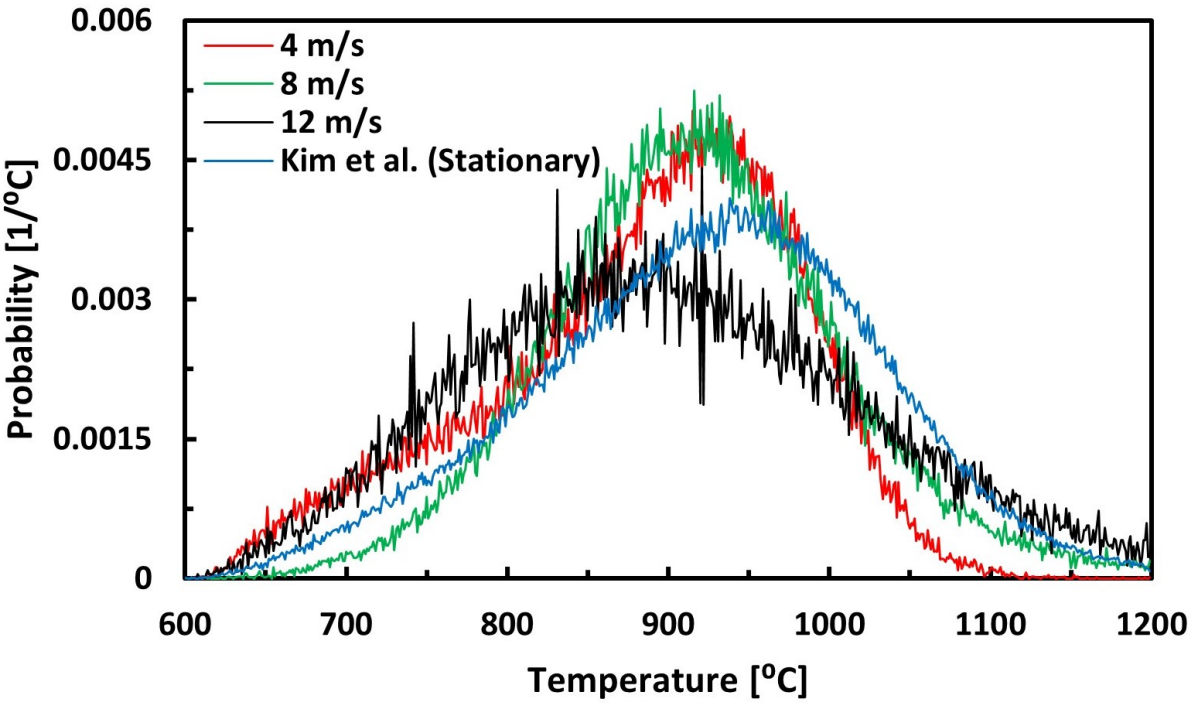

Figure 5.6: Single Image Histograms of a Stationary Ember compared to Streak Images at Varying Simulated Speeds

Qualitatively, in contrast to the hypothesized results, the streak images appear to pro-

duce histograms with a lower or equal variance about the mean when compared to the stationary ember. This is particularly evident in all cases except for the 12 m/s simulated speed case in 5.6. It is expected that this is due to the "smoothing" caused by physical motion previously dsicussed, which creates a collection of pixel temperatures that effectively convey the ember's mean surface temperature with variance largely attributed to noise caused by the ratio pyrometry's relatively low SNR. In contrast to this, the wider variance seen in the stationary image is attributed to the more evident imaging of both ember cool and hot spots, from factors such as ash accumulation and uneven wind speed. Also of note is that, while the noise in the measurements (considered as the qualitative fluctuations in the histogram curves) appears to only slightly varying with distance, the faster simulated speeds appear to carry a significantly increased degree of this noise. This effect is attributed to the increased degree of physical "smoothing" in those cases, which introduces more uncertainty in the specific portion of the object being imaged in any single pixel and thereby creates data noise. Also of note is that, in the distance histogram, the 0.375m case shows a significantly lower mean surface temperature than the other cases with the particular images considered. Again, due to the previously discussed time-temperature plots as well as the works of [8] showing no dependence of pyrometry temperature measurements on distance, the difference seen in these particular images is attributed to ambient conditions that could impact the ember's smoldering reaction. While images from the point of first smoldering from other trials of similar orientation were considered to improve the display of these results, all other trials showed the same characteristics - again, due to the cursory nature of this analysis because of its goal to quantify general dependencies (which translates to only four images satisfying the criteria of 1 m/s applied wind, 4 m/s simulated speed, horizontal rotation, 0.375m distance, and the point of first smoldering being captured) as well as the lack of distance-temperature dependence seen in other results, this particular finding is attributed to chance.

Following this qualitative analysis, Kolmogorov-Smirnov and Mann-Whitney U-Tests were again conducted on each of these data sets. The results of these tests can be seen in

Tables 5.7 and 5.8 for the varying distance trials and Tables 5.9 and 5.10 for the varying simulated speed trials.

Table 5.7: Kolmogorov-Smirnov Test Results for Inter-Streak Trials with Varying Distance (Constant 4 m/s Simulated Speed and 1 m/s Wind Speed)

	Reference [22] (Stat.)	**0.375m**	**0.75m**	**1.5m**
Reference [22] (Stat.)	-	1	1	1
0.375m	-	-	1	1
0.75m	-	-	-	1
1.5m	-	-	-	-

Table 5.8: Mann-Whitney U-Test Results for Inter-Streak Trials with Varying Simulated Speed (Constant 4 m/s Simulated Speed and 1 m/s Wind Speed)

	Reference [22] (Stat.)	**0.375m**	**0.75m**	**1.5m**
Reference [22] (Stat.)	1	0.4963	0	0.0012
0.375m	-	-	0	0
0.75m	-	-	-	0.6699
1.5m	-	-	-	-

Table 5.9: Kolmogorov-Smirnov Test Results for Inter-Streak Trials with Varying Simulated Speed (Constant 1.5m Distance and 1 m/s Wind Speed)

	Reference [22] (Stat.)	**4 m/s**	**8 m/s**	**12 m/s**
Reference [22] (Stat.)	-	1	1	1
4 m/s	-	-	1	1
8 m/s	-	-	-	1
12 m/s	-	-	-	-

Table 5.10: Mann-Whitney U-Test Results for Inter-Streak Trials with Varying Simulated Speed (Constant 1.5m Distance and 1 m/s Wind Speed)

	Reference [22] (Stat.)	**4 m/s**	**8 m/s**	**12 m/s**
Reference [22] (Stat.)	-	0.2346	0	0.8667
4 m/s	-	-	0.0455	0.0958
8 m/s	-	-	-	0
12 m/s	-	-	-	-

While these PDF results are not necessarily hypothesized to agree, due to the time-temperature fluctuations which still introduce a significant degree of unpredictability despite these images being sourced from similar points in each ember's "lifespan", they still provide insight in the repeatable nature of results between trials of differing configurations. In particular, while the KS Test results are not significantly useful (being that their Boolean output simply proves that the distributions are not the same as expected), the MWU test results provide a valuable measure of the similarity between distributions even given their general differences. Of primary note are the similarities between the stationary ember and the trials with 4 m/s and 12 m/s speed as well as the slight degree of similarity between the 4 m/s trial and the other two simulated movement orientations in 5.10 - while these values do not show perfect agreement, the fact that they demonstrate even this degree of similarity considering the temporal differences between the trials proves the generally repeatable behavior of the presented results.

6 Conclusions & Future Work

The individual impact of movement speed on a color pyrometry analysis applied to smoldering wood embers, intended to model firebrand particles relevant to the propagation of wildland fire events, was considered. The goal of this objective is to quantify the effect of a complicating factor in realistic firebrand movement on the presented pyrometry model, and thereby pave the way for future pyrometry analysis of realistic firebrands which could then be used to develop more accurate wildland fire spread models. The specific pyrometry method considered is based on a calibration against a blackbody furnace and uses the ratio of normalized green-to-red pixel intensities in a photograph to estimate temperature while removing the dependency on ember emissivity and ash transmittance, which infrared cameras and intensity-based pyrometry are dependent upon. The individual impact of firebrand movement speed was assessed by developing an apparatus that simulates ember movement by rotating the imaging device relative to a stationary ember, thereby better maintaining ember repeatability between trials. The simulated speed of the ember is adjusted by varying the imaging device rotation speed and the distance between the ember and the device's focus. The use of this apparatus was validated by considering the pixel intensity characteristics of an imaged LED device, as well as by imaging 5 embers at identical distance, rotation speed, and wind speed orientations. Through this the repeatability of the apparatus in a set orientation is verified, which thereby allows for a cursory analysis of a range of these factors with a minimal number of tests and reasonable confidence in the results.

Resulting from a consideration of the average ember surface temperature taken both spatially (within all the temperature data from a single image) and temporally (across all of the images taken for a single ember), the speed of the embers show little-to-no effect on their surface temperature estimations once decoupled from wind speed. Despite this agreement in average surface temperatures, a time-temperature relationship across each unique ember's lifespan is noted which introduces uncertainty the temporal comparison of different embers. The assertion that movement speed does not effect pyrometry temperature estimations in

this context is further validated through simple statistical analysis, involving an Analysis of Variance (ANOVA) of the average values and non-parametric distribution tests of single image's surface temperature histograms. Through this, it is further proved that the developed apparatus is not only capable of creating repeatable results at a single simulated speed orientation but also that the pyrometry-predicted average surface temperature is acceptably independent of simulated speed, even given the temporal uncertainty of each ember's surface temperature. The average ember surface temperatures were found to be 922.1 ± 20.4 °C with a 1 m/s applied wind speed and 955.0 ± 20.2 °C with a 2 m/s applied wind speed, which is in agreeement with the findings of references [22, 8].

In terms of future work into this topic, the time-temperature dependency and histograms of ember surface temperatures should be further explored to better define a firebrand's general characteristics for use in modeling. While these factors were only given a cursory overview in this body of work to contextualize the average surface temperature results, which are considered to be of primary concern in terms of the major results of ember images as well as for future heat transfer modeling, a more focused consideration could provide for a better understanding of ember mechanics in general. The more focused analysis of these factors could include considering a variety of wind conditions or different wood species for the time-temperature dependence, and concatenating histogram results for multiple images of shared orientation and thus deriving a more general distribution for embers subjected to those targeted conditions. Beyond these topics, immediate future work on the topic of ember pyrometry should focus on considering the effect of visual obscuration, such as would be expected in a realistic scenario with the smoke generated by wildland fire events, as well as considering a methodology for applying the discussed pyrometry methodology to situations with ambient light levels such as was noted an obstacle by reference [8]. In addition to this, other species of wood and varying moisture contents should be considered to more accurately reflect natural surface temperature conditions. In terms of the experimental apparatus, while the wind speed generation approach in this body of work is deemed to be effective as

a result of the anemometer investigations, a more rigorous approach should be considered due to the strong dependence of wind speed on surface temperature as noted in reference [48]. Additionally, pyrometry methods using the same blackbody furnace calibration method but different mathematical structures could be considered to improve the precision of the accurate ratio pyrometry approach without referencing it to the grayscale pyrometry results, such as by raising the green pixel intensities to a power or multiplying it by an additional factor to make its signal stronger relative to the predominantly red pixel intensities produced by imaging smoldering embers. While this could serve to fundamentally improve the ratio pyrometry method, care must be taken to ensure that ember surface emissivity and ash transmissivity still cancel out in a Planck's Law derivation, as this functionality is one of the primary benefits of ratio pyrometry. Finally, procedural improvements to the analysis method such as more complex smoothing, noise reduction, and edge finding mechanisms could be instituted to improve consistency between trial results.

Appendix A MATLAB Pyrometry Analysis Code

```
function[] = Pyrometry(IgnitionOffset,GHSToggle,XLSToggle)
% XLSToggle controls whether an excel sheet is prpduced, GSHToggle controls
% whether Grayscale Pyrometry is used.
format short g
myFolder = 'C:\Users\baldw\OneDrive\Desktop\Pyrometry\Demosaicing';
if (GSHToggle > 1)
    error(['Accepted GSHToggle Inputs are 0 (off) and 1 (on)'])
end
if (XLSToggle > 1)
    error(['Accepted XLSToggle Inputs are 0 (off) and 1 (on)'])
end
filePattern = fullfile(myFolder, '*.tiff'); % Change to whatever pattern you need.
theFiles = dir(filePattern);
% Get a list of all files in the folder with the desired file name pattern.
IgnitionOffset = 32.81; % Time between ignition
% (when lighter first touches ember) and start of photos.
tic; % Starts code timer, for considering operation efficiency


hold on
for k = 1: length(theFiles)


    photoname = theFiles(k).name;
    fullFileName = fullfile(theFiles(k).folder, photoname);
    RowHeader(k,1) = {photoname};


    A = imread(fullFileName);
```

```
rdc = 7.7; % This, and the next 2 terms, are dark current values.
gdc = 11.5; % They're representative for a single camera orientation,
bdc = 4.4; % but they're negligible in general.
GSdc = (rdc+gdc+bdc)/3;
res = size(A(:,:,1));
photoinfo = imfinfo(fullFileName);
iso = photoinfo.DigitalCamera.ISOSpeedRatings; % Image  ISO
t = photoinfo.DigitalCamera.ExposureTime; % Image Exposure Time [s]
f = photoinfo.DigitalCamera.FNumber; % Image F-Stop (~Zoom)
c1 = 0; % c1 and c2 provide manual cropping regions
c2 = 3000;
if (res(1) > 4000) % This if statement is suited to analyzing streak
    % photos, and auto-detects whether the image is vertical or horizontal
    y1 = 0; % Entire picture is 5496 by 3672 pixels.
    y2 = res(1);
    x1 = c1;
    x2 = c2;
else
    y1 = c1;
    y2 = c2;
    x1 = 0;
    x2 = res(2);
end
nrows = y2- y1;
ncolumns = x2- x1;
sat = size(A(A(:,:,1) == 65535));
SatPix(k) = sat(1);
```

```
X = [num2str(sat(1)), ' saturated pixels']; % Saturated pixel count
disp(X);
B = imcrop(A, [x1 y1 x2-x1 y2-y1]);

%% Separating RGB columns
rawred = double(B(:,:,1));
rawred(rawred > 65534) = 0; % This, and similar commands below, remove
% saturated pixels on the raw pixel intensity channels

rawgreen = double(B(:,:,2));
rawgreen(rawgreen > 65534 | rawgreen < 100) = 0; % Applies a
% rudimentary noise filter by removing raw green intensities beneath
% 100 (as per Dennis' Dissertation)

rawblue = double(B(:,:,3));
rawblue(rawblue > 65534) = 0;

rawGS = double(rgb2gray(B));
%% Normalized Intensities
normred = ((rawred-rdc)*(f^2))/(iso*t) % This, and below, normalize
% pixel intensities to the camera settings
normgreen = ((rawgreen-gdc)*(f^2))/(iso*t);
normblue = ((rawblue-bdc)*(f^2))/(iso*t);
if (GSHToggle == 1)
    normGS = ((rawGS-GSdc)*(f^2))/(iso*t);
end
%% Finding log of pixel G/R ratio to use for ratio pyrometry curve fit
```

```
GR = normgreen./normred; % Green-to-Red normalized pixel ratio
GR2 = log10(GR); % Log-base-10 of above ratio
GR2(imag(GR2) > 0) = 0; % Removes any imaginary entries
logGR = GR2; % Redefinition for calculations
%% Finding log of pixel Grayscale ratio
if (GSHToggle == 1)
    GS2 = log10(normGS); % Log 10 of normalized GS intensities
    GS2(imag(GS2) > 0) = 0;
    logGS = GS2;
end
%% Application of ratio pyrometry curve fit
RT = (362.73.*(logGR.^3) + 2186.7.*(logGR.^2) + 4466.5.*(logGR) ...
    + 3753.5); % New Camera Ratio Temp
%RT = (292.26.*(logGR.^3) + 1733.8.*(logGR.^2) + 3614.5.*(logGR)
% + 3253.2); % Old Camera Ratio Temp
%% Grayscale Pyrometry Fit
if (GSHToggle == 1)
    %GST = (13.126*(logGS.^2))+(15.692*logGS)+517.63;
    % Old Camera GS Temp, from Dennis' thesis, w/ ISO
    GST = (12.622.*(logGS.^2))+(18.54.*logGS)+514.93;
    %From Kyle's thesis, new camera GS temp w/ ISO
end
%% Removal of 600-1200 range (Ratio)
RT(RT < 600 | RT > 1200) = 0; % BB Calibration Temperature range
%% Removal of 600-1200 range (Grayscale)
if (GSHToggle == 1)
    GSTfull = GST;
```

```
    GSTfull(rawGS < 500 | GST < 600 | GST > 1200) = 0;
    GST(RT < 600 | RT > 1200 | GST < 600 | GST > 1200) = 0; % Removes
    % temperatures values outside of the calibration range for GS
    % temps, as well as Ratio Temps as a rudimentary edge-finding
    % mechanism
end
%% 50% rule (Ratio)
RT2 = RT; % This section and below apply a noise reduction algorithm
% - if 50% of pixels around each pixel are 0, set that pixel to 0 as well
for i = 4:(nrows-4)
    for j = 4:(ncolumns-4)
        if nnz(RT(i-3:i+3,j-3:j+3)) < 25
            RT2(i,j) = 0;
        else
            RT2(i,j) = RT(i,j);
        end
    end
end
%% 50% rule (Grayscale)
if (GSHToggle == 1)
    GST2 = GSTfull;
    for i = 4:(nrows-4)
        for j = 4:(ncolumns-4)
            if nnz(GST(i-3:i+3,j-3:j+3)) < 25
                GST2(i,j) = 0;
            else
                GST2(i,j) = GSTfull(i,j);
```

```
                end
            end
        end
    end
    %% MATLAB display
    RT3=RT2; % Left in b/c some images need to be flipped for proper
    % display - to do this, the command would instead be "RT3 = flip(RT2)
    RatioAverageTemp(k) = mean(nonzeros(RT3)); % Average surface temperature
    Pixel(k) = nnz(RT3); % Temp pixel count, to contextualize
    % the saturated pixel number
    if (GSHToggle == 1)
        GST3=GST2;
        GrayscaleAverageTemp(k) = mean(nonzeros(GST3));
    end
%% Exporting results to spreadsheets
% These all serve to print the analysis results to an Excel spreadsheet
if(XLSToggle == 1)
    if (GSHToggle == 0)
     xlswrite([photoinfo.FileModDate(1:11) '_HR' ...
         photoinfo.FileModDate(13:14) '_' 'Results.xlsx'],[SatPix' ...
         Pixel' RatioAverageTemp'],'Sheet1','B2')
     xlswrite([photoinfo.FileModDate(1:11) '_HR' ...
         photoinfo.FileModDate(13:14) '_' 'Results.xlsx'], ...
         {'Photo Name','Saturated Pixel Count','Pixel Count', ...
         'Avg Ratio Temp C'},'Sheet1','A1')
     xlswrite([photoinfo.FileModDate(1:11) '_HR' ...
         photoinfo.FileModDate(13:14) '_' 'Results. xlsx'], ...
```

```
        cellstr(RowHeader),'Sheet1','A2')
    else
     xlswrite([photoinfo.FileModDate(1:11) '_HR' ...
        photoinfo.FileModDate(13:14) '_' 'Results.xlsx'],[SatPix' ...
        Pixel' RatioAverageTemp' GrayscaleAverageTemp'],'Sheet1','B2')
     xlswrite([photoinfo.FileModDate(1:11) '_HR' ...
        photoinfo.FileModDate(13:14) '_' 'Results.xlsx'], ...
        {'Photo Name','Saturated Pixel Count','Pixel Count', ...
        'Avg Ratio Temp C','Avg Grayscale Temp C'},'Sheet1','A1')
     xlswrite([photoinfo.FileModDate(1:11) '_HR' ...
        photoinfo.FileModDate(13:14) '_' 'Results.xlsx'], ...
        cellstr(RowHeader),'Sheet1','A2')
    end
    xlswrite([photoinfo.FileModDate(1:11) '_HR' ...
        photoinfo.FileModDate(13:14) '_' 'Results.xlsx'], ...
        IgnitionOffset,'Sheet1','N3');
    xlswrite([photoinfo.FileModDate(1:11) '_HR' ...
        photoinfo.FileModDate(13:14) '_' 'Results.xlsx'], ...
        {'Time from Ignition to Start of Photos (s)'},'Sheet1','N2');
end
    toc; % Ends code timer
    hold off
end
```

Appendix B MATLAB dcraw Image Conversion Code

```
%% Automatically converts RAW format images to TIFF format images using the
%dcraw software, given the input of the directory path where the photos are
%located. In order for this program to work, the dcraw software will need
%to be downloaded. At the time of writing, it can
%be found at https://www.dechifro.org/dcraw/.


clear all
folderfilepath = 'C:\Users\baldwinj\Desktop\PhotoAnalysisFolder\';
filePattern = fullfile(folderfilepath, '*.arw'); % Change to whatever
%pattern you need.
Files = dir(filePattern);
%% Conversion Process
for photo = 1:length(Files)
 command = ['dcraw -v -4 -T ' folderfilepath Files(photo).name];
 system(command);
end
```

Appendix C MATLAB Trial ANOVA Analysis Code

```
%% Average Streak Temperatures and Corresponding Conditions
AvgTemp1ms = [932.357745 910.2257531 924.2500941 948 928 885.0705104 ...
    898.7330831 903.3814622 880.0365881 930.0780336 926.9611714 ...
    923.2674662 931.7628147 950.3652012 937.8443097 942.5356665 922.675459];
% Average Surface Temperatures across images for 1 m/s wind [C]
SimSpeed1ms = [0 0 0 0 0 2 2 2 4 4 4 4 8 8 8 12 12]; % Simulated ember
% speeds for each 1 m/s trial
WindSpeed1ms = zeros(1,length(AvgTemp1ms)); % Wind speed for each 1 m/s wind trial
WindSpeed1ms(:) = 1;
Dist1ms = [1.5 0.75 0.375 1 0.01 0.375 0.75 0.375 0.375 ...
    0.75 1.5 0.75 0.75 1.5 1.5 1.5 1.5]; % Distance for each 1 m/s trial
Orient1ms = {'Horz' 'Horz' 'Horz' 'Horz' 'Horz' 'Horz' 'Horz' ...
    'Vert' 'Horz' 'Horz' 'Horz' 'Vert' 'Horz' 'Horz' 'Vert' 'Horz' 'Vert'};
% Mounting Orientation for each 1 m/s trial
AvgTemp2ms = [985.1172374 949.6905589 951.2514735 948 928 945.6292744 ...
    954.672665 931.7834112 936.1973085 982.0157659 973.5901701 ...
    941.2472594 980.5987481 961.9546588 930.2717063 988.8468492 945.0896974];
% This, and below, are the same aforementioned factors except for the 2 m/s
% wind speed trials
SimSpeed2ms = [0 0 0 0 0 2 2 2 4 4 4 4 8 8 8 12 12];
WindSpeed2ms = zeros(1,length(AvgTemp2ms));
WindSpeed2ms(:) = 2;
Dist2ms = [1.5 0.75 0.375 1 0.01 0.375 0.75 0.375 0.375 0.75 1.5 ...
    0.75 0.75 1.5 1.5 1.5 1.5];
Orient2ms = {'Horz' 'Horz' 'Horz' 'Horz' 'Horz' 'Horz' 'Horz' 'Vert' ...
    'Horz' 'Horz' 'Horz' 'Vert' 'Horz' 'Horz' 'Vert' 'Horz' 'Vert'};
```

```
%% Concatenating Matrices
AvgTemp = [AvgTemp1ms AvgTemp2ms];
SimSpeed = [SimSpeed1ms SimSpeed2ms];
WindSpeed = [WindSpeed1ms WindSpeed2ms];
Dist = [Dist1ms Dist2ms];
Orient = [Orient1ms Orient2ms];
%% ANOVA Analysis
[~,~,stats] = anovan(AvgTemp,{SimSpeed,WindSpeed,Dist,Orient}) % N-Way
% ANOVA analysis between all factors considered
BH = multcompare(stats,'CType','bonferroni') % Bonferroni Correction for
% the n-way ANOVA, which considers the individual relationship between factors
Temp_WindSpeed = anova1(AvgTemp,WindSpeed) % This, and below, effectively
% conduct a Student's T-Test through a 1-way ANOVA and thereby provide a
% similar validation of results as the Bonferroni correction
Temp_SimSpeed = anova1(AvgTemp,SimSpeed)
Temp_Dist = anova1(AvgTemp,Dist)
Temp_Orient = anova1(AvgTemp,Orient)
```

Appendix D MATLAB Repeatability ANOVA Analysis Code

```
%% Repeatability Trials - average surface temperature for each photo as a
%% function of test number.
AvgTemp1 = [877.04 868.66 860.33 838.49 876.14 875.28 865.38 863.11 ...
    866.6 861.15 843.12 849.32 867.90 873.69 917.8 881.4 880.05]; % This,
% and below, are the average surface temperature of each image captured
% in the repeatability trial. Suffix number corresponds to the specific trial
AvgTemp2 = [859.54 860.55 863.05 848.42 891.13 898.70 885.91 868.65 ...
    876.76 915.10 925.22 899.30 879.73 919.81 908.39 914.17 902.26 ...
    901.13 894.50 889.17 886.10 946.09];
AvgTemp3 = [897.17 847.24 874.76 884.64 900.62 873.54 855.93 880.82 ...
    887.54 864.57];
AvgTemp4 = [857.82 901.26 862.09 862.30 851.95 879.45 884.34 874.11 ...
    890.73 848.44 898.57 855.32 849.48 883.07 859.69 864.36 903.93];
AvgTemp5 = [888.37 899.24 848.13 828.33 864.76 876.78 892.94 897.84 ...
    865.07 843.20 870.01 882.57 859.40 898.76 882.67 877.88 883.23 ...
    893.14 921.58];
TrialNum1 = ones(1,length(AvgTemp1)); % Sets the trial number, for the
% ANOVA analysis
TrialNum2 = 2*ones(1,length(AvgTemp2));
TrialNum3 = 3*ones(1,length(AvgTemp3));
TrialNum4 = 4*ones(1,length(AvgTemp4));
TrialNum5 = 5*ones(1,length(AvgTemp5));
%% Concatenating Matrices
AvgTemp = [AvgTemp1 AvgTemp2 AvgTemp3 AvgTemp4 AvgTemp5];
TrialNum = [TrialNum1 TrialNum2 TrialNum3 TrialNum4 TrialNum5];
```

```
AvgTempwo2 = [AvgTemp1 AvgTemp3 AvgTemp4 AvgTemp5];
TrialNumwo2 = [TrialNum1 TrialNum3 TrialNum4 TrialNum5];
%% ANOVA Analysis
Result = anova1(AvgTemp,TrialNum) % 1-way ANOVA between average surface
% temperatures and trial number - if proven independent, temperatures
% independent of experiment and results are verified as repeatible
Resultwo2 = anova1(AvgTempwo2,TrialNumwo2)
```

Appendix E MATLAB Probability Distribution Test Code

```
clear all
dbclear if error;
format short g
myFolder = ['C:\Users\baldw\OneDrive\Desktop\Pyrometry\' ...
    'InterStreakAnalysis_Distance']; % Get a list of all files in
% the folder with the desired file name pattern.
filePattern = fullfile(myFolder, '*.tiff'); % Change to whatever pattern you need.
theFiles = dir(filePattern);
SmoothingToggle = 0; % Set to 1 to use a 7-by-7 window mean
% smoothing algorithm on the non-zero entries, 0 for no smoothing
tic;

for k = 1: length(theFiles)

    photoname = theFiles(k).name
    fullFileName = fullfile(theFiles(k).folder, photoname);
    A = imread(fullFileName);
    res = size(A(:,:,1));
    photoinfo = imfinfo(fullFileName);
    iso = photoinfo.DigitalCamera.ISOSpeedRatings; %isovalue
    t = photoinfo.DigitalCamera.ExposureTime; %seconds
    f = photoinfo.DigitalCamera.FNumber; %f-stop

    y1(1:length(theFiles)) = 0;
    y2(1:length(theFiles)) = res(1);
```

```
x1(1:length(theFiles)) = 0;
x2(1:length(theFiles)) = res(2);
nrows = y2(k)- y1(k);
ncolumns = x2(k) - x1(k);
sat = size(A(A(:,:,1) == 65535));
SatPix(k) = sat(1);
X = [num2str(sat(1)), ' saturated pixels'];
disp(X)
B = imcrop(A, [x1(k) y1(k) x2(k)-x1(k) y2(k)-y1(k)]);

rdc = 7.7; % Dark Current Values
gdc = 11.5;
bdc = 4.4;

rawred = double(B(:,:,1));
rawred(rawred > 65534) = 0; % Removes saturated red pixels

rawgreen = double(B(:,:,2));
rawgreen(rawgreen > 65534 | rawgreen < 100) = 0;
% Removes saturated green pixels as well as those with an intensity
% under 100, which are noted to produce noise (Kim Dissertation).

normred = ((rawred-rdc)*(f^2))/(iso*t); % Pixel Intensity Normalization
normgreen = ((rawgreen-gdc)*(f^2))/(iso*t);

GR = normgreen./normred;
GR2 = log10(GR);
```

```
    GR2(imag(GR2) > 0) = 0; % Removes ratio values from null pixels
    logGR = GR2;

    RT = (362.73.*(logGR.^3) + 2186.7.*(logGR.^2) + 4466.5.*(logGR) + ...
        3753.5); % New Camera Ratio Temp Correlation
    RT(RT < 600 | RT > 1200) = 0;
    %removes temperatures outside of calibration range

    RT2 = RT;
    for i = 4:(nrows-4) % 50% Rule: A form of noise reduction,
        % if the majority of pixels in a 7x7 area around a pixel are
        % empty, set it equal to 0.
        for j = 4:(ncolumns-4)
            if nnz(RT(i-3:i+3,j-3:j+3)) < 25
                RT2(i,j) = 0;
            else
                RT2(i,j) = RT(i,j);
            end
        end
    end

%% Ratio Smoothing (For Streaks)
if (SmoothingToggle == 1) % 7x7 moving window mean filter algorithm.
    % The if statements account for the window's border conditions.
    RT3 = RT2;
    for i = 1:nrows
        for j = 1:ncolumns
```

```
            if RT2(i,j) > 0 && 3 <= i && i <= (nrows-3) && 3 <= j && j <= (ncolumns-3)
               RT3(i,j) =  mean(nonzeros(RT2(i-2:i+2,j-2:j+2)));
            elseif RT2(i,j) > 0 && i < 3 && 3 <= j && j <= (ncolumns-3)
                RT3(i,j) =  mean(nonzeros(RT2(i:i+2,j-2:j+2)));
            elseif RT2(i,j) > 0 && i > (nrows-3) && 3 <= j && j <= (ncolumns-3)
                RT3(i,j) =  mean(nonzeros(RT2(i-2:i,j-2:j+2)));
            elseif RT2(i,j) > 0 && 3 <= i && i <= (nrows-3) && j < 3
                RT3(i,j) =  mean(nonzeros(RT2(i-2:i+2,j:j+2)));
            elseif RT2(i,j) > 0 && 3 <= i && i <= (nrows-3) && j > (ncolumns-3)
                RT3(i,j) =  mean(nonzeros(RT2(i-2:i+2,j-2:j)));
            end
        end
    end
else
    RT3=RT2;
end
%% Avg. Temp and Pixel Count
    RatioAverageTemp(k) = mean(nonzeros(RT3));
    Pixel(k) = nnz(RT3);
%% PDF Distribution Analysis
    n = 600:0.5:1200;

    figure(1)
    hold on
    h(k) = histogram(RT3(RT3>0),600,'Normalization','probability');
    % Plots histogram
    hold off
```

```
    pd(k) = fitdist(RT3(RT3>0),'Normal'); % Fits & plots a
    % Gaussian distribution from the dataset, which are evidently
    % normally distributed in the histogram.
    PDF(k,:) = pdf(pd(k),n);

    figure(2)
    hold on
    plot(n,PDF(k,:));
    hold off
end

for x = 1:length(theFiles)
    for z = 1:length(theFiles)
        KS2(x,z) = kstest2(PDF(x,:),PDF(z,:));
        MWU(x,z) = ranksum(PDF(x,:),PDF(z,:));
    end
end

%disp('For the 2-way KS Test, a result of 1 means that the ...
% distributions are not equal, 0 means that they are.')
%disp('The ranksum command executes a Wilcoxon Rank-Sum Test ...
% /Mann-Whitney U-Test (same thing), which displays a confidence ...
% value with respect to the difference - e.g. a result of 0.03 means ...
% that the means are different to the 3% confidence level, so with ...
% 97% confidence.')
```

```
for y = 1:length(theFiles)
    LegEntry{y} = ['RT' num2str(y)];
end

figure(2)
legend(LegEntry)

for p = 1:length(theFiles)
    %xlswrite('HistogramDataSet.xlsx',h(p).Values,'Sheet1',['A' num2str(p)]);
end

%xlswrite('PDFDataSets.xlsx',PDF);

toc;
```

Appendix F MATLAB Contour Plot Generation Code

```
  function[] = ContourPlots(PlotCase,GSHToggle,SmoothingToggle)
if (GSHToggle > 1)
    error(['Accepted GSHToggle Inputs are 0 (off) and 1 (on)'])
end
if (SmoothingToggle > 1)
    error(['Accepted SmoothingToggle Inputs are 0 (off) and 1 (on)'])
end
format short g
myFolder = 'C:\Users\baldw\OneDrive\Desktop\Pyrometry\VertStreakImages';
% Get a list of all files in the folder with the desired file name pattern.
filePattern = fullfile(myFolder, '*.tiff');
% Change to whatever pattern you need.
theFiles = dir(filePattern);
mmPC(1) = 1/12.1; % Pixel-to-mm conversion for 0.375m focal distance
% (i.e. 121 pixels is 1cm in the straight-on orientation, which is the
% best approximation that we'll likely get)
mmPC(2) = 1/5.7; % Pixel-to-mm conversion for 0.75m focal distance
mmPC(3) = 1/2.7; % Pixel-to-mm conversion for 1.5m focal distance
tic; % Starts a timer for the code, to consider operation efficiency


hold on
for k = 1: length(theFiles)


    photoname = theFiles(k).name;
    fullFileName = fullfile(theFiles(k).folder, photoname);
    RowHeader(k) = {photoname};
```

```
    A = imread(fullFileName);
    L = imlocalbrighten(A); % Artifically brightens the image, for
    % presentation purposes. DON'T USE FOR ACTUAL ANALYSIS.
    rdc = 7.7; % This, and the next 2 terms, are dark current values.
    gdc = 11.5; % They're representative for a single camera orientation,
    bdc = 4.4; % but they're negligible in general.
    GSdc = (rdc+gdc+bdc)/3;
    res = size(A(:,:,1));
    photoinfo = imfinfo(fullFileName);
    iso = photoinfo.DigitalCamera.ISOSpeedRatings; % isovalue
    t = photoinfo.DigitalCamera.ExposureTime; % exposure time in seconds
    f = photoinfo.DigitalCamera.FNumber; % f-stop
switch PlotCase % This structure switches between different photo
    % orientations, with the specific case needing to be set manually
    % depending on your needs. The values correspond to the cropping
    % region of the specific photos I considered, so will vary on a
    % case-by-case basis.
    case 'HorzStreakFull'
        x1(1) = 0;
        x2(1) = 5445;
        y1(1) = 2037;
        y2(1) = 2400;
    case 'VertStreaks'
        x1(1) = 2233;
        x2(1) = 2717;
        x1(2) = 2096;
```

```
        x2(2) = 2324;
        x1(3) = 1971;
        x2(3) = 2079;
        y1(1) = 2500;
        y2(1) = 2863;
        y1(2) = 2500;
        y2(2) = 2842;
        y1(3) = 2500;
        y2(3) = 2824;
    case 'HorzStreaks'
        y1(1) = 2069;
        y2(1) = 2311;
        y1(2) = 1873;
        y2(2) = 1987;
        y1(3) = 1788;
        y2(3) = 1842;
        x1(1) = 2000;
        x2(1) = 2363;
        x1(2) = 2000;
        x2(2) = 2342;
        x1(3) = 2800;
        x2(3) = 3124;
    case'LEDStreak'
        x1(1) = 0;
        x2(1) = 5445;
        y1(1) = 1948;
        y2(1) = 2432;
```

```
    case'StatLED'
        x1(1) = 2915;
        x2(1) = 3036;
        y1(1) = 2049;
        y2(1) = 2200;
    case'StatEmber'
        x1(1) = 2394;
        x2(1) = 2757;
        y1(1) = 2000;
        y2(1) = 2121;
    otherwise
        % Produces an error if the inputted case isn't recognized
        error(['Unexpected PlotCase function input. Accepted entries ' ...
            'are "StatEmber", "HorzStreakFull", "HorzStreaks", ' ...
            '"VertStreaks", "LEDStreak", and "StatLED".'])
end
nrows = y2(k)- y1(k);
ncolumns = x2(k) - x1(k);

sat = size(A(A(:,:,1) == 65535)); % Determines the number of saturated pixels
    SatPix(k) = sat(1);
    X = [num2str(sat(1)), ' saturated pixels'];
    disp(X);
    B = imcrop(A, [x1(k) y1(k) x2(k)-x1(k) y2(k)-y1(k)]);

    %% Separating RGB columns
    rawred = double(B(:,:,1));
```

```
rawred(rawred > 65534) = 0; % Removes saturated red pixels


rawgreen = double(B(:,:,2));
rawgreen(rawgreen > 65534 | rawgreen < 100) = 0; % Removes saturated
% green pixels, and applies a noise filtering method


rawblue = double(B(:,:,3));
rawblue(rawblue > 65534) = 0;


rawGS = double(rgb2gray(B)); % Creates grayscale values from the image
%% Normalized Intensities
normred = ((rawred-rdc)*(f^2))/(iso*t); % These and below normalize
% the pixel values to the camera settings
normgreen = ((rawgreen-gdc)*(f^2))/(iso*t);
normblue = ((rawblue-bdc)*(f^2))/(iso*t);
 if (GSHToggle == 1)
    normGS = ((rawGS-GSdc)*(f^2))/(iso*t);
 end
  %% Finding log of pixel G/R ratio to use for ratio pyrometry curve fit
GR = normgreen./normred; % Green-to-Red ratio of normalized pixel intensities
GR2 = log10(GR); % Log base 10 of the above ratio
GR2(imag(GR2) > 0) = 0; % Removes any imaginary entries
logGR = GR2; % Redefinition for calculations
%% Finding log of pixel Grayscale ratio
if (GSHToggle == 1)
    GS2 = log10(normGS); % Log 10 of normalized GS intensities
    GS2(imag(GS2) > 0) = 0;
```

```
    logGS = GS2;
end
%% Application of ratio pyrometry curve fit
RT = (362.73.*(logGR.^3) + 2186.7.*(logGR.^2) + 4466.5.*(logGR) + ...
    3753.5); % New Camera Ratio Temp
%RT = (292.26.*(logGR.^3) + 1733.8.*(logGR.^2) + 3614.5.*(logGR) + ...
% 3253.2); % Old Camera Ratio Temp
%% Grayscale Pyrometry Fit
if (GSHToggle == 1)
    %GST = (13.126*(logGS.^2))+(15.692*logGS)+517.63;
    % Old Camera GS Temp, from Dennis' thesis, w/ ISO
    GST = (12.622.*(logGS.^2))+(18.54.*logGS)+514.93;
    %From Kyle's thesis, new camera GS temp w/ ISO
end
%% Removal of 600-1200 range (Ratio)
RT(RT < 600 | RT > 1200) = 0; % BB Calibration Temperature range
%% Removal of 600-1200 range (Grayscale)
if (GSHToggle == 1)
    GSTfull = GST;
    GSTfull(rawGS < 500 | GST < 600 | GST > 1200) = 0; % Applies a
    % filter to the GS values to reduce noise, and applies
    % BB temperature range
    GST(RT < 600 | RT > 1200 | GST < 600 | GST > 1200) = 0;
end
%% 50% rule (Ratio)
RT2 = RT; % This section and below apply a noise reduction algorithm
% - if 50% of pixels around each pixel are 0, set that pixel to 0 as well
```

```
    for i = 4:(nrows-4)
        for j = 4:(ncolumns-4)
            if nnz(RT(i-3:i+3,j-3:j+3)) < 25
                RT2(i,j) = 0;
            else
                RT2(i,j) = RT(i,j);
            end
        end
    end
    %% 50% rule (Grayscale)
    if (GSHToggle == 1)
        GST2 = GSTfull;
        for i = 4:(nrows-4)
            for j = 4:(ncolumns-4)
                if nnz(GST(i-3:i+3,j-3:j+3)) < 25
                    GST2(i,j) = 0;
                else
                    GST2(i,j) = GSTfull(i,j);
                end
            end
        end
    end
        %% Ratio Smoothing (For Streaks)
 RT3 = RT2; % Optional 7x7 mean smoothing algorithm
  if (SmoothingToggle == 1)
    for i = 1:nrows
        for j = 1:ncolumns
```

```
            if RT2(i,j) > 0 && 3 <= i && i <= (nrows-3) && 3 <= j && j <= (ncolumns-3)
               RT3(i,j) =  mean(nonzeros(RT2(i-2:i+2,j-2:j+2)));
            elseif RT2(i,j) > 0 && i < 3 && 3 <= j && j <= (ncolumns-3)
                RT3(i,j) =  mean(nonzeros(RT2(i:i+2,j-2:j+2)));
            elseif RT2(i,j) > 0 && i > (nrows-3) && 3 <= j && j <= (ncolumns-3)
                RT3(i,j) =  mean(nonzeros(RT2(i-2:i,j-2:j+2)));
            elseif RT2(i,j) > 0 && 3 <= i && i <= (nrows-3) && j < 3
                RT3(i,j) =  mean(nonzeros(RT2(i-2:i+2,j:j+2)));
            elseif RT2(i,j) > 0 && 3 <= i && i <= (nrows-3) && j > (ncolumns-3)
                RT3(i,j) =  mean(nonzeros(RT2(i-2:i+2,j-2:j)));
            end
        end
    end
  end
switch PlotCase
  %% Horizontal Rotation Figure Printout (Full)
  % These case commands all produce the contour plots associated with each
  % case, with specific orientations on a case-by-case basis. Because of
  % their similar structures, only the first case is fully commented.
  % All position values come from manual tweaking due to the signfiicant
  % size variations between cases.
    case 'HorzStreakFull'
        f = figure(1);
        f.Position = [0 0 1920 1080]; % Fits figure window to a 1080p
        % computer monitor (i.e. full screens the figure)
        pos1 = [0.05 0.1 0.35 0.15]; % Contour plot position in figure
        pos2 = [0.05 0.265 0.35 0.088]; % Image position in figure
```

```
subplot('Position',pos1)
P = imagesc(RT2,[600 1200]); % Color image of the ratio
% temperatures (NOTE: need to use imagesc because it doesn't
% produce borders between cells)
daspect([1 1 1]); % Image aspect ratio -
% this specific command keeps it as the source aspect ratio
shading interp % Color plot shading interpolation/smoothing
colormap jet % Specific color scheme - can change, just stylistic
c = colorbar('southoutside'); % Colorbar scale location
ax1 = gca; % Axis data, set here for manipulation
% Neccesary b/c color plots and images have intrinsically different
% formats in MATLAB and we want them to be the same for
% presentation purposes.
set(ax1,'YDir','normal'); % y-axis direction
ax1.YAxis.Limits = [0 (y2(k)-y1(k))]; % Y-Axis limits
ax1.XAxis.Limits = [0 (x2(k)-x1(k))]; % X-Axis limits
ax1.YTick = [0 (0.5*(y2(k)-y1(k))) y2(k)-y1(k)]; % Y-Axis Tick values
set(ax1, 'YTickLabel', round(mmPC(k)*get(ax1, 'YTick'),2)); % Y-Axis
% tick labels
ax1.XTick = [0 0.5*(x2(k)-x1(k)) x2(k)-x1(k)]; % X-Axis Tick values
set(ax1, 'XTickLabel', round(mmPC(k)*get(ax1, 'XTick'),2),'fontsize',11);
% X-Axis tick labels
ylabel('Length [mm]','fontsize',11); % Y-Axis title
xlabel([char(176) 'C (Colorbar), Length [mm] (Plot)'],'fontsize',11);
% X-Axis title
subplot('Position',pos2)
image(L) % Displays brightened image
```

```
    daspect([1 1 1]);
    xlim([x1(k) x2(k)]) % This and below force the desired axis limits
    ylim([y1(k) y2(k)])
    ax2 = gca;
    ax2.YTick = [y1(k) (y1(k)+0.5*(y2(k)-y1(k))) y2(k)];
    set(ax2, 'YTickLabel', round(mmPC(k)*(get(ax2, 'YTick') - ...
        y1(k)),2));
    set(ax2,'YDir','normal');
    ax2.XTick = [x1(k) (x1(k)+0.5*(x2(k)-x1(k))) x2(k)];
    set(ax2, 'XTickLabel', round(mmPC(k)*(get(ax2, 'XTick') - ...
        x1(k)),2),'fontsize',11);
    ylabel('Length [mm]','fontsize',11);
    if(k==1) % This k value corresponds to the last number of photos
        % considered (i.e. if 3 photos, k=3)
        print([photoname '_FullStreak.jpg'],'-djpeg')
    end
%% Horizontal Rotation Figure Printout (Cropped)
case 'HorzStreaks'
    f = figure(1);
    f.Position = [0 0 1920 1080];
    pos1 = [0.1 (0.15 + (0.13*(k-1))) 0.15 0.075];
    if (k==3)
        pos2 = [0.28 (0.15 + (0.13*(k-1))) 0.15 0.14];
    else
        pos2 = [0.28 (0.15 + (0.13*(k-1))) 0.15 0.075];
    end
    subplot('Position',pos2)
```

```
P = imagesc(RT3,[600 1200]);
daspect([1 1 1]);
shading interp
colormap jet
if(k==3)
    c = colorbar('northoutside');
    ylabel(c,[char(176) 'C'],'fontsize',12);
end
ax1 = gca;
set(ax1,'YDir','normal');
ax1.YAxis.Limits = [0 (y2(k)-y1(k))];
ax1.XAxis.Limits = [0 (x2(k)-x1(k))];
ax1.YTick = [0 (0.5*(y2(k)-y1(k))) y2(k)-y1(k)];
set(ax1, 'YTickLabel', round(mmPC(k)*get(ax1, 'YTick'),2));
ax1.XTick = [0 0.5*(x2(k)-x1(k)) x2(k)-x1(k)];
set(ax1, 'XTickLabel', round(mmPC(k)*get(ax1, 'XTick'),2),'fontsize',11);
if (k==1)
    xlabel('Length [mm]','fontsize',11)
end
yyaxis right;
if(k==1)
    ylabel('0.375m','fontsize',20,'Color','black')
elseif(k==2)
    ylabel('0.75m','fontsize',20,'Color','black')
elseif(k==3)
    ylabel('1.5m','fontsize',20,'Color','black')
end;
```

```
        ax1r = gca;
        set(ax1r, 'YTickLabel',[]);
        title('Ratio Analysis');
        xlabel({'X-Direction Pixels';['Ratio Average Temperature = ' ...
            num2str(RatioAverageTemp(k))]});
        ylabel('Y-Direction Pixels')
        subplot('Position',pos1)
        image(L)
        daspect([1 1 1]);
        xlim([x1(k) x2(k)])
        ylim([y1(k) y2(k)])
        ax2 = gca;
        ax2.YTick = [y1(k) (y1(k)+0.5*(y2(k)-y1(k))) y2(k)];
        set(ax2, 'YTickLabel', round(mmPC(k)*(get(ax2, 'YTick') - ...
            y1(k)),2));
        set(ax2,'YDir','normal');
        ax2.XTick = [x1(k) (x1(k)+0.5*(x2(k)-x1(k))) x2(k)];
        set(ax2, 'XTickLabel', round(mmPC(k)*(get(ax2, 'XTick') - ...
            x1(k)),2),'fontsize',11);
        if(k==1)
            xlabel('Length [mm]','fontsize',11)
        end
        ylabel('Length [mm]','fontsize',11)
        if(k==3)
            print([photoname '_HorzStreaks.jpg'],'-djpeg')
        end
%% Stationary Ember Figure Printout
```

```
case 'StatEmber'
    f = figure(1);
    f.Position = [0 0 1920 1080];
    pos1 = [0.295 0.3 0.21 0.3];
    pos2 = [0.1 0.3 0.175 0.3];
    subplot('Position',pos1)
    P = imagesc(RT3,[600 1200]);
    daspect([1 1 1]);
    shading interp
    colormap jet
    c = colorbar;
    title(c,[char(176) 'C'],'fontsize',11);
    ax1 = gca;
    set(ax1,'YDir','normal');
    ax1.YAxis.Limits = [0 (y2(k)-y1(k))];
    ax1.XAxis.Limits = [0 (x2(k)-x1(k))];
    ax1.YTick = [0 (0.5*(y2(k)-y1(k))) y2(k)-y1(k)];
    set(ax1, 'YTickLabel', round(mmPC(k)*get(ax1, 'YTick'),2));
    ax1.XTick = [0 0.5*(x2(k)-x1(k)) x2(k)-x1(k)];
    set(ax1, 'XTickLabel', round(mmPC(k)*get(ax1, 'XTick'),2),'fontsize',11);
    xlabel('Length [mm]','fontsize',11);
    subplot('Position',pos2)
    image(L)
    daspect([1 1 1]);
    xlim([x1(k) x2(k)])
    ylim([y1(k) y2(k)])
    ax2 = gca;
```

```
        ax2.YTick = [y1(k) (y1(k)+0.5*(y2(k)-y1(k))) y2(k)];
        set(ax2, 'YTickLabel', round(mmPC(k)*(get(ax2, 'YTick') - ...
            y1(k)),2));
        set(ax2,'YDir','normal');
        ax2.XTick = [x1(k) (x1(k)+0.5*(x2(k)-x1(k))) x2(k)];
        set(ax2, 'XTickLabel', round(mmPC(k)*(get(ax2, 'XTick') - ...
            x1(k)),2),'fontsize',11);
        ylabel('Length [mm]','fontsize',11);
        xlabel('Length [mm]','fontsize',11);
        print([photoname '_StatEmber.jpg'],'-djpeg')
%% Horizontal Rotation Green Intensities Figure Printout
    case 'LEDStreak'
        f = figure(1);
        f.Position = [0 0 1920 1080];
        pos1 = [0.05 (0.1 + (0.26*(k-1))) 0.7 0.115];
        pos2 = [0.05 (0.215 + (0.26*(k-1))) 0.7 0.3];
        subplot('Position',pos2)
        if(k==1)
            P = imagesc(normgreen,[0 1000]);
        elseif(k==2)
            P = imagesc(normblue,[0 150]);
        elseif(k==3)
            P = imagesc(normblue,[0 75]);
        end
        daspect([1 1 1]);
        shading interp
        colormap jet
```

```
c = colorbar('northoutside');
title(c,['Intensity'],'fontsize',12);
ax1 = gca;
set(ax1,'YDir','normal');
ax1.YAxis.Limits = [0 (y2(k)-y1(k))];
ax1.XAxis.Limits = [0 (x2(k)-x1(k))];
ax1.YTick = [0 (0.5*(y2(k)-y1(k))) y2(k)-y1(k)];
set(ax1, 'YTickLabel', round(mmPC(k)*get(ax1, 'YTick'),2));
ax1.XTick = [0 0.5*(x2(k)-x1(k)) x2(k)-x1(k)];
set(ax1, 'XTickLabel', round(mmPC(k)*get(ax1, 'XTick'),2),'fontsize',11);
ylabel('Length [mm]','fontsize',11);
subplot('Position',pos1)
image(L)
daspect([1 1 1]);
xlim([x1(k) x2(k)])
ylim([y1(k) y2(k)])
if(k==1)
    ylabel('0.375m','fontsize',20)
elseif(k==2)
    ylabel('0.75m','fontsize',20)
elseif(k==3)
    ylabel('1.5m','fontsize',20)
end
ax2 = gca;
ax2.YTick = [y1(k) (y1(k)+0.5*(y2(k)-y1(k))) y2(k)];
set(ax2, 'YTickLabel', round(mmPC(k)*(get(ax2, 'YTick') - ...
    y1(k)),2));
```

```
    set(ax2,'YDir','normal');
    ax2.XTick = [x1(k) (x1(k)+0.5*(x2(k)-x1(k))) x2(k)];
    set(ax2, 'XTickLabel', round(mmPC(k)*(get(ax2, 'XTick') - ...
        x1(k)),2),'fontsize',11);
    xlabel('Length [mm]','fontsize',11)
    ylabel('Length [mm]','fontsize',11)
    if(k==1)
        print([photoname '_LEDStreak.jpg'],'-djpeg')
    end
    %% Stationary LED Figure Printout
case 'StatLED'
    f = figure(1);
    f.Position = [0 0 1920 1080];
    pos1 = [0.23 0.3 0.135 0.3];
    pos2 = [0.1 0.3 0.1 0.3];
    subplot('Position',pos1)
    P = imagesc(rawgreen,[0 30000]);
    daspect([1 1 1]);
    shading interp
    colormap jet
    c = colorbar;
    ylabel(c,['Green Intensity'],'fontsize',11);
    ax1 = gca;
    set(ax1,'YDir','normal');
    ax1.YAxis.Limits = [0 (y2(k)-y1(k))];
    ax1.XAxis.Limits = [0 (x2(k)-x1(k))];
    ax1.YTick = [0 (0.5*(y2(k)-y1(k))) y2(k)-y1(k)];
```

```
        set(ax1, 'YTickLabel', round(mmPC(k)*get(ax1, 'YTick'),1));
        ax1.XTick = [0 0.5*(x2(k)-x1(k)) x2(k)-x1(k)];
        set(ax1, 'XTickLabel', round(mmPC(k)*get(ax1, 'XTick'),1),'fontsize',11);
        xlabel('Length [mm]','fontsize',11);
        subplot('Position',pos2)
        image(L)
        daspect([1 1 1]);
        xlim([x1(k) x2(k)])
        ylim([y1(k) y2(k)])
        ax2 = gca;
        ax2.YTick = [y1(k) (y1(k)+0.5*(y2(k)-y1(k))) y2(k)];
        set(ax2, 'YTickLabel', round(mmPC(k)*(get(ax2, 'YTick') - ...
            y1(k)),1));
        set(ax2,'YDir','normal');
        ax2.XTick = [x1(k) (x1(k)+0.5*(x2(k)-x1(k))) x2(k)];
        set(ax2, 'XTickLabel', round(mmPC(k)*(get(ax2, 'XTick') - ...
            x1(k)),1),'fontsize',11);
        ylabel('Length [mm]','fontsize',11);
        xlabel('Length [mm]','fontsize',11);
        print([photoname '_StatLED' '.jpg'],'-djpeg')
%% Vertical Rotation Figure Printout
    case 'VertStreaks'
        f = figure(1);
        f.Position = [0 0 1920 1080];
        pos1 = [(0.1 + (0.125*(k-1))) 0.3 0.03 0.3];
        if (k==3)
            pos2 = [(0.155 + (0.125*(k-1))) 0.3 0.065 0.3];
```

```
else
    pos2 = [(0.155 + (0.125*(k-1))) 0.3 0.03 0.3];
end
subplot('Position',pos2)
P = imagesc(RT3,[600 1200]);
shading interp
colormap jet
if(k==3)
    c = colorbar('eastoutside');
    title(c,[char(176) 'C'],'fontsize',12);
end
ax1 = gca;
set(ax1,'YDir','normal');
ax1.YAxis.Limits = [0 y2(k)-y1(k)];
ax1.XAxis.Limits = [0 x2(k)-x1(k)];
ax1.XAxis.TickValues = round(mmPC(k)*[0 0.5*(x2(k)-x1(k)) ...
    x2(k)-x1(k)],2);
ax1.YTick = [0 (0.5*(y2(k)-y1(k))) y2(k)-y1(k)];
set(ax1, 'YTickLabel', round(mmPC(k)*get(ax1, 'YTick'),2));
ax1.XTick = [0 (0.5*(x2(k)-x1(k))) x2(k)-x1(k)];
set(ax1, 'XTickLabel', round(mmPC(k)*get(ax1, 'XTick'),2), ...
    'fontsize',11);
xlabel('Length [mm]','fontsize',10)
subplot('Position',pos1)
image(L)
xlim([x1(k) x2(k)])
ylim([y1(k) y2(k)])
```

```
        ax2 = gca;
        ax2.XTick = [x1(k) (x1(k)+0.5*(x2(k)-x1(k))) x2(k)];
        set(ax2, 'XTickLabel', round(mmPC(k)*(get(ax2, 'XTick') - ...
            x1(k)),2));
        set(ax2,'XDir','normal');
        set(ax2,'YDir','normal');
        ax2.YTick = [y1(k) (y1(k)+0.5*(y2(k)-y1(k))) y2(k)];
        set(ax2, 'YTickLabel', round(mmPC(k)*(get(ax2, 'YTick') - ...
            y1(k)),1),'fontsize',11);
        xlabel('Length [mm]','fontsize',10)
        if(k==1)
          ylabel('Length [mm]','fontsize',10)
        end
        if(k==1)
            title('0.375m','fontsize',20,'FontWeight','Normal')
        elseif(k==2)
            title('0.75m','fontsize',20,'FontWeight','Normal')
        elseif(k==3)
            title('1.5m','fontsize',20,'FontWeight','Normal')
        end;
        if(k==3)
            print([photoname '_VertStreaks.jpg'],'-djpeg')
        end


        end
end
    toc; % Ends code timer
```

```
end
```

Appendix G Arduino Camera Trigger Code

```
#include <Adafruit_CharacterOLED.h> // Need to download this library for the
// code to work. At the time of writing (8/10/2021), it can be found at:
// https://learn.sparkfun.com/tutorials/oled-display-hookup-guide/firmware.
// Be sure to unzip the library into your computer's Arduino library
// directory, there's a guide on how to do this on the page.
#include <StopWatch.h> // Stopwatch functionality library. To install just
// search in Arduino's in-built library catalog: "Tools" -> "Manage Libraries..."


const int MagnetReciever = A0, Trans = 2, Shutter = 13, RS = 6, RW = 7, E = 8,
 D4 = 9, D5 = 10, D6 = 11, D7 = 12; // Establishes the pins used. The Magnet
// & Shutter pins are for the camera trigger, the others correspond to the
// pins labeled on the OLED module.
float ShutterTrigger, ShutterThresh = 616, temp, w, rev = 1, convert = 1000000;
 // DefineS all float values. ShutterTrigger could be an int but left a
 // float for code brevity,
 // ShutterThresh accounts for different effects of baud rate at different
 // angular velocities, rest need to be float bc they're used in the angular
 // velocity w calculation. rev refers to the number of revolutions between
 // sensor trigger, convert refers to conversion from ms to s.
StopWatch wTime(StopWatch::MICROS);
Adafruit_CharacterOLED lcd(OLED_V2,RS,RW,E,D4,D5,D6,D7); // Sets up the OLED
// module. The "OLED_V2" initializes the version of the library, the rest
// inputs the digital pins used.


void setup() {
  pinMode(Shutter,OUTPUT);
```

```
  pinMode(Trans,OUTPUT);
  lcd.begin(16,2); // Sets up the OLED module to have 2 rows and 16 columns
  // of output entries.
  Serial.begin(9600); // Begins serial monitor output (useful for diagnostics,
  // to check it go to the ribbon at the top of this window: "Tools" ->
  // "Serial Monitor")
  digitalWrite(Shutter,LOW);
  digitalWrite(Trans,HIGH);
  wTime.start(); // Starts timer
}

void loop() {
  ShutterTrigger = analogRead(MagnetReciever); // Reads to Hall sensor's output
  Serial.println(ShutterTrigger);
  if (ShutterTrigger > ShutterThresh) { // The intention with this conditional
  // is to have the camera shutter line trigger when the sensor reads a value
  // substantially lower than the ambient value, i.e. when it passes by the
  // magnet. The threshold may need to be adjusted based on the realistic
  // reading increase.
      w = (rev/(wTime.elapsed()-temp))*convert*(TWO_PI); // Angular Velocity
      // of the apparatus for that rotation, converted from rev/ms to rad/s.
     // Serial.println(wTime.elapsed()-temp);
     if (50 > w > 5.5) {
      ShutterThresh = 616; // Hall sensor analalog input threshold for
      // higher rotation speeds
     }
     if (w > 50) {
```

```
 ShutterThresh = 645; // Hall sensor analalog input threshold for slower
 // rotation speeds (w=50 rad/s not possible for this apparatus, so it
 // indicates double-triggering
}
 temp = wTime.elapsed();
 //Serial.println(w); // Prints to serial monitor
 lcd.clear(); // Clears OLED screen
 lcd.setCursor(0,0); // Specifies the column/row on the OLED module to
 // begin display
 lcd.print(w); // Prints to OLED module
 lcd.print(" rad/s");
 lcd.setCursor(12,0);
 lcd.print(((2*3.1415)/3)/w); // Gives an estimate of the required
 // shutter speed. Recommended to round up slight at first then
 // trial-and-error until it works optimally.
 lcd.setCursor(0,1);
 //delay(100); // Time delay between when the sensor activates and
 // when the photo is taken. Will need to be determined with the actual
 // experiment setup, and should provide enough delay such that the ember
 // is within the photo frame given the camera's rotation speed.
 // Redundant with command below, pick one.
 delay((3.1415/4)/w); // Sets the delay between detection and the photo
 // as a function of the angular velocity. Designed so that the photo
 // begins right before the ember is in shot, and the shutter speed is
 // time such that it ends right after the ember exits. The denominator
 // of the numerator statement represents the approximate fraction of
 // the arc (i.e. the radians) from detection to start of photo.
```

```
    digitalWrite(Shutter,HIGH); // Triggers the Shutter Line to take a
    // photo. The delay in triggering this line should also be accounted
    // for in the above delay function.
    //Serial.println(Count);
    delay(100); // Needed for code to work, Arduino can't keep up if you
    // go immediately from HIGH to LOW. Also helps prevent double-tapping
    // the shutter.
    digitalWrite(Shutter,LOW);
  }
}
```

Appendix H Idealized Mounting Wire Heat Transfer Considerations

Beyond the situational testing conducted on stationary embers to consider the impact of this mounting wire change, which again proved no appreciable difference in surface temperature readings, a brief heat transfer calculation is considered to theoretically validate the negligible impact of this alteration. For simplicity, it is assumed that the heat transfer will be occurring from a region of approximately the ember's average surface temperature of 930 $°C$ (from references [8] [22]) to an ambient temperature of 20 $°C$ and that the top half of each wire's perimeter is in contact with the ember's inner surface. Both wires are assumed to behave in a "thermally thin" regime with a Biot number of less than 0.1, deemed reasonable due to their relatively minute diameter, and thus are assumed isothermal in the area in contact with the ember [4]. The thermal conductivity of Nichrome 80 at the approximate temperature (slightly lower, due to tabulated value limitations) considered is taken as 21.0 $W/m-K$ and the thermal conductivity of SiC fiber at similar conditions is taken as 87.0 $W/m-K$ as per Tables A.1 and A.2 respectively of reference [4]. The convection heat transfer coefficient along the wire is taken as a conservative 5.0 W/m^2-K. The wires are considered as an extended surface (colloquially referred to as a "fin") with an infinite tip condition, representing that these wires extend to the point where heat transfer is almost certainly no longer occuring. The relevant correlations to this condition are summarized in Table 3.4 of reference [4]. With these assumptions, calculations indicate that the Nichrome wires show an increased conductive heat transfer loss of approximately 65-fold at the ember's inner surface. While significant, these results are approximately as expected from a quotient of the Fourier Law expressions for each wire - the Nichrome has approximate a 16-fold diameter increase and the SiC has an approximately 4-fold higher thermal conductivity, and the conduction heat transfer is expected to scale along $O((D^2)/k)$. The results of this idealized analysis can be seen in H.1. Of further note is that the increased Nichrome 80 wire size will theoretically decrease convective losses in the ember's inner bore, which further supports this wire change.

Table H.1: Idealized Consideration of Ember Mounting Heat Transfer

	Diameter [micron]	**Thermal Conductivity at 1000K** $[W/m-K]$	**Ember Inner Surface Area Contact [%]**	**Four-Sided Conduction Heat Transfer [W]**
Nichrome 80	225	21.0	7.09	0.198
Nicalon ™SiC	14	87.0	0.44	0.00306

Also of note is that the wires have a more closely aligned heat loss per unit area of contact at the ember's inner surface (with the ember's inner surface diameter of 3.175mm), justifying why the contact area percentage is noted, which is the quantity that would be more accurately reflected on the ember's surface.

To contextualize these results, and thereby better justify the use of the Nichrome wire despite its evident conduction heat transfer increase, the approximate heat release rate of the smoldering embers is of interest. Through a cursory analysis of the 6mm diameter, 20cm long, center-bored conditioned Maple embers used here, it was found that approximately 60mg of ember mass remains after the flaming combustion phase. While these embers often fall apart at higher wind speeds as noted in the main body of this work, it is assumed that this higher wind speed increases the rate of reaction and therefore the heat release rate of the ember as per conventional combustion theory. In these trials, it was found that the embers took approximately 75 seconds to burn completely (taken as the point where smoldering ceases and only ash of an approximate mass of 6 mg remains, because this quantity was unable to be measured directly and this 10% ash yield is assumed as a conservative value). As per Table A.32 of reference [18], maple wood has a net heat of combustion of 17.8 kJ/g - while this is a generalization of the material given that its composition will change throughout the flaming stage of combustion as the original maple wood decomposed, it is assumed to be conservative because both carbon and charcoal (similar materials to wood's decomposed composition)

both have significantly higher heats of combustion than this pure maple value. Subsequently, with a burned mass of 54mg and an energy content of 17.8 kJ/g over 75 seconds, an average smoldering HRR of approximately 12.8 W is found. This roughly corresponds with the general findings of Chapter 19 of reference [18]. While the product of several simplifying assumptions, the magnitude of this HRR contextualizes these conductive heat loss results - with the increased Nichrome losses only amounting to approximately 1.55% of the energy generated by the ember under the most restrictive reaction conditions and neglecting the other aforementioned heat transfer effects that would better represent the more complicated transport phenomenon at work in this wire comparison. As indicated by the propagation consideration in Appendix I, although that case considered hotter pixels than the surface average temperature while this one considers cooler, it is still evident that this minute and idealized conductive heat loss increase will have negligible effects on the average surface temperatures considered in this body of work as the experimental comparisons between these wiring mounting methods indicate.

Appendix I Saturated Pixel Error Consideration

- From reference [22], for ratio pyrometry analysis specifically the maximum recorded ember surface temperature is 1136.4 Celsius. As a worst-case approximation, this maximum temperature is assumed to be the temperature of all saturated pixels.
- The average from all of the spinning trials (between wind speeds) is approximately 935 Celsius - because those photos were taken with camera settings adjusted to minimize/remove saturated pixels, take this 935C as the true average. This roughly corresponds with the average temperature findings of references [22] and [8], which is what the two different applied wind speeds considered in this analysis were selected to approximate.
- Consider X as the fraction of allowable error (e.g. 0.05 for 5% error, 0.1 for 10%, etc.)
- Consider Y as the percentage of saturated pixels in the photo
- Accordingly:
  - Expression 1: $Average = (935°C)((1-Y)) + (1136.4°C)(Y)$
    - Simplifying: $Average = 935 - (935(Y)) + (1136.4(Y)) = (201.4(Y)) + 935$
  - Expression 2: $X = \frac{Average}{935} - 1$ (Subtracted because saturation will increase the average under these assumption)
    - Rearranging: $Average = 935(X+1)$
  - Combining Expressions: $935(X+1) = (201.4(Y)) + 935$
    - Simplifying: $X = (0.2154(Y)) + 1 - 1$
    - Rearranging for Y: $Y = \frac{1}{0.2154}(X) = (4.6425(X))$
  - For an error of X = 5% in the temperature average, there can be Y = 23.2% saturated pixels

  - For an error of X = 0.5% in the temperature average, there can be Y = 2.32% saturated pixels
  - For an error X = 0.1% in the temperature average, there can be approximately 0.5% saturated pixels

- Major takeaway 1: Given the specific parameters related to the application of green-red ratio pyrometry on firebrands, pixel saturation produces an error approximately 5 times lower than its own percentage on the ember's average temperature under these assumptions.

- Major takeaway 2: While this brief consideration relies on assumed temperature values and therefore may not reflect a complete quantitatively correct analysis, it still validates that for the general temperatures ranges considered here there can be a small number of saturated pixels in the image while not significantly compromising the fidelity of the average surface temperature results.

Appendix J Vertical Rotation Counterweight Considerations

- To get the vertical apparatus rotating with an approximate constant angular velocity for a set voltage input, needed 5oz of mass on either side of the mounting hole and approximately 30oz of mass (including adhesive and the weights themselves) above the mounting hole at a height of 3.6 inches.

- Assume that the camera's center of mass is somewhere along its lens (i.e. in the opposite direction of the weights with respect to the mounting hole) - due to the complex shape and makeup of the camera, the precise location of the center of mass is difficult to determine exactly.

- Assume that the camera rotates evenly when the mounting hole is its center of mass - this ignores inertial effects as it rotates, so this calculation should be treated as a first-order approximation of the counterweight required.

- Consider that the distance between the camera's center of mass and the mounting hole is X inches. The purpose of this brief analysis is to determine this location X, for future balancing.

  5oz on either side of the mounting hole are just meant to offer stability, and therefore negligibly contribute to this mass balance because their location is approximately at the mounting hole.

- Camera itself weighs approximately 1.1 kg = 38.8 oz. Therefore:

  - $(X inches)(38.8 oz) = (1.8 inches)(30 oz)$
  - X = 1.39 inches

- This would place the camera's center of mass approximately at the beginning of the lens, which is roughly where it would be expected by visual consideration of the camera.

- To accomplish this with two bars of material, for the purposes of consistency and aesthetics:
  - Assume that aluminum has a density of approximately 2700 kg/m^3 and steel has a density of 7750 kg/m^3 [4].
  - McMaster-Carr [35] sells aluminum bars of varying width, thickness, and lengths - for the sake of accommodating the apparatus' scale, assume that a 6" bar is used.
  - To compensate for the camera's weight:
    - (1.39 inches)(38.8 oz) = 2(3 inches)(Y oz)
    - Y = 9 oz each
  - 9 ounces converted to kilograms is 0.255146 kg. Using the above density of aluminum and the 6" (= 0.1524 m) set length of the bar, the aluminum bars each need to have a cross sectional area of 6.2007e-4 m^2 or 0.961 in^2.
  - Using the above density of steel and the 6" (= 0.1524 m) set length of the bar, the steel bars each need to have a cross sectional area of 2.16e-4 m2 or 0.335 in2.
  - On the back of the camera in its vertical rotation position, there's about 1.5" of free room. Therefore, select a 1" bar thickness for simplicity.
  - Accordingly, the aluminum bars would need a width of approximately 0.961 inches (31/32", or just 1") and the steel bars will need a width of 0.335 inches (1/3", but 3/8" is closest on McMaster)
    - Aluminum: https://www.mcmaster.com/9008K14-9008K142/
    - Steel (3/8" Thick): https://www.mcmaster.com/8910K645-9143K402/
    - Steel (5/16" Thick): https://www.mcmaster.com/8910K611-9143K366/

References

[1] U.S. Fire Administration. *What is the WUI?* URL: https://www.usfa.fema.gov/wui/what-is-the-wui.html.

[2] Ralph A. Anthenien, Stephen D. Tse, and A. Carlos Fernandez-Pello. "On the Trajectories of Embers Initially Elevated or Lofted by Small Scale Ground Fire Plumes in High Winds". In: *Fire Safety Journal* 41.5 (2006), pp. 349–363. DOI: https://doi.org/10.1016/j.firesaf.2006.01.005.

[3] Siddhant S. Aphale and Paul E. DesJardin. "Development of a non-intrusive radiative heat flux measurement for upward flame spread using DSLR camera based two-color pyrometry". In: *Combustion and Flame* 210 (2019), pp. 262–278. DOI: https://doi.org/10.1016/j.combustflame.2019.08.042.

[4] Theodore L. Bergman and Adrienne S. Lavine. *Fundamentals of Heat and Mass Transfer*. 8th. John Wiley & Sons, 2017.

[5] David M.J.S. Bowman et al. "The human dimension of fire regimes on Earth". In: *Journal of Biogeography* 38.12 (2011), pp. 2223–2236. DOI: https://doi.org/10.1111/j.1365-2699.2011.02595.x.

[6] Sara E. Caton et al. "Review of Pathways for Building Fire Spread in the Wildland Urban Interface Part I: Exposure Conditions". In: *Fire Technology* 53 (2017), pp. 429–473. DOI: https://doi.org/10.1007/s10694-016-0589-z.

[7] Dave Coffin. *Decoding raw digital photos in Linux*. URL: https://www.dechifro.org/dcraw/.

[8] Kyle Decker. "Imaging Pyrometry of Smoldering Wood Embers at various Distances and Illuminations". MA thesis. College Park, MD: University of Maryland, College Park, Dec. 2020.

[9] Sneh Deep and Gopalan Jagadeesh. "Spatially resolved solid-phase temperature characterization in a sillimanite tube furnace using a broadband two-color ratio pyrometry". In: *Review of Scientific Instruments* 90 (2019). DOI: https://doi.org/10.1063/1.5088149.

[10] Jay L. Devore. *Probability and Statistics for Engineering and the Sciences*. 9th. Cengage Learning, 2016.

[11] Vladimir Fateev et al. "Determination of smoldering time and thermal characteristics of firebrands under laboratory conditions". In: *Fire Safety Journal* 91 (2017), pp. 791–799. DOI: http://dx.doi.org/10.1016/j.firesaf.2017.03.080.

[12] J. Gabitto and C. Tsouris. "Drag coefficient and settling velocity for particles of cylindrical shape". In: *Powder Technol* 183 (2018), pp. 314–322.

[13] Stephanie Glen. *ANOVA Test: Definition, Types, Examples, SPSS*. URL: https://www.statisticshowto.com/probability-and-statistics/hypothesis-testing/anova/.

[14] Michael Grogan. *ANOVA and the Bonferroni Correction*. URL: https://towardsdatascience.com/anova-vs-bonferroni-correction-c8573936a64e.

[15] Haiqing Guo, Jose A. Castillo, and Peter B. Sunderland. "Digital camera measurements of soot temperature and soot volume fraction in axisymmetric flames". In: *Applied Optics* 52.33 (2013), pp. 8040–8047. DOI: http://dx.doi.org/10.1364/AO.52.008040.

[16] Raquel S.P. Hakes et al. "Thermal characterization of firebrand piles". In: *Fire Safety Journal* 104 (2019), pp. 34–42. DOI: https://doi.org/10.1016/j.firesaf.2018.10.002.

[17] Yunwei Huang et al. "Quantifying the Effects of Combustion Gases' Radiation on Surface Temperature Measurements Using Two-Color Pyrometry". In: *Energy & Fuels* 33 (2019), pp. 3610–3619. DOI: https://doi.org/10.1021/acs.energyfuels.9b00257.

[18] Morgan J. Hurley. *SFPE Handbook of Fire Protection Engineering*. 5th. Springer, 2016.

[19] George Morris III and Cal Fire. *2020 Fire Siege*. 2020. URL: https://www.fire.ca.gov/media/hsviuuv3/cal-fire-2020-fire-siege.pdf.

[20] Nadim Kawwa. *When to Use the Kolmogorov-Smirnov Test: Theory, Application, and Interpretation*. URL: https://towardsdatascience.com/when-to-use-the-kolmogorov-smirnov-test-dd0b2c8a8f61.

[21] Mahdiar Khosravi and Patrick Kirchen. "Refinement of the two-color pyrometry method for application in a direct injection diesel and natural gas compression-ignition engine". In: *Journal of Automobile Engineering* 233.14 (2019), pp. 3787–3800. DOI: https://doi.org/10.1177/0954407019832774.

[22] Dennis Kim. "Imaging Pyrometry of Smoldering Wood Embers". PhD thesis. College Park, MD: University of Maryland, College Park, Apr. 2019.

[23] Meg A. Krawchuk et al. "Global Pyrogeography: the Current and Future Distribution of Wildfire". In: *Plos One* 4.4 (2009), e5102. DOI: https://doi.org/10.1371/journal.pone.0005102.

[24] Wayne W. LaMorte. *Nonparametric Tests: Mann Whitney U Test (Wilcoxon Rank Sum Test)*. URL: https://sphweb.bumc.bu.edu/otlt/mph-modules/bs/bs704_nonparametric/bs704_nonparametric4.html.

[25] Oriel Product Line. *Oriel Blackbody Reference Source, Models 67032 and 67033*. Newport. 150 Long Beach Blvd, Stratford, CT 06615, 2017.

[26] Yudong Liu et al. "Temperature and Motion Tracking of Metal Spark Sprays". In: *Fire Technology* 55 (2019), pp. 2143–2169. DOI: https://doi.org/10.1007/s10694-019-00847-3.

[27] Hong Lu et al. "Particle Surface Temperature Measurements with Multicolor Band Pyrometry". In: *American Institute of Chemical Engineers Journal* 55.1 (2008), pp. 243–255. DOI: https://doi.org/10.1002/aic.11677.

[28] Samuel L. Manzello, Seul-Hyun Park, and Thomas G. Cleary. "Investigation on the Ability of Glowing Firebrands Deposited within Crevices to Ignite Common Building Materials". In: *Fire Safety Journal* 44.6 (2009), pp. 894–900. DOI: https://doi.org/10.1016/j.firesaf.2009.05.001.

[29] Samuel L. Manzello and Sayaka Suzuki. "Experimental investigation of wood decking assemblies exposed to firebrand showers". In: *Fire Safety Journal* 92 (2017), pp. 122–131. DOI: http://dx.doi.org/10.1016/j.firesaf.2017.05.019.

[30] Samuel L. Manzello and Sayaka Suzuki. "Influence of board spacing on mitigating wood decking assembly ignition". In: *Fire Safety Journal* 110 (2019). DOI: https://doi.org/10.1016/j.firesaf.2019.102913.

[31] Samuel L. Manzello and Sayaka Suzuki. "The new and improved NIST Dragon's LAIR (Lofting and Ignition Research) facility". In: *Fire and Materials* 36 (2012), pp. 623–635. DOI: https://doi.org/10.1002/fam.1123.

[32] Samuel L. Manzello, Sayaka Suzuki, and Yoshihiko Hayashi. *Summary of Full-scale Experiments to Determine Vulnerabilities of Building Components to Ignition by Firebrand Showers: NIST Special Publication 1126*. National Institute of Standards and Technology, 2011.

[33] Samuel L. Manzello et al. "On the ignition of fuel beds by firebrands". In: *Fire and Materials* 30 (2005), pp. 77–87. DOI: https://doi.org/10.1002/fam.901.

[34] Samuel L. Manzello et al. "Role of Firebrand Combustion in Large Outdoor Fire Spread". In: *Progress in Energy and Combustion Science* 76 (2020). DOI: https://doi.org/10.1016/j.pecs.2019.100801.

[35] McMaster-Carr. *McMaster-Carr Online Marketplace*. URL: https://www.mcmaster.com/.

[36] NWCG. *Spotting Fire Behavior*. 2019. URL: www.nwcg.gov/publications/pms437/crown-fire/spotting-fire-behavior.

[37] Thomas A. Ota et al. "Comparison of Simultaneous Shock Temperature Measurements from Three Different Pyrometry Systems". In: *Journal of Dynamic Behavior of Materials* 5 (2019), pp. 396–408. DOI: https://doi.org/10.1007/s40870-019-00201-2.

[38] Kuhn PB, Ma B, and Connelly BC. "Soot and thin-filament pyrometry using a color digital camera". In: *Proc Combust Inst* 33 (2011), pp. 743–750. DOI: https://doi.org/10.1016/j.proci.2010.05.006.

[39] Karl Soderby. *Liquid Crystal Displays (LCD) with Arduino*. URL: https://docs.arduino.cc/learn/electronics/lcd-displays.

[40] Sony. *DSC-RX10M3: Full Specifications and Features*. 2021. URL: https://www.sony.com/electronics/cyber-shot-compact-cameras/dsc-rx10m3/specifications.

[41] Sayaka Suzuki and Samuel L. Manzello. "Experimental Study on Vulnerabilities of Japanese-Style Tile Roof Assemblies to Firebrand Exposure". In: *Fire Technology* 56 (2020), pp. 2315–2330. DOI: https://doi.org/10.1007/s10694-020-00982-2.

[42] Sayaka Suzuki and Samuel L. Manzello. "Investigating Coupled Effect of Radiative Heat Flux and Firebrand Showers on Ignition of Fuel Beds". In: *Fire Technology* 57 (2021), pp. 683–697. DOI: https://doi.org/10.1007/s10694-020-01018-5.

[43] Sayaka Suzuki and Samuel L. Manzello. "Role of accumulation for ignition of fuel beds by firebrands". In: *Applications in Energy and Combustion Science* 1–4 (2020). DOI: https://doi.org/10.1016/j.jaecs.2020.100002.

[44] Sayaka Suzuki et al. "Firebrands Generated from a Full-Scale Structure Burning under Well-Controlled Laboratory Conditions". In: *Fire Safety Journal* 63 (2014), pp. 43–51. DOI: https://doi.org/10.1016/j.firesaf.2013.11.008.

[45] C.S. Tarifa, P.P. Del Notario, and F.G. Moreno. "On the Flight Paths and Lifetimes of Burning Particles of Wood". In: *International Symposium of Combustion* 10.1 (1965), pp. 1021–1037.

[46] Draper Teri S et al. "Two-dimensional flame temperature and emissivity measurements of pulverized oxy-coal flames". In: *Applied Energy* 95 (2012), pp. 38–44. DOI: https://doi.org/10.1016/j.apenergy.2012.01.062.

[47] Pal Toth et al. "Three-dimensional combined pyrometric sizing and velocimetry of combusting coal particles II: Pyrometry". In: *Applied Optics* 54.15 (2015), pp. 4916–4926. DOI: https://doi.org/10.1364/AO.54.004916.

[48] J.L. Urban et al. "Temperature measurement of glowing embers with color pyrometry". In: *Fire Technology* 55 (2019), pp. 1013–1026. DOI: https://doi.org/10.1007/s10694-018-0810-3.

[49] Joe Urbas, William J. Parker, and Gerald E. Luebbers. "Surface Temperature Measurements on Burning Materials Using an Infrared Pyrometer: Accounting for Emissivity and Reflection of External Radiation". In: *Fire and Materials* 28 (2004), pp. 33–53. DOI: doi:10.1002/fam.844.

[50] Alok Warey. “Influence of thermal contact on heat transfer from glowing firebrands”. In: *Case Studies in Thermal Engineering* 12 (2018), pp. 301–311. DOI: https://doi.org/10.1016/j.csite.2018.04.018.

[51] Yang Xu et al. “Measurement on the Surface Temperature of Dispersed Char in a Flat-Flame Burner Using Modified RGB Pyrometry”. In: *Energy & Fuels* 31 (2017), pp. 2228–2235. DOI: https://doi.org/10.1021/acs.energyfuels.6b02203.

[52] F. Zander. “Surface Temperature Measurements in Hypersonic Testing Using Digital Single-Lens Reflex Cameras”. In: *Journal of Thermophysics and Heat Transfer* 30.4 (2016), pp. 919–925. DOI: https://doi.org/10.2514/1.T4820.

[53] K. Zhou, S. Suzuki, and S.L. Manzello. “Experimental Study of Firebrand Transport”. In: *Fire Technology* 51 (2015), pp. 785–799. DOI: https://doi.org/10.1007/s10694-014-0411-8.